

Common Envelope Mass Ejection in Evolved Stars: Modeling the Dust Emission from post-RGB stars in the LMC

GEETANJALI SARKAR¹ AND RAGHVENDRA SAHAI²

¹*Department of Physics, Indian Institute of Technology, Kanpur
U.P., India*

²*Jet Propulsion Laboratory
Pasadena, CA, USA*

ABSTRACT

Common Envelope (CE) systems are the result of Roche lobe overflow in interacting binaries. The subsequent evolution of the CE, its ejection and the formation of dust in its ejecta while the primary is on the Red Giant Branch (RGB), gives rise to a recently identified evolutionary class – dusty post-RGB stars. Their spectral energy distributions (SEDs) suggest that their mass-ejecta are similar to dusty post-Asymptotic Giant Branch (post-AGB) stars. We have modeled the SEDs of a select sample of post-RGB and post-AGB stars in the Large Magellanic Cloud (LMC), quantified the total dust mass (and gas mass assuming gas-to-dust ratio) in the disks and shells and set constraints on the dust grain compositions and sizes. We find that the shell masses in the post-RGBs are generally less than those in post-AGBs, with the caveat that substantial amount of mass in both types of objects may lie in cold, extended shells. Our models suggest that circumstellar disks, when present, are geometrically thick structures with a substantial opening angle, consistent with numerical simulations of CE evolution (CEE). Comparison of our model dust masses with the predictions of dust production during CEE on the RGB suggest that CEE occurred near or at the tip of the RGB for our post-RGB sources. A surprising result is that some post-RGB stars harbor carbon-rich dust, believed to form when C/O > 1, e.g. following triple-alpha nucleosynthesis and third dredge-up events in AGB stars. This anomaly strengthens the hypothesis that dusty post-RGBs are born in binary systems.

Keywords: Circumstellar dust(236) — Evolved stars(481) — Post-asymptotic giant branch stars(2121)
— Red giant stars(1372)

1. INTRODUCTION

The demise of most stars in the Universe (i.e., in the 1–8 M_{\odot} range) has traditionally been thought to occur as a result of heavy mass-loss on the Asymptotic Giant Branch (AGB), with rates in the range $10^{-8} - 10^{-4} M_{\odot} \text{ yr}^{-1}$ (Höfner & Olofsson 2018), when the stars are very luminous ($L \sim 5000 - 10,000 L_{\odot}$) and cool ($T_{eff} < 3000 \text{ K}$). This heavy mass-loss is believed to occur via a dusty, spherical, radiatively-driven wind, typically expanding at $\sim 5 - 20 \text{ km s}^{-1}$. After the mass-loss has depleted most of the stellar envelope, the stars evolve to higher temperatures through the post-AGB phase at almost constant luminosity. A major unsolved problem in this evolution is that post-AGB stars are surrounded either by a disk (dpAGB objects¹), and/or an expanding dusty shell (pre-planetary nebulae or PPNe) that is generally highly aspherical – objects with round morphology are absent during this evolutionary phase! HST imaging surveys have clearly revealed the aspherical morphologies of pre-planetary nebulae (PPNs), e.g. (Sahai et al. 2007; Ueta et al. 2000). The current consensus is that these dramatic changes in the geometry and kinematics of mass-loss during the AGB-to-PPN transition are a result of strong interaction with a binary companion, see e.g. Sahai (2018) and references therein.

geetanjali.sarkar@gmail.com

¹ disk-prominent post-AGB objects: Sahai et al. (2011)

Intriguingly, binarity may also be responsible for the rapid and unexpected evolution of Red Giant Branch (RGB) stars to the PPN stage (post-RGB stars). The Boomerang Nebula – the coldest object in the Universe (Sahai & Nyman 1997), is the only known representative of a post-RGB star that has evolved to the PPN phase (Sahai et al. 2017), in our Galaxy. The Boomerang’s luminosity is much lower ($L \sim 300 L_{\odot}$) than possible for a post-AGB object, and Sahai et al. (2017) show that merger with a binary companion most likely triggered extreme mass loss ($\sim 10^{-3} M_{\odot} \text{yr}^{-1}$) at a very high ejection velocity (165 km s^{-1}), over a relatively short period (3500 yr) via common-envelope evolution (CEE).

A class of post-RGB objects similar to the Boomerang (i.e., with $L \lesssim 1000 L_{\odot}$) have recently been identified in the Large and Small Magellanic Clouds (LMC and SMC), using optical spectroscopy and *Spitzer* photometry (Kamath et al. 2014, 2015, 2016). The circumstellar dust in the ejecta heated by the central star results in these objects having large mid-IR excesses. The optical spectroscopy allows a determination of stellar parameters (T_{eff} , $\log g$, $[Fe/H]$ and $E(B - V)$) and integration of the spectral-energy-distribution (SED) constrains the bolometric flux. The known distance to the LMC ($\sim 50 \text{ kpc}$) then allows reliable luminosity estimates for these stars; the low luminosities ($< 2500 L_{\odot}$) indicate that these stars have not yet reached the AGB phase. The post-RGB stars are thus separated from post-AGB ones by their low luminosities. Further, the spectroscopically estimated $\log g$ values are compared with theoretical values that a star with similar luminosity and T_{eff} would have in the post-RGB and pre-Main Sequence phase. Stars in the latter phase would be typically 15-20 times more massive and hence differ in $\log g$ by ~ 1.2 (Kamath et al. 2016). However, for stars with poor quality optical spectra, the estimated $\log g$ and hence subsequent classification may not be accurate; e.g. J051845.47-690321.8, a post-AGB star was wrongly classified as a Young Stellar Object (YSO): Kamath & Van Winckel (2019). In addition, since the post-AGB/RGB stars are an old to intermediate age population, they are expected to be more metal poor than the YSOs which would belong to the young LMC population with a mean metallicity of $[Fe/H] \simeq -0.5$ (Kamath et al. 2015).

In this paper, we investigate a sample of this new class of post-RGB stars in the LMC, believed to be rapidly evolving to the PN stage. We also study a sample of post-AGB LMC stars discovered by Kamath et al. (2015): hereafter KWVW15² for comparison, in order to investigate if the properties of the ejecta (e.g., mass, mass-loss rate, temperature, disk-to-shell mass ratio) are different in these two classes. In order to understand the influence of a binary companion on the mass loss history and rapid evolution of a post-RGB star to the PPN stage, we model the circumstellar dust distribution of these objects, using their near to far-infrared SEDs. We chose objects classified as “shell” or “disk” sources from KWVW15. The presence of a disk and/or shell and the ratio of the shell to disk mass (when both can be identified) should help in understanding the physical processes contributing to the early evolution of these stars to the PN stage.

The plan of this paper is as follows. §2 describes the selection of sources for our modeling study, §3 describes our modeling methodology, and §4 and §5 provide details of the SED modeling for each of our post-RGB and post-AGB objects. In §6, we provide a discussion of our modeling results, and §7 gives our conclusions.

2. TARGET SELECTION

The post-RGB and post-AGB stars in this study are taken from KWVW15 – these are listed in Table 1 together with their photometry. The photometry has been compiled by Kamath et al. (2015) and is available online from the Vizier database (<https://vizier.u-strasbg.fr/viz-bin/VizieR>). The Vizier database was further searched to compile the error bars and upper (lower) limits if any on the photometric magnitudes. KWVW15 use the average of epoch 1 and 2 (Meixner et al. 2006) *Spitzer* MIPS 24 μm photometry. Although these values are close enough and the use of an average is justified, we use the photometric data from both the epochs with their corresponding error bars from the NASA/IPAC Infrared Science Archive (<https://irsa.ipac.caltech.edu>).

A total of eight post-RGB and post-AGB stars have been analysed. These are divided equally between “shell” and “disk” sources. KWVW15 introduced this classification based on a visual inspection of their dust SEDs. The shell sources show far-IR excess and the peak of the SED lies beyond 10 μm . The disk sources show near-IR excess indicative of hot dust and the peak of the SED lies around 10 μm or sometimes shortwards. Further, on a color-color plot, see Fig. 12, Kamath et al. (2015), the shell sources have $[3.6] - [4.5] < 0.5$ and $[8] - [24] > 4.0$. Disk sources, on the other hand, have $[3.6] - [4.5] > 0.5$, or in some cases, $[3.6] - [4.5] < 0.5$ in combination with $[8] - [24] < 3.0$.

² According to KWVW15, “shell” sources are those that show a double-peaked SED in the near-to mid-IR region, whereas the “disk” sources do not show two distinct flux peaks but display a near-IR excess.

In order to ensure that for the post-RGBs in our study, CEE occurred on the RGB, we selected objects with $L < 1000 L_{\odot}$. The post-AGB stars are common between KWVW15 and van Aarle et al. (2011), the only exception being J051906.86-694153.9. This star showed the BaII line at 4554.03Å, (KWVW15). The presence of BaII indicates a s-process enriched post-AGB object.

3. MODELLING THE SPECTRAL ENERGY DISTRIBUTION: METHODOLOGY

We have modeled the SEDs of the selected sources using the one-dimensional radiative transfer code, DUSTY (Ivezić et al. 2012). Optical properties for six different grain types are included in the DUSTY code. These are ‘warm’ and ‘cold’ silicates (Sil-Ow and Sil-Oc) from Ossenkopf et al. (1992), silicate and graphite grains (Sil-DL and grf-DL) from Draine & Lee (1984), amorphous carbon (amC-Hn) from Hanner (1988) and silicon carbide (SiC-Pg) from Pégourié (1988). For stars on the RGB, the circumstellar envelope is expected to be oxygen-rich. The change from oxygen-rich to carbon-rich chemistry may occur as a result of specific binary interactions (see §6.3.1) and/or once the star has undergone thermal pulses on the AGB. Silicates are expected to be the main dust species in oxygen-rich outflows, see e.g. Gail et al. (2009). Further, as the name suggests, ‘warm silicates’ are expected to dominate in regions of high dust temperature and/or in fast moving circumstellar outflows (Ossenkopf et al. 1992). In contrast, ‘cold silicates’ are expected in the cool highly obscured circumstellar environment around OH/IR stars and in the interstellar medium (ISM). Hence, for our models, the dust grain composition was chosen to be ‘warm’ (Sil-Ow) silicates. Only when Sil-Ow grain composition did not provide a satisfactory fit, we tried different grain compositions. We used the Mathis, Rumpl, Nordsieck (MRN), Mathis et al. (1977) grain size (a) distribution function, $n(a) \propto a^{-q}$ for $a_{min} \leq a \leq a_{max}$. DUSTY allows one to use standard MRN parameters ($q = 3.5$, $a_{min} = 0.005 \mu\text{m}$ and $a_{max} = 0.25 \mu\text{m}$) or modified MRN parameters. The MRN grain size distribution, for a mixture of silicate and graphite grains, reproduces the Milky Way extinction curve. The Magellanic Cloud extinction curves also obey the same power law for the grain size distribution albeit for different silicate and graphite abundance ratios (Pei 1992). Whenever required, we used a modified MRN distribution by altering a_{min} and a_{max} . The dust density was assumed to be proportional to r^{-2} , where r is the radial distance from the star.

There are multiple input parameters associated with the dusty circumstellar environment: the dust temperature at the inner shell boundary, $T_d(\text{in})$; the relative shell thickness (ratio of outer, R_{out} to inner radius, R_{in}), $Y = R_{out}/R_{in}$; the optical depth at $0.55 \mu\text{m}$, τ ; choice of grain composition and the grain-size distribution.

Our strategy for exploring the parameter space is as follows. We first attempt to fit the SED using a single shell (one-component) model, varying the above input parameters. These model numbers are given a suffix ‘s’. If systematic discrepancies remain between the fit and the data, we then attempt a two-component fit, in which we add an inner component, representative of a hot, compact disk, and vary its T_d , Y , τ , and dust-grain properties. Specific wavelength ranges of the SED are relatively more sensitive to the shell and disk, and help us to constrain their properties in a non-degenerate manner.

For the two-component fit (inner disk + outer shell), we approximated the inner disk by a spherical shell that intercepts a fraction of the direct starlight e.g., as in (Sahai et al. 2003, 2006). Such a shell is thus roughly equivalent to an axially-symmetric wedge-shaped fraction of a sphere; this fraction is hereafter referred to as the “disk fraction” and is listed in Tables 2 and 3. Thus, a disk with an opening angle of θ_d is approximated by a shell that intercepts a fraction, $\sin(\theta_d/2)$ of the radiation emitted within a 4π solid angle, and the corresponding “disk-fraction” is $\sin(\theta_d/2)$. An illustration of the circumstellar geometry is provided in Fig. 1.

A “correctly illuminated” model of the outer shell is constructed assuming the shell to be divided into two parts. The fraction of the shell that lies in the shadow of the disk (= the disk-fraction) is illuminated by star light attenuated by the disk, together with the sum of the scattered and thermal emission from the disk within that fraction. The remaining fraction of the shell is illuminated by direct starlight plus the remaining fraction of the sum of scattered and thermal emission from the disk. The DUSTY code is run separately for each of the two parts of the outer shell and the outputs are added proportionately to obtain the final SED. These correctly illuminated model numbers are given a suffix ‘c’.

In some post-AGB stars, the SEDs may be a result of an interaction between a slow-moving cold outer shell ejected during the previous AGB phase and a fast-moving warm inner shell ejected during the post-AGB phase similar to the case of IRAS 22036+5306 (Sahai et al. 2006). A fit to the SED is then obtained assuming a pair of ‘nested shells’, i.e., a warm inner shell covering 4π solid angle and a cold outer shell. In the correctly illuminated nested shells model, the cold shell is illuminated by the radiation emerging from the warm inner shell.

3.1. Chi-square statistic

We arrive at the best-fit models based on visual inspection of the observed and modeled data. In doing so, we have given more importance to matching the photometry at longer wavelengths ($\lambda \gtrsim 2 \mu\text{m}$) because these are much less affected by the relatively uncertain intervening interstellar absorption along the line-of-sight to each object, and potential stellar variability in the optical and near-infrared. For the sake of completeness, we also calculated the reduced chi-square statistic for each of the models. The reduced chi-square is given by:

$$\chi^2 = \sum \left(\frac{O_i - M_i}{\sigma_i} \right)^2 / (N - p - 1) \quad (1)$$

where, O_i is the observed flux, M_i is the model flux, σ_i is the error in the observed flux and $N-p-1$ is the number of degrees of freedom, with N equal to the number of observed datapoints and p equal to the number of free parameters ($= 5$ for single shell models and 10 for two-component models).

While estimating χ^2 we omitted the WISE photometric data and used the ALLWISE data due to its improved photometric sensitivity at bands 1 and 2 (§6.3.4). For our dataset then, the maximum number of degrees of freedom is 12 for single shell models and 7 for two-component models. Using Pearson’s chi-square distribution table (<https://www.statology.org/chi-square-distribution-table>), we find that the critical chi-square values for 5% significance level and degrees of freedom 7 and 12 correspond to 14.1 and 21.0 respectively. The critical values decrease with decrease in the degrees of freedom. For the majority of our stars, the calculated chi-square statistic lies well above the critical value for both single shell and two-component models. Whenever possible, the model with the least χ^2 value has been chosen as the best-fit for a particular source. However, the chi-square statistic cannot be unambiguously used to decide between our models. Given the large number of free parameters, p vis-à-vis the number of observed data points, a much larger dataset is required for the use of the reduced chi-square method to unambiguously decide the goodness of fit.

3.2. Photometric magnitudes, extinction and stellar model atmospheres

The photometric magnitudes were corrected for the combined effects of Galactic and LMC reddening using a mean $E(B - V) = 0.08$ (Keller & Wood 2006). From the ultraviolet to the near-infrared, we used the LMC’s average extinction curve and $R_V = 3.41$ as derived by Gordon et al. (2003). In the mid-infrared, we applied the extinction law by Gao et al. (2013). The DUSTY code requires the spectral shape of the source illuminating the dusty shell. Kamath et al. (2015) have derived the effective temperatures (T_{eff}), gravities ($\log g$) and metallicities [Fe/H] of the objects used in the study. Hence, for the purpose of modeling, we used the Kurucz stellar atmosphere models closest to these parameters from <http://kurucz.harvard.edu/grids.html>.

3.3. Estimating the circumstellar mass

The DUSTY code outputs the SED, normalized to the bolometric flux, F_{bol} . We determined F_{bol} by scaling the model SED to match the de-reddened SED of our sources. The luminosity and dust mass (M_d) in the circumstellar component was computed for each model. The distance (d) to the LMC was adopted to be 50 kpc. We estimated the luminosity for each model as:

$$L = 4\pi d^2 F_{bol}. \quad (2)$$

For objects obeying a r^{-2} density distribution, the dust mass in the circumstellar component is given by:

$$M_d = 4\pi R_{in}^2 Y (\tau_{100} / \kappa_{100}). \quad (3)$$

From this, we inferred the total mass (gas+dust), $M_{gd} = M_d \delta$ (Sarkar & Sahai 2006) where, τ_{100} is the shell optical depth at $100 \mu\text{m}$, κ_{100} is the dust mass absorption coefficient, κ , at $100 \mu\text{m}$ and δ is the gas-to-dust ratio. We assume $\kappa_{100} = 34 \text{ cm}^2 \text{ g}^{-1}$, as in Sarkar & Sahai (2006). Although this equation is valid for any wavelength, we selected the latter to lie in the far-infrared range, where the SED is dominated by optically-thin thermal emission and therefore the optical depth is better constrained by the model than that at short wavelengths. We note that κ is poorly constrained in general. It may be different for warm ($\gtrsim 300 \text{ K}$) and cold dust ($\lesssim 300 \text{ K}$), e.g. (Demyk et al. 2018). We have therefore chosen to use the same value of κ_{100} in Eq. 3 for the cool shell and warm disk.

The inner radius of the dust shell, R_{in} scales as $L^{1/2}$ where L is the luminosity (Ivezić et al. 2012). DUSTY computes R_{in} for $10^4 L_{\odot}$; we use our estimated luminosity (Eq. 2) for each source, to infer R_{in} for the dust shell/disk in it. M_d also scales in proportion to Y (discussed below).

3.3.1. Thickness of the circumstellar component

The estimated dust mass scales in proportion to Y (Eq. 3) and may therefore be taken as a lower limit to the actual mass in the shell. To understand this, we look at the post-RGB objects, J051920.18-722522.1 (shell-source) and J045755.05-681649.2 (disk-source). Increasing the thickness, Y of the cold outer shell by a factor of 10 in these objects, increased the total shell mass by the same factor (Table 2) but did not cause any noticeable change in the fit to the observed SEDs (Figs. 4.2 and 7.4). While R_{in} is constrained by T_d which is an input parameter, we cannot constrain R_{out} in our SED modeling. This is because the dust temperature decreases with radius – thus the outer regions of the shell emit dominantly at wavelengths longward of the maximum wavelength for which we have data, $\sim 24 \mu\text{m}$. In this paper, we adopt the minimum Y value needed to fit the $24 \mu\text{m}$ photometry.

3.4. Gas-to-dust ratio

The derived mass-loss rate depends on the assumed gas-to-dust ratio. Considering that RGB stars are much less luminous than their AGB counterparts, the gas-to-dust ratio may deviate from the typical value of 200 for the post-AGBs. The dust composition around the post-RGBs may be different from that around the post-AGBs. The gas-to-dust ratio may also depend on the metallicity of the galaxy, e.g. van Loon et al. (1999), Nanni et al. (2019). van Loon et al. (1999) use a value of 500 for the LMC. Roman-Duval et al. (2014) found gas-to-dust ratios of 380^{+250}_{-130} in the LMC. Determining the gas-to-dust ratio as a function of fundamental stellar parameters (e.g., luminosity and metallicity) and evolutionary phase is still a distant goal (Sahai 2009). In this paper, we adopt $\delta = 200$. A higher value of δ would imply a proportionate increase in the derived masses of the ejecta (gas+dust).

3.5. Expansion velocity and mass loss rate

We have no reliable way of estimating the expansion velocity of the cool shells in post-RGB objects. For (the only example of) a post-RGB object where this information is available – the Boomerang Nebula – the cold outer shell is expanding at 165 km s^{-1} . Typical expansion velocities of the shells around post-AGB and PNe are lower, $\sim 10 - 30 \text{ km s}^{-1}$ (Nyman et al. 1992), although collimated outflows in pre-planetary nebulae can have expansion velocities comparable to that in the Boomerang’s cool shell e.g., (Sánchez Contreras & Sahai 2012; Bujarrabal et al. 2001) We have therefore assumed an expansion velocity of 50 km s^{-1} for the cool shells for the post-RGB sources in order to estimate their ages. The thickness of the model shell provides an ejection time-scale, and together with the model shell mass (M_{gd}), an estimate for the mass loss rate (dM/dt). Our estimate of dM/dt is sensitive to both the extent of the dust shell and the assumed expansion velocity (it is possible that the dust shell is much larger, as in the Boomerang Nebula.)

For the warm inner disk in these objects, the expansion velocity is likely to be much lower. For example, in the Boomerang nebula, the FWHM of the emission from the central waist/disk region is 4.3 km s^{-1} (Sahai et al. 2017), which may suggest an expansion velocity of 2.2 km s^{-1} . Jura & Kahane (1999) suggest FWHM $< 5 \text{ km s}^{-1}$ from molecular gas observations around evolved red giant stars. We have therefore assumed an expansion velocity of 2 km s^{-1} to derive the ages and mass-loss rates for the warm inner disks in post-RGB.

In the post-AGB phase, the cold outer shell is most likely a remnant of the previous AGB phase. Since typical AGB expansion velocity is 15 km s^{-1} (Olofsson 1993), we adopt this value for the cool post-AGB shells. For the inner disk, we use an expansion velocity of 2 km s^{-1} , similar to the post-RGBs. The SED of some post-AGB sources such as J050632.10-714229.8 (§ 5.1) indicate the presence of ‘nested shells’. Following the original AGB phase, a post-AGB wind may develop. Radiation pressure from the hot central post-AGB star on the less dense post-AGB wind may accelerate the dust to velocities of upto 150 km s^{-1} (Szczerba & Marten 1993). Since, our post-AGB sources are relatively cool ($T_{eff} < 10000 \text{ K}$), we assume a smaller value of 50 km s^{-1} for the expansion velocity of the warm inner post-AGB shells.

4. MODELS OF POST-RGB OBJECTS

The detailed modeling of the post-RGBs objects listed in Table 1 is discussed below. Our procedure for determining the best-fit model is explained in detail for J043919.30-685733.4, together with a discussion of additional models demonstrating the effect of varying different input parameters. The physical parameters and derived model parameters corresponding to each of the post-RGB models are given in Table 2. We check for the robustness of the fits by varying the different input model parameters. All model fits are shown in their respective Figure Sets. The adopted best-fit models are flagged with † symbol. Corresponding to each figure set, a sample figure displaying the best-fit model is shown. Important physical parameters of the adopted best-fits are summarized in Table 4.

4.1. *J043919.30-685733.4*

This object is classified as a post-RGB shell source by Kamath et al. (2015), with $T_{eff} = 6313\text{K}$, $\log g = 1.5$ and $[Fe/H] = -2.0$. We used a Kurucz stellar atmosphere model with $T_{eff} = 6250\text{K}$, $\log g = 1.5$ and $[Fe/H] = -2.0$. In Fig. 2.1 we show the observed and model SEDs obtained by varying $Y = 8, 100$ and 500 . We assumed the standard MRN grain size distribution. With $T_d(\text{in}) = 550\text{K}$ and $\tau = 1.5$, we find a reasonable fit to the SED, except in the mid-IR region ($\sim 5 - 12\ \mu\text{m}$). We find a lower limit on $Y \sim 100$, from the MIPS $24\ \mu\text{m}$ flux.

Taking $Y = 100$ as the lower limit to the shell thickness, we investigated whether variation in the value of T_d can improve the fit in the mid-IR region. Models with $T_d(\text{in}) = 145, 175$ and 500K , Fig. 2.2 were computed using a standard MRN grain size distribution, and $\tau = 0.8$. We find that the discrepancy in the near-IR persists, except for the model with $T_d(\text{in}) = 500\text{K}$. However, in this case, the model shows a large silicate feature which is not observed – although using larger size grains in the shell may suppress this emission feature, the far-IR flux too falls much more rapidly than that indicated by the MIPS $24\ \mu\text{m}$ data. Since the shell is optically thin at all wavelengths longward of $\sim 1\ \mu\text{m}$, the model SED is not sensitive to the shell geometry. We conclude that a single-shell cannot fit the SED adequately, and resolving these discrepancies requires a two-component model.

Following the two-component approach outlined in Sec.3, we found that a good fit to the SED could be obtained with a disk fraction ~ 0.35 , together with a cold outer shell that dominates the emission in $\lambda \gtrsim 10\ \mu\text{m}$ region. This cold shell has $T_d(\text{in}) = 130\text{K}$, $Y = 20$, $\tau = 0.95$ and standard MRN grain size distribution (blue curve in Fig. 2.3 and 2.5). $Y = 20$ is a lower limit for the shell thickness. For the warm inner disk with $Y = 1.4$ and an r^{-2} density, alternate model fits were obtained assuming standard MRN grain size distribution, model #1: $T_d(\text{in}) = 1000\text{K}$, yellow curve, Fig. 2.3 and modified MRN grain size distribution: $a_{min} = 1\ \mu\text{m}$ and $a_{max} = 25\ \mu\text{m}$, model #2: $T_d(\text{in}) = 800\text{K}$, yellow curve, Fig. 2.5) in the disk.

The sensitivity of the SED to different a_{min} and a_{max} grain sizes in the inner disk is shown in Fig. 2.7. A smaller a_{min} (by a factor of 10) would cause a deficit in the near-IR range. Similarly, decreasing a_{max} (by a factor of 5) causes a deficit between 5 and $10\ \mu\text{m}$. Increasing a_{max} however, does not appear to effect the SED.

For both models #1 and #2 (Figs. 2.3 and 2.5), there is a mismatch with the IRAC4 ($8\ \mu\text{m}$) flux. We convolved the model flux with the IRAC4 response curve and estimated the magnitude at $8\ \mu\text{m}$ for models #1 (14.96 mag) and #2 (14.76 mag). In comparison, the observed magnitude at $8\ \mu\text{m}$ (corrected for extinction) is significantly lower (13.84). The IRAC4 bandpass covers a strong PAH emission feature which is not included in the DUSTY code. If we were to include the excitation of PAHs, it is possible that a better fit would be obtained in this region.

We show the sensitivity of the SEDs to varying the Y parameter for models #1 and #2 in Figs. 2.4 and 2.6. Increasing the thickness causes a mismatch in the mid-IR and with WISE band 3 (W3/12 μm) flux.

In the two-component models (models #1 and #2), it was assumed that the shell is illuminated by the radiation from the central star and captures ~ 0.65 of the bolometric flux of the star. The disk was treated as a separate entity illuminated by the central star and capturing (~ 0.35) of the bolometric flux from the star. The output was the sum of the modeled fluxes in each instance. Finally, we constructed the correctly illuminated models Table 2, model #1,c & #2,c and Figs. 2.8 & 2.9 following the prescription in Sec. 3.

The fit in the far-IR is identical for the two models; we compared the model and observed SEDs in the near and mid-IR region to choose our best-fit model. The model SED is closer to the observed J,H,K fluxes in the case of model #1,c, and we adopt this as the best-fit for J043919.30-685733.4. This choice is re-affirmed by a comparison of reduced chi-square in the two cases, model #1,c (18.1) and model #2,c (30.4). In the light of the above discussion, we omitted the IRAC4 ($8\ \mu\text{m}$) flux and the W4' flux while calculating the reduced chi-square. The latter is an upper limit. Our estimated luminosity, $L = 116 L_\odot$ from model #1,c is in close agreement with the observed luminosity of the object, $L = 106 L_\odot$ (KWVW15). The total mass accumulated in the shell is $5.2 \times 10^{-3} M_\odot$ over a relatively short period of $\sim 200 - 300$ years at a mass loss rate of $7.1 \times 10^{-6} - 1.1 \times 10^{-5} M_\odot \text{yr}^{-1}$ (Table 2). The inner disk is very young (~ 2 years) with a mass of $\sim 2.19 \times 10^{-8} M_\odot$ and a mass loss rate of $1.18 \times 10^{-8} M_\odot \text{yr}^{-1}$.

4.2. *J051347.57-704450.5*

This object is classified as a post-RGB shell source by KWVW15, with $T_{eff} = 4500\text{K}$, $\log g = 1.0$ and $[Fe/H] = -0.5$. We used a Kurucz stellar atmosphere model with these parameters for modeling the SED of the object. Our adopted best-fit model corresponds to $T_d(\text{in}) = 250\text{K}$, modified MRN grain size distribution: $a_{min} = 0.1\ \mu\text{m}$, $a_{max} = 0.25\ \mu\text{m}$, $\tau = 0.40$ and $Y = 3.0$ (Fig. 3.1; $\chi^2 = 69.2$). In Figs. 3.2 – 3.5, we show the effects of varying $T_d(\text{in})$, τ , grain sizes and Y . We find that the GSC 2.2 R-band flux is much below the modeled SED. Three R-band magnitudes

are available for the object from Vizier, $R = 16.74 \pm 0.44$ (GSC 2.2 Catalogue/STScI 2001), $R1 = 15.76$ and $R2 = 16.29$ (USNO-B 1.0 Catalog); Monet et al. (2003). We plotted the corresponding extinction corrected fluxes in the SED. The USNO-B 1.0 R-band fluxes are closer in agreement with the modeled SED. Mismatch between the modeled SED and the I-band flux is seen in several of our objects and is discussed in § 6.3.3. Since a single shell model provided satisfactory fits to the optical and IR fluxes, we did not try a two-component model for this star.

The luminosity of the object is estimated to be $776 L_{\odot}$. In comparison, KWVW15 estimated a luminosity of $712 L_{\odot}$ by integrating the flux under the observed SED and a photospheric luminosity of $840 L_{\odot}$. From our best-fit model, the total mass accumulated in the shell is $4.66 \times 10^{-5} M_{\odot}$ over a period of 18 years at a mass loss rate of $2.59 \times 10^{-6} M_{\odot} \text{yr}^{-1}$.

4.3. J051920.18-722522.1

This object is classified as a post-RGB shell source by KWVW15, with $T_{eff} = 4500$ K, $\log g = 1.5$ and $[Fe/H] = -1.5$. We used a Kurucz stellar atmosphere model with these parameters. A fit to the U,B,V and far-IR fluxes could be obtained using T_d (in) = 200 K, MRN grain size distribution, $\tau = 0.75$ and $Y = 20$ (model # 1,s; $\chi^2 = 89.1$). Figs. 4.3 – 4.6 show the effects of varying T_d (in), τ , grain sizes and Y in model # 1,s. For all cases, the R and I-band fluxes remain well below the modeled SED (§ 6.3.3). To account for this deficit, we assumed a two-component model (model # 2) with a warm (T_d (in) = 500 K), inner disk, in addition to a cold outer shell at 110 K. This disk was approximated as a wedge-shaped fraction (~ 0.4) of a sphere with $\tau = 0.4$, $Y = 2.0$ and modified MRN grain size distribution: $a_{min} = 0.5 \mu\text{m}$ and $a_{max} = 20 \mu\text{m}$. The cold outer shell is characterised by $\tau = 1 \mu\text{m}$, $Y = 20$ and MRN grain size distribution. We constructed the correctly illuminated spectrum (model # 2,c; $\chi^2 = 17.5$) for the shell in the two solid angles (Fig. 4.1). Increasing the thickness of the cold outer shell by a factor of 10, does not cause any appreciable change in the fit to the SED (Fig. 4.2, § 3.3.1).

Based on visual inspection and a comparison of reduced chi-square values, we adopted model # 2,c as the best-fit. From this, we estimated luminosity, $L = 582 L_{\odot}$. In comparison, KWVW15 estimated a luminosity of $496 L_{\odot}$ by integrating the flux under the observed SED. The total mass in the shell is estimated to be $3.41 \times 10^{-2} M_{\odot}$ accumulated over $\sim 645 - 792$ years at a mass loss rate of $\sim 2.1 \times 10^{-5} - 2.6 \times 10^{-5} M_{\odot} \text{yr}^{-1}$. The inner disk is much younger (15.9 years) with a mass of $3.01 \times 10^{-5} M_{\odot}$ and a mass loss rate of $1.89 \times 10^{-6} M_{\odot} \text{yr}^{-1}$.

4.4. J053930.60-702248.5

This object is classified as a post-RGB shell source by KWVW15, with $T_{eff} = 4315$ K, $\log g = 0.5$ and $[Fe/H] = -0.9$. We used a Kurucz stellar atmosphere model with $T_{eff} = 4250$ K, $\log g = 0.5$, $[Fe/H] = -1.0$ for modeling the SED of this object. A fit to the optical and IR fluxes could be obtained using T_d (in) = 300 K, MRN grain size distribution, $\tau = 0.7$ and $Y = 10$ (Fig. 5.1; $\chi^2 = 30.4$). Figs. 5.2 – 5.5, show the effects of varying T_d (in), τ , grain sizes and Y . We find that the reduced chi-square is least for a modified MRN grain size distribution, $a_{min} = 0.005 \mu\text{m}$ and $a_{max} = 0.50 \mu\text{m}$ (Table 2, Fig. 5.4). Visual inspection of the model plot in this case reveals that this is due to better agreement with ALLWISE W4' data. However, the latter model shows a mismatch with the IRAC4 ($8 \mu\text{m}$) flux. Hence, we adopt the model with standard MRN grain size distribution as the best-fit. For the same reason, we also reject the model with $\tau = 0.8$ (Fig. 5.3) even though the model has a lower chi-square value than our adopted best-fit. Since a single shell model provided satisfactory fits to the optical and IR fluxes, we did not try a two-component model for this star.

Our estimated luminosity ($295 L_{\odot}$) is in good agreement with the observed ($248 L_{\odot}$) and photospheric luminosity ($294 L_{\odot}$) values of KWVW15. From our best fit model, the total mass accumulated in the shell is $5.8 \times 10^{-5} M_{\odot}$ over a period of 27.2 years at a mass loss rate of $2.13 \times 10^{-6} M_{\odot} \text{yr}^{-1}$.

4.5. J045555.15-712112.3

This object is classified as a post-RGB disk source by Kamath et al. (2015), with $T_{eff} = 10000$ K, $\log g = 2.0$ and $[Fe/H] = -0.5$. We used a Kurucz stellar atmosphere model with these parameters. Fig. 6.1 shows a one-component model fit to the observed SED (model # 1,s) using Sil-Ow grains, T_d (in) = 550 K, $a_{min} = 0.005 \mu\text{m}$, $a_{max} = 1.0 \mu\text{m}$, $\tau = 2.3$ and $Y = 20$. The effects of varying T_d (in), τ , grain sizes and Y are shown in Figs. 6.5 – 6.8. Our model fit (# 1,s) is deficit in the near-IR region and additionally, there is a mismatch with the IRAC2 ($4.5 \mu\text{m}$), W2 ($4.6 \mu\text{m}$) and IRAC3 ($5.8 \mu\text{m}$) fluxes.

For a better fit in the near-IR region, we assumed a two-component model (model # 2) with a warm, T_d (in) = 1200 K, thin inner disk, in addition to the cold outer shell at 550 K. The disk composed of Sil-Ow grains was approximated

as a wedge-shaped fraction (~ 0.1) of a sphere with $\tau = 0.5$, $Y = 10$ and grain size distribution: $a_{min} = 0.005 \mu\text{m}$ and $a_{max} = 0.1 \mu\text{m}$. We constructed the correctly illuminated spectrum for the shell in the two solid angles (#2,c, Fig. 6.2). We tried an alternate two-component model (model #3) using graphite grains (grf-DL) for the warm inner disk ($T_{eff} = 800 \text{ K}$) and a combination of Sil-Ow (0.8) and grf-DL (0.2) for the cold outer shell ($T_{eff} = 500 \text{ K}$). The inner disk was approximated to be a wedge-shaped fraction (0.1) of a sphere with $\tau = 0.7$, $Y = 5$ and MRN grain size distribution: $a_{min} = 0.005 \mu\text{m}$ and $a_{max} = 0.25 \mu\text{m}$. The cold shell is modeled using $\tau = 1.8$, $Y = 2$ and MRN grain size distribution. Fig. 6.3 shows the correctly illuminated two-component model (#3,c). Besides the continuing mismatch at IRAC2 ($4.5 \mu\text{m}$), W2 ($4.6 \mu\text{m}$) and IRAC3 ($5.8 \mu\text{m}$), the fit remained unsatisfactory in the near-IR.

Further, we investigated the possibility that a stellar companion dominates the emission at and around $4.6 \mu\text{m}$ in models #2 and #3, with suitable adjustments in the disk and the shell parameters, by fitting a blackbody curve to the flux at $4.6 \mu\text{m}$. We find that a blackbody with $T_{eff} = 800 \text{ K}$, and $L = 39 L_{\odot}$ would account for the flux at $4.6 \mu\text{m}$. Since a main-sequence companion star with such a low T_{eff} would have a very low luminosity (i.e., much lower than $39 L_{\odot}$), we conclude models including a stellar companion cannot explain the discrepancy at $4.6 \mu\text{m}$.

The relatively low flux at $4.6 \mu\text{m}$ may result from the presence of a deep absorption feature at $4.6 \mu\text{m}$. Such a feature has been observed in YSOs (Lacy et al. 1984), and is believed to be due to solid phase CO and cyano group molecules. J045555.15-712112.3 was classified originally as a possible YSO by Gruendl & Chu (2009). KWVW15 re-classified it (and many other objects also originally classified as YSOs), using an automated spectral typing pipeline (STP) that focusses on the Balmer-line region for the determination of T_{eff} , for objects with $T_{eff} > 8000 \text{ K}$ (Kamath et al. 2014). However, an examination of the optical spectrum (downloaded from VizieR) reveals a lack of reliable discernible spectral features in this region. It is therefore plausible that for this case, the STP fit did not provide a good estimate of T_{eff} and hence $\log g$. A higher $\log g$ value would support the classification of J045555.15-712112.3 as a possible YSO.

In the scenario that the object is indeed a post-RGB source as classified by KWVW15 and not a YSO, we explored models which may give a better fit at $4.6 \mu\text{m}$. The two-component model #4 is shown in Fig. 6.4. The warm inner disk, T_d (in) = 1000 K, composed of Sil-Ow grains was approximated to be a wedge-shaped fraction (0.4) of a sphere with $\tau = 1.0$, $Y = 10$ and MRN grain size distribution. The cold outer shell, T_d (in) = 300 K has Sil-Ow grains, $\tau = 2.5$ and $Y = 2$ and MRN grain size distribution. The model provides a good fit at $4.6 \mu\text{m}$ but is discrepant with the observed values in the near-IR and at IRAC3 ($5.8 \mu\text{m}$) and IRAC4 ($8 \mu\text{m}$). The discrepancy at IRAC bands 3 and 4 may be due to PAH emissions and has been discussed further in Sec. 6.3.1. Since the inner disk is optically thick, we cannot apply the ‘‘correctly illuminated model’’ formalism to this object.

We calculated the reduced chi-square for each of the models, model #1,s/ $\chi^2 = 619.8$, model #2,c/ $\chi^2 = 1125.5$ and model #3,c/ $\chi^2 = 1318.3$, model #4/ $\chi^2 = 116.6$. Based on the above discussion, if the object is indeed a post-RGB source, we adopt model #4 as the best-fit to the observed SED.

From this model, we estimated a luminosity of $465 L_{\odot}$ for J045555.15-712112.3. KWVW15 estimated a luminosity of $454 L_{\odot}$ by integrating the flux under the observed SED and a photospheric luminosity of $191 L_{\odot}$. They attributed this difference in luminosity estimates to either a non-spherically symmetric dust envelope or substantial flux contribution from another object coincident with J045555.15-712112.3 in the sky. The total mass accumulated in the shell is $2.84 \times 10^{-4} M_{\odot}$ over ~ 7.9 years at a mass loss rate of $3.59 \times 10^{-5} M_{\odot} \text{ yr}^{-1}$. The mass accumulated in the disk is $3.08 \times 10^{-6} M_{\odot}$ over 131 years at a mass loss rate of $2.35 \times 10^{-8} M_{\odot} \text{ yr}^{-1}$.

4.6. J045755.05-681649.2

This object is classified as a post-RGB disk source by KWVW15, with $T_{eff} = 4927 \text{ K}$, $\log g = 1.5$ and $[Fe/H] = -0.3$. We used a Kurucz stellar atmosphere model with $T_{eff} = 5000 \text{ K}$, $\log g = 1.5$ and $[Fe/H] = -0.3$. We first modeled the SED of the object, assuming a single dust shell surrounding the central star (model #1,s, Fig. 7.1). A fit to the optical and far-IR fluxes could be obtained using T_d (in) = 500 K, MRN grain size distribution ($a_{min} = 0.005 \mu\text{m}$, $a_{max} = 0.25 \mu\text{m}$), $\tau = 1.0$ and $Y = 20$ (model #1,s). The I-band flux is well below the modeled SED. Additionally, there is a mismatch at W2 ($4.6 \mu\text{m}$) and IRAC4 ($8 \mu\text{m}$). These discrepancies have been discussed further in (§6). The mismatch at IRAC4 may be attributed to PAH emission, similar to J043919.30-685733.4. Figs. 7.5 – 7.7 show the observed and modeled SED of the object along with effects of varying T_d (in), τ , and Y .

To obtain a better fit in the mid-IR region, we tried a two-component model (model #2), i.e. a warm inner disk, approximated as an axially symmetric wedge-shaped fraction (0.4) of a sphere and a cold outer shell. Assuming the fraction that is not covered by the disk, reasonable fit to the far-IR flux distribution ($\lambda \gtrsim 10 \mu\text{m}$) could be obtained

for for T_d (in) = 400 K, $Y = 30$, $\tau = 0.9$ and modified MRN grain size distribution: $a_{min} = 0.1 \mu\text{m}$, $a_{max} = 1.0 \mu\text{m}$. For the warm inner disk, T_d (in) = 1300 K, $Y = 2$, $\tau = 0.5$ and modified MRN grain size distribution: $a_{min} = 0.005 \mu\text{m}$, $a_{max} = 2.0 \mu\text{m}$ was used. We constructed the correctly illuminated model for the shell in the two solid angles (#2,c). The output modeled flux distribution is shown in Fig. 7.2.

Since, both the one and two-component models could not provide a fit at IRAC4 ($8 \mu\text{m}$), we omitted the flux at this point for the reduced chi-square calculation. Further, the ALLWISE W4' flux is an upper limit and is also omitted from the chi-square calculation. The reduced chi-square is least for the single shell model with T_d (in) = 550K, $\chi^2 = 20.7$ (Table 2). This value is comparable with $\chi^2 = 24.7$ for the two-component model #2,c. Since the two fits appear similar, we overplotted the two models (Fig. 7.3). On visual inspection, we find that the latter provides a better fit in the region of the mid-IR IRAC bands, $3\mu\text{m} - 6\mu\text{m}$ with a lower value for the residual sum (98.8) than in the former case (186.4). Hence, we adopt the two-component model #2,c as the best-fit for J045755.05-681649.2. Increasing the thickness of the outer shell by a factor of 10 in model #2,c does not cause any appreciable change in the fit to the SED (Fig. 7.4, §3.3.1).

From our best-fit model, the luminosity is estimated to be $L = 217 L_\odot$. In comparison, KWVW15 estimated a luminosity of $190 L_\odot$ by integrating the flux under the observed SED and a photospheric luminosity of $215 L_\odot$. The total mass accumulated in the shell is $\sim 5.73 \times 10^{-5} M_\odot$ over a short period of $\sim 30 - 40$ years at a mass loss rate of $\sim 7 \times 10^{-7} - 9 \times 10^{-7} M_\odot \text{yr}^{-1}$. The inner disk is much younger, ~ 1.9 yr. with a mass of $\sim 9.64 \times 10^{-9} M_\odot$. and a mass loss rate of $\sim 5 \times 10^{-9} M_\odot \text{yr}^{-1}$.

4.7. J050257.89-665306.3

This object is classified as a post-RGB disk source by KWVW15, with $T_{eff} = 4586\text{K}$, $\log g = 0.5$ and $[Fe/H] = -0.5$. We used a Kurucz stellar atmosphere model with $T_{eff} = 4500$ K, $\log g = 0.5$ and $[Fe/H] = -0.5$. A single shell model could not provide a fit to the near and mid-IR fluxes (model #1,s; Fig. 8.1, $\chi^2 = 141.77$). Hence, we tried two-component models with a warm inner disk and a cold outer shell. A fit to the optical and IR flux could be obtained under two scenarios: a two-component model in which the disk and shell are composed of Sil-Ow grains (model #2) and another two-component model in which the disk is composed of amC-Hn grains and shell is composed of Sil-Ow grains (model #3). The discrepancies at I-band and IRAC4 ($8 \mu\text{m}$) have been discussed in §6. In calculating the reduced chi-square, we have omitted the flux at $8\mu\text{m}$.

In model #2, the inner disk (T_d (in) = 1200 K) is composed of Sil-Ow grains with modified MRN grain size distribution: $a_{min} = 0.3 \mu\text{m}$ and $a_{max} = 5.0 \mu\text{m}$, $\tau = 0.5$ and $Y = 3.0$. The outer shell (T_d (in) = 240 K) is composed of Sil-Ow grains with modified MRN grain size distribution: $a_{min} = 0.005 \mu\text{m}$ and $a_{max} = 1.0 \mu\text{m}$, $\tau = 1.2$ and $Y = 10.0$. The disk was approximated as an axially symmetric wedge-shaped fraction (0.4) of a sphere. The correctly illuminated model (#2,c, $\chi^2 = 48.4$) is presented in Fig. 8.2.

In model #3, the inner disk (T_d (in) = 1000 K) is composed of amC-Hn grains with modified MRN grain size distribution: $a_{min} = 0.005 \mu\text{m}$ and $a_{max} = 0.5 \mu\text{m}$. $\tau = 0.6$ and $Y = 2.0$. The outer shell (T_d (in) = 250 K) is composed of Sil-Ow grains with MRN grain size distribution: $a_{min} = 0.005 \mu\text{m}$ and $a_{max} = 0.25 \mu\text{m}$, $\tau = 1.7$ and $Y = 10.0$. The disk was approximated as an axially symmetric wedge-shaped fraction (0.3) of a sphere. The correctly illuminated model (#3,c, $\chi^2 = 43.9$) is presented in Fig. 8.3.

The reduced chi-square is comparable for models #2,c and #3,c. On visual inspection we find that model #2,c shows better agreement with the optical (U,B) fluxes (Fig. 8.4). Hence we adopt the two-component model #2,c as the best fit for J050257.89-665306.3.

From our correctly illuminated model #2,c (Table 2), the luminosity is estimated to be $L = 303 L_\odot$. In comparison, KWVW15 estimated a luminosity of $267 L_\odot$ by integrating the flux under the observed SED and a photospheric luminosity of $177 L_\odot$. The total mass accumulated in the shell is $2.24 \times 10^{-4} M_\odot$ over a period of $\sim 30 - 38$ years at a mass loss rate of $\sim 3 \times 10^{-6} M_\odot \text{yr}^{-1}$. The inner disk is much younger ($\sim 4.3\text{yr}$) with a mass of $\sim 5.77 \times 10^{-8} M_\odot$ and a mass loss rate of $\sim 1.3 \times 10^{-8} M_\odot \text{yr}^{-1}$.

4.8. J055102.44-685639.1

This object is classified as a post-RGB disk source by KWVW15, with $T_{eff} = 7625$ K, $\log g = 1.0$ and $[Fe/H] = -0.5$. We used a Kurucz stellar atmosphere model with $T_{eff} = 7500$ K, $\log g = 1.0$ and $[Fe/H] = -0.5$. The near-IR flux distribution of this object suggests the presence of a warm inner disk. A single shell model (model #1,s, $\chi^2 = 600.2$) could not provide a fit to the optical and near-IR fluxes. We therefore tried two component models with a

warm inner disk and cold outer shell made up of Sil-Ow grains. In these models, # 2a and # 2b, the inner disk was approximated as a fraction (0.4 and 0.3 respectively) of a sphere. However, we could not obtain a simultaneous fit to the optical and near-IR fluxes. The model fits # 1,s, # 2a and # 2b are shown in Fig. 9.1.

The near-IR flux of the object indicates a dust temperature in excess of 1500 K. This would exceed the sublimation temperature of silicate grains. We therefore tried amorphous carbon grains (amC-Hn) for the inner disk (model # 3, $\chi^2 = 220.0$). In the DUSTY input, the dust sublimation temperature was changed to 2500 K. Amorphous carbon has a higher sublimation temperature than silicate grains. While amorphous carbon has been observed in the dusty disk around C-rich post-AGB stars, e.g. HR4049 (Acke et al. 2013), we do not expect to see it in the circumstellar environment of a post-RGB star because such dust is believed to form when the C/O ratio is >1 in the star’s atmosphere, following formation of C via $3-\alpha$ nucleosynthesis and (the third) dredge-up – events that occur at the centers of AGB stars. In the case of J055102.44-685639.1, we find that the disk is optically thick ($\tau = 1.0$) and amC-Hn grains provide a reasonable fit to the SED in the near and mid-infrared (Fig. 9.2). The cold outer shell has a combination of warm silicates and silicon carbide. The carbon-rich circumstellar chemistry may be explained if the post-RGB star is a CH giant in a binary system that formed when the post-RGB progenitor accreted carbon-rich matter from a more massive AGB companion (now a WD) before undergoing Common Envelope (CE) ejection. Such a scenario may also account for the presence of PAH molecules in the circumstellar environment of some post-RGB stars (see § 6.3.1).

Our choice of a two-component model (# 3) as the best fit is re-affirmed by a lower value of the reduced chi-square in this case, $\chi^2 = 147.3$. The disk was approximated as an axially symmetric wedge-shaped fraction (0.3) of a sphere with amC-Hn grains, $T_d = 2000$ K, $Y = 7.0$, $\tau = 1.0$ and modified MRN grain size distribution: $a_{min} = 0.005 \mu\text{m}$, $a_{max} = 0.05 \mu\text{m}$. The outer shell (Sil-Ow/0.4 and SiC-Pg/0.6) has $T_d = 350$ K, $Y = 3.0$, $\tau = 12.0$ and modified MRN grain size distribution: $a_{min} = 0.005 \mu\text{m}$, $a_{max} = 0.07 \mu\text{m}$. At the large optical depth of the outer shell, the SiC feature goes into absorption (Fig. 9.2). Further, since the inner disk is optically thick, we cannot apply the “correctly illuminated model” formalism to this object.

From the best-fit model # 3 (Table 2), we estimated a luminosity of $621L_\odot$. In comparison, KWVW15 estimated $452L_\odot$ and $815L_\odot$ respectively for the observed and photospheric luminosity of the object. The total mass accumulated in the shell is $3.05 \times 10^{-3} M_\odot$ over a period of ~ 12.5 years at a mass loss rate of $\sim 2.43 \times 10^{-4} M_\odot \text{yr}^{-1}$. The inner disk is younger, ~ 8.8 yr. with a mass of $\sim 1.99 \times 10^{-8} M_\odot$ and a mass loss rate of $\sim 2.27 \times 10^{-9} M_\odot \text{yr}^{-1}$.

5. MODELS OF POST-AGB OBJECTS

The detailed modeling of the post-AGB objects listed in Table 1 is discussed below. The physical parameters and derived model parameters corresponding to the post-AGB models are given in Table 3. We check for the robustness of the fits by varying the different input model parameters. All model fits are shown in their respective Figure Sets. The adopted best-fit models are flagged with † symbol. Corresponding to each figure set, a sample figure displaying the best-fit model is shown. Important physical parameters of the adopted best-fits are summarized in Table 4.

5.1. J050632.10-714229.8

This object is classified as a post-AGB shell source by KWVW15, with $T_{eff} = 7614$ K, $\log g = 0.5$ and $[Fe/H] = -0.4$. However, based on high resolution spectra, van Aarle et al. (2013) obtained a much lower T_{eff} ($= 6750$ K), $\log g = 0.5$ and a lower $[Fe/H]$ ($= -1.0$). We prefer the van Aarle et al. (2013) values based on their high resolution data. Hence, we used a Kurucz stellar atmosphere model with $T_{eff} = 7000$ K, $\log g = 0.5$ and $[Fe/H] = -1.0$. Fig. 10.1 shows a one-component model fit to observed SED using Sil-Ow grains, standard MRN grain size distribution, T_d (in) $= 200$ K, $\tau = 0.6$ and $Y = 20$ (model # 1,s). This model is deficient in the mid-IR region, particularly at IRAC3 ($5.8 \mu\text{m}$) and IRAC4 ($8 \mu\text{m}$).

Since J050632.10-714229.8 is a post-AGB star, we modeled the SED using the ‘nested shells’ approach outlined in Sec. 3. Fig. 10.2 shows the fit obtained in the mid-IR using Sil-Ow (grain type # 1) in the inner shell, T_d (in) $= 400$ K, standard MRN grain size distribution, $\tau = 0.4$ and $Y = 2$. It also shows that changing the grains from warm (Sil-Ow) to cold silicates (Sil-Oc) doesn’t alter the fit significantly in the mid-IR, so we use Sil-Ow grains for the inner shell. The circumstellar environment of a post-AGB star may have a mix of carbon and silicate dust grains. Fig. 10.3 shows the fits obtained using different grain combinations. We find that Sil-Ow (# 1) at 400 K, a combination of amC-Hn/0.1 and Sil-Ow/0.9 (# 2) at 350 K and a combination of grf-DL/0.3 and Sil-Ow/0.7 (# 3) at 350 K (Fig. 10.4) all provide good fits to the observed SED in the mid-IR. However, neither combination of grains could provide

a satisfactory fit to the flux from $4.6 \mu\text{m} - 8 \mu\text{m}$. These discrepancies are further discussed in §6. Using each of the above best-fit warm inner-shell models, we obtained best-fit models for the cold outer shell (nested models #1; $\chi^2 = 181.6$; #2; $\chi^2 = 164.2$ and #3; $\chi^2 = 154.7$; Table 3). Fig. 10.5 shows the complete correctly illuminated model SED of J050632.10-714229.8 for each grain combination.

The reduced chi-square is least for model #3. Hence, we adopt this as the best-fit model. Our estimated luminosity ($5434L_{\odot}$) is in good agreement with KWVW15's observed luminosity for the object ($4910L_{\odot}$). They estimated a much higher photospheric luminosity of $7606L_{\odot}$. The latter may be in error since it is based on their estimate of T_{eff} and metallicity from low resolution spectra which is significantly different from that based on high resolution spectra of van Aarle et al. (2013). From model #3, the total mass accumulated in the outer shell, the shell age and mass loss rate respectively are $5.91 \times 10^{-2} M_{\odot}$, 1020 yrs., $5.81 \times 10^{-5} M_{\odot} \text{yr}^{-1}$.

5.2. J051848.84-700247.0

This object is classified as a post-AGB shell source by KWVW15, with $T_{eff} = 6015 \text{ K}$, $\log g = 0.0$ and $[Fe/H] = -1.0$ based on their STP. However, Table 3 in KWVW15 suggests that using high resolution spectra van Aarle et al. (2013) estimate $\log g = 0.5$. We could not find the object in the paper by van Aarle et al. (2013). Hence, we used a Kurucz stellar atmosphere model with $T_{eff} = 6000 \text{ K}$, $\log g = 0.0$ and $[Fe/H] = -1.0$. Based on Vizier, for the R-band magnitude we used 14.80 ± 0.44 (GSC 2.2 Catalogue/STScI 2001)³ We modeled the SED of the object (Fig. 11.1, $\chi^2 = 50.4$) using T_d (in) = 350 K, standard MRN grain size distribution, $\tau = 3.2$ and $Y = 20$. Figs. 11.2 – 11.4 show the effects of varying T_d , τ and Y . Since a single shell model provided satisfactory fits to the optical and IR fluxes, we did not try a two-component model for this object.

We estimate a luminosity of $6210L_{\odot}$. KWVW15 obtained vastly different values for the observed and photospheric luminosity of the object, $4477L_{\odot}$ and $14112L_{\odot}$ respectively. Their observed luminosity is obtained by integrating the flux under the observed SED. In the event of circumstellar dust and reddening, the former may be significantly less than the actual luminosity. Their derived photospheric luminosity depends on the extinction correction applied to the observed V-magnitude. KWVW15's formalism attempts to account for both interstellar and circumstellar reddening. If the V-magnitude is over-corrected, they would derive a higher luminosity for the object.

From our best-fit model, the total mass accumulated in the shell is $1.76 \times 10^{-2} M_{\odot}$ over 1100 years at a mass-loss rate of $1.6 \times 10^{-5} M_{\odot} \text{yr}^{-1}$.

5.3. J051906.86-694153.9

This object is classified as a post-AGB shell source by KWVW15, with $T_{eff} = 5613 \text{ K}$, $\log g = 0.0$ and $[Fe/H] = -1.3$. The WISE and ALLWISE W3 and W4 data are discrepant for this source, with ALLWISE reporting upper limits significantly lower than the WISE magnitudes. Given the good agreement between the Spitzer MIPS $24 \mu\text{m}$ and the WISE W4 fluxes, we have chosen to ignore the ALLWISE W3 and W4 data for this source. We used a Kurucz stellar atmosphere model with $T_{eff} = 5500 \text{ K}$, $\log g = 0.0$ and $[Fe/H] = -1.5$. A single shell model could not simultaneously fit the observed flux distribution from the optical to the far-IR. Similar to the case of the post-AGB star, J050632.10-714229.8, we assumed a pair of nested shells. A fit to the optical, mid- and far-IR data was obtained using amC-Hn grain type, standard MRN grain size distribution, T_d (in) = 2000 K, $\tau = 0.35$ and $Y = 2.0$ (Fig. 12.1). The radiation emerging from this warm shell illuminates a cold outer shell of SiC-Pg grains with modified MRN grain size distribution: $a_{min} = 2.3 \mu\text{m}$, $a_{max} = 3.0 \mu\text{m}$, T_d (in) = 160 K, $\tau = 0.07$ and $Y = 2.0$. Fig. 12.2 ($\chi^2 = 21.3$) shows the correctly illuminated nested shell model. In calculating the reduced chi-square for this source, we used the WISE W3 and W4 fluxes.

We estimate a luminosity of $2018L_{\odot}$. This is in good agreement with the observed luminosity estimated by KWVW15 ($2052L_{\odot}$). However, as in the case of the post-AGB star, J051848.84-700247.0, KWVW15 report vastly different values for the observed and photospheric luminosities of the object, $2052L_{\odot}$ and $4246L_{\odot}$ respectively. From our best-fit model, the total mass accumulated in the shell is $1.78 \times 10^{-4} M_{\odot}$ over a period of 51.4 years at a mass loss rate of $3.46 \times 10^{-6} M_{\odot} \text{yr}^{-1}$.

5.4. J053250.69-713925.8

³ We did not use KWVW15's R-band magnitude (14.31) because we could not find a corresponding reference.

This object is classified as a post-AGB shell source by KWVW15, with $T_{eff} = 6073\text{K}$, $\log g = 1.0$ and $[Fe/H] = -1.1$. Based on high resolution spectra, van Aarle et al. (2013) obtained $T_{eff} = 5500\text{K}$, $\log g = 0.0$ and $[Fe/H] = -1.0$. We prefer the van Aarle et al. (2013) values based on their high resolution data. Hence, we used a Kurucz stellar atmosphere model with $T_{eff} = 5500\text{K}$, $\log g = 0.0$ and $[Fe/H] = -1.0$. A single shell model gave a reasonable fit to the near, mid and far-IR data (Fig. 13.1, $\chi^2 = 214.4$). The fit was obtained for T_d (in) = 260 K, using a mix of silicate (Sil-Ow/0.2) and graphite (grf-DL/0.8) grains, modified MRN grain size distribution: $a_{min} = 0.005\ \mu\text{m}$, $a_{max} = 0.50\ \mu\text{m}$, $\tau = 0.9$ and $Y = 2$. The presence of graphite dust indicates that it is a carbon-rich post-AGB star. Hence, the mismatch at IRAC3 (5.8 μm) and IRAC4 (8 μm) may be attributed to PAH emissions.

We estimate a luminosity of $4657.0L_{\odot}$. This is in good agreement with the observed luminosity estimated by KWVW15 ($4223L_{\odot}$). However, similar to the case of the post-AGBs, J051848.84-700247.0 (§ 5.2) and J051906.86-694153.9 (§ 5.3), KWVW15 estimated a much higher photospheric luminosity, $11056L_{\odot}$. From our best-fit model, the total mass accumulated in the shell is $6.45 \times 10^{-3}M_{\odot}$ over a period of 144 years at a mass loss rate of $4.48 \times 10^{-5}M_{\odot}\text{yr}^{-1}$.

5.5. J045623.21-692749.0

This object is classified as a post-AGB disk source by KWVW15, with $T_{eff} = 4500\text{K}$, $\log g = 0.0$ and $[Fe/H] = -1.0$. We used a Kurucz stellar atmosphere model with these parameters. A single shell model (Fig. 14.3) could not provide a fit to the far-IR data. An overall fit from the optical to the far-IR could be obtained under two scenarios: (1) a nested shells model (# 1) as in the case of the post-AGB shell sources J050632.10-714229.8 and J051906.86-694153.9 and (2) a two-component model with a warm inner disk and a cold outer shell (model # 2).

In case of the former (# 1), the inner shell is composed of Sil-Ow grains with modified MRN grain size distribution: $a_{min} = 0.005\ \mu\text{m}$ and $a_{max} = 5.0\ \mu\text{m}$, T_d (in) = 1100 K, $\tau = 0.6$ and $Y = 3.0$. The outer shell is composed of Sil-Ow grains with standard MRN grain size distribution, T_d (in) = 150 K, $\tau = 0.10$ and $Y = 2.0$. Fig. 14.1 ($\chi^2 = 100.2$) shows the correctly illuminated nested shells model.

In the second scenario (# 2), the warm inner disk (T_d (in) = 1100 K) is composed of amC-Hn grains and the cold outer shell (T_d (in) = 400 K) is made up of Sil-Ow grains. The amC-Hn disk was approximated as a wedge-shaped fraction (0.5) of a sphere with $\tau = 0.5$, $Y = 2$ and modified MRN grain size distribution: $a_{min} = 0.005\ \mu\text{m}$ and $a_{max} = 2.0\ \mu\text{m}$. The Sil-Ow shell has modified MRN grain size distribution: $a_{min} = 0.40\ \mu\text{m}$ and $a_{max} = 1.0\ \mu\text{m}$, $\tau = 0.22$ and $Y = 15$. The correctly illuminated model SED is shown in Fig. 14.2 ($\chi^2 = 195.2$).

Based on the reduced chi-square values, we adopt the nested shells model (# 1) as the best-fit. The estimated luminosity based on this model is $6598L_{\odot}$. KWVW15 gave an observed luminosity estimate of $6864L_{\odot}$ and a photospheric luminosity of $7131L_{\odot}$. The total mass accumulated in the outer shell is estimated to be $8.25 \times 10^{-4}M_{\odot}$ in 225 years at a mass-loss rate of $3.7 \times 10^{-6}M_{\odot}\text{yr}^{-1}$.

5.6. J051418.09-691234.9

This object has been classified as a post-AGB disk source (KWVW15), a population II Cepheid variable (Soszyński et al. 2008) and a RV Tauri star (van Aarle et al. 2011). KWVW15 estimated $T_{eff} = 6112\text{K}$, $\log g = 0.5$ and $[Fe/H] = -1.6$. We adopted Kurucz stellar atmosphere model with $T_{eff} = 6000\text{K}$, $\log g = 0.5$ and $[Fe/H] = -1.5$. For the R magnitude we used 13.78⁴ from the NOMAD catalog (Zacharias et al. 2005).

A reasonable fit to the near, mid and far-IR data (Fig. 15.1, $\chi^2 = 98.0$) is obtained assuming an inner disk (T_d (in) = 1100 K) composed of amorphous carbon (amC-Hn) with modified MRN grain size distribution: $a_{min} = 0.005\ \mu\text{m}$, $a_{max} = 2.0\ \mu\text{m}$, $\tau = 5.0$ and $Y = 15.0$. The disk is assumed to be a wedge-shaped fraction (0.25) of a sphere. The outer shell (T_d (in) = 600 K) is composed of silicate (Sil-Ow/0.4) and graphite (grf-DL/0.6) grains with standard MRN grain size distribution, $\tau = 0.4$ and $Y = 30.0$. Since the inner disk is optically thick, similar to the post-RGB star, J055102.44-685639.1 (§ 4.8) we cannot apply the ‘‘correctly illuminated model’’ formalism to this object.

The variable nature of the star may explain the difference between the WISE (ALLWISE) and IRAC data at their bands 1 and 2 ($\sim 3.5\ \mu\text{m}$ and $4.5\ \mu\text{m}$) as also the mismatch between model and observed I-band data. ALLWISE photometry at bands 1 (3.4 μm) and 2 (4.6 μm) is generally an improvement over the WISE data at these wavelengths (§ 6.3.4). From our best-fit model, the luminosity of the object is $7763L_{\odot}$. KWVW15 obtained $6667L_{\odot}$ for the observed luminosity and $4703L_{\odot}$ for the photospheric luminosity. The total mass accumulated in the shell is estimated to be

⁴ We did not use KWVW15’s R-band magnitude (13.96) because we could not find a corresponding reference.

$1.21 \times 10^{-3} M_{\odot}$ over 800 years at a mass-loss rate of $1.51 \times 10^{-6} M_{\odot} \text{ yr}^{-1}$. The total mass in the disk is $4.67 \times 10^{-5} M_{\odot}$ over 220 years at a mass-loss rate of $2.12 \times 10^{-7} M_{\odot} \text{ yr}^{-1}$.

5.7. J055122.52-695351.4

This object has been classified as a post-AGB disk source (KWVW15), a Population II Cepheid variable (Soszyński et al. 2008) and a RV Tauri star (van Aarle et al. 2011). KWVW15 estimated $T_{eff} = 6237$ K, $\log g = 1.5$ and $[Fe/H] = -2.5$ for the star. We used a Kurucz stellar atmosphere model with $T_{eff} = 6250$ K, $\log g = 1.5$ and $[Fe/H] = -2.5$. The difference between the WISE (ALLWISE) and IRAC fluxes at bands 1 and 2 ($\sim 3.5 \mu\text{m}$ and $4.5 \mu\text{m}$) may be attributed to the variable nature of the object.

A reasonable fit to the near, mid and far-IR data could be obtained assuming a single shell model (Fig. 16.1, $\chi^2 = 41.8$) with a mix of graphite (grf-DL/0.7) and amorphous carbon (amC-Hn/0.3) grains, modified MRN grain size distribution: $a_{min} = 0.05 \mu\text{m}$, $a_{max} = 0.3 \mu\text{m}$, T_d (in) = 450 K, $\tau = 0.78$ and $Y = 6$.

We obtained a luminosity of $4116 L_{\odot}$ for the object in close agreement with the observed ($3780 L_{\odot}$) and photospheric ($3657 L_{\odot}$) luminosity estimated by KWVW15. The total mass accumulated in the shell is estimated to be $1.18 \times 10^{-3} M_{\odot}$ in 243 years at a mass-loss rate of $4.86 \times 10^{-6} M_{\odot} \text{ yr}^{-1}$.

5.8. J052519.48-705410.0

This object has been classified as a post-AGB disk source (KWVW15), a Population II Cepheid variable (Soszyński et al. 2008) and a RV Tauri star (van Aarle et al. 2011). KWVW15 estimated $T_{eff} = 8117$, $\log g = 1.0$ and $[Fe/H] = -0.5$. We used a Kurucz stellar atmosphere model with $T_{eff} = 8000$ K, $\log g = 1.0$ and $[Fe/H] = -0.5$. There is a significant difference between the WISE (ALLWISE) and IRAC fluxes at bands 1 and 2 ($\sim 3.5 \mu\text{m}$ and $4.6 \mu\text{m}$) which may (at least partly) be due to the photometric variability. We have chosen to fit the IRAC data, and have excluded the WISE(ALLWISE) fluxes at $3.6 \mu\text{m}$, $4.6 \mu\text{m}$ and $12 \mu\text{m}$ for estimating the reduced chi-square.

Single shell models #1 and #2 (Fig. 17.1) could not provide simultaneous fit to the near, mid and far-IR data. Using Sil-Ow grains a fit could be obtained to the near and far-IR fluxes (model #1) while single shell grf-DL model (model #2) provided a fit to the near-IR and IRAC ($3.6 \mu\text{m}$, $4.5 \mu\text{m}$ and $5.8 \mu\text{m}$) fluxes.

Hence we tried two-component model fits to the observed SED. Fig. 17.2 shows the best-fit two-component model for J052519.48-705410.0 (model #3, $\chi^2 = 35.9$). The warm inner disk (T_d (in) = 800 K) is approximated as a wedge-shaped fraction (0.35) of a sphere and is made up of Sil-Ow grains with standard MRN grain size distribution, $\tau = 1.0$ and $Y = 20$. The outer shell (T_d (in) = 600K) is made up of grf-DL grains with modified MRN grain size distribution: $a_{min} = 0.005 \mu\text{m}$, $a_{max} = 0.5 \mu\text{m}$, $\tau = 0.8$ and $Y = 2.0$. Since the inner disk is optically thick, we cannot apply the ‘‘correctly illuminated model’’ formalism to this object.

From our best-fit model #3, we estimated a luminosity of $3804 L_{\odot}$. KWVW15 obtained $3219 L_{\odot}$ and $4943 L_{\odot}$ respectively for the observed and photospheric luminosities. The total mass in the disk and shell was estimated to be $3.64 \times 10^{-5} M_{\odot}$ and $1.25 \times 10^{-4} M_{\odot}$ respectively. The age of the disk is estimated to be 451 years while the shell is ~ 20 years old. The mass loss rates for the disk and shell respectively are $8.08 \times 10^{-8} M_{\odot} \text{ yr}^{-1}$ and $6.12 \times 10^{-6} M_{\odot} \text{ yr}^{-1}$.

6. DISCUSSION

6.1. Common envelope evolution and ejecta mass

When the primary in a binary system overflows its Roche lobe and the resulting mass transfer proceeds too rapidly to be accreted by the compact companion, a CE system results. CEE (Paczynski 1976; Ivanova et al. 2013) may give rise to close binary systems. Two scenarios may exist — a rapid plunge in of the companion or a slow spiral-in phase. In the former, if enough orbital energy is deposited to the CE via dynamical friction, the whole envelope is ejected on a dynamical timescale (Paczynski 1976). The second case provides an alternate route for the envelope ejection (Ivanova et al. 2002; Podsiadlowski et al. 2010) over ‘several dynamical time scales’ (Ivanova et al. 2013; Clayton et al. 2017). Recently, a third scenario has been proposed by Glanz & Perets (2018) wherein dust driven winds similar to those observed in AGB stars may lead to the ejection of the CE.

Following the ejection of the CE, dust formation may occur in the expanding gas (Lü et al. 2013; Iaconi et al. 2020) which may explain the presence of circumstellar dust shells in these systems. Some fraction of the ejected mass may also fall back and interact with the binary leading to the formation of circumbinary disks (Kashi & Soker 2011).

Lü et al. (2013) discuss dust formation in the CE ejecta of binary systems wherein the giant is on the RGB (they call it the first giant branch or FGB) and the companion is a $1 M_{\odot}$ degenerate star. Since RGB stars are expected to

be oxygen-rich following the first dredge-up, they use only olivine, pyroxene, and quartz-type silicates and iron grains for discussion. They find that silicate and iron-rich dust in the CE ejecta can form over a very wide range of radial distances ($10^{14} - 10^{18}$ cm) from the RGB star (Fig. 5, Lü et al. (2013)) which easily encompasses our R_{in} values for the cold dust shells from our best-fit models (Table 2). In Lü et al.’s models, the mass of dust produced in the CE ejecta of giants with masses $1-7 M_{\odot}$ ranges from about $10^{-9} M_{\odot}$ to $10^{-2} M_{\odot}$. The lower end of this mass range corresponds to CEE occurring at the base of the RGB and the model parameter $\gamma = 0.2$ (see eqn. 2 of Lü et al. (2013) for a definition of γ). Higher values of γ result in CE ejecta with relatively higher densities, and thus more efficient dust formation. Thus, the upper end of the ejecta mass range corresponds to CEE occurring anywhere between the base and the tip of the RGB with $\gamma \geq 0.3$, or at the tip of the RGB with $\gamma \geq 0.2$ (Fig. 2, Lü et al. (2013)).

For our sample of post-RGB objects, the values of total mass, M_{gd} in the outer shell range from about $4 \times 10^{-5} M_{\odot}$ to $3 \times 10^{-2} M_{\odot}$ (Table 4) – inferred from our model dust masses, M_d that lie in the range $2 \times 10^{-7} M_{\odot} - 1.5 \times 10^{-4} M_{\odot}$. We compare our dust mass estimates with those of Lü et al. (2013) in Fig. 18. Since our derived masses are likely lower limits to the total dust mass, its most likely that either $\gamma \geq 0.3$ and/or CEE has occurred near or at the tip of the RGB for our post-RGB sources. Lü et al. (2013) were pessimistic about the difficulty to observe the dust produced in CE ejecta, since “the distance of dust formation in the CE ejecta is between $\sim 10^{14}$ and $\sim 10^{18}$ cm and is relatively far away from the FGB star”; however our study clearly shows that dust is relatively easily detected in our sample of post-RGB sources between $\text{few} \times 10^{14}$ and $\sim 10^{18}$ cm. Dust formation in CE ejecta wherein the primary is a RGB star has also been studied by Iaconi et al. (2020) using a 3D SPH hydrodynamic simulation. Their range of dust masses obtained were comparable to that of Lü et al. (2013).

6.2. “Disk” and “Shell” source classification

KWVW15 classified the post-RGB and post-AGB sources into two groups – “disk” and “shell” (Van Winckel 2003), based on their SEDs. The “disk” sources are inferred to have a stable compact circumbinary disk and are confirmed binaries (with orbital periods, $P_{orb} \sim 100 - 2000$ d), whereas the “shell” sources have not resulted (so far) in any clear detected binary orbit (Hrivnak et al. 2011), suggesting that these are either single-stars or have companions with relatively very wide orbits.

However, our modeling shows that the KWVW15 “shell”/“disk” classification is not robust. All “disk” sources in our sample require the presence of “shells”. In addition, we find the presence of a disk in some “shell” sources (J043919.30-685733.4 and J051920.18-722522.1), and we exclude the presence of a disk in some “disk” sources (J045623.21-692749.0 and J045623.21-692749.0).

We find that the disk fractions are surprisingly large (typically 0.3–0.4), implying disks with large opening angles ($\sim 41^{\circ} \pm 6^{\circ}$) and hence geometrically thick structures. The large opening angles appear to be roughly consistent with the gas density of the ejected envelope as seen in numerical simulations of CEE, relatively soon after CEE occurs e.g., see Fig. 1 of García-Segura et al. (2018). It appears unlikely that the “disk” structures in our models represent the stable compact circumbinary disks envisaged by Van Winckel (2003), although it is possible that the latter reside within the former. The inner rims of circumbinary disks may be puffed up, as suggested by the modeling of near and mid-IR interferometric imaging of the disk structure in the post-AGB star IRAS 08544-4431 (Deroo et al. 2007), and may mimic the physical effect of absorbing a substantial part of the direct stellar radiation within a relatively large solid angle.

6.2.1. Source Luminosities

We summarize our derived model stellar luminosities, together with those provided by KWVW15 in Tables 6 (for post-RGB sources) and 6 (for post-AGB sources). We find that our values are in reasonable agreement with KWVW15’s observed values. For a few objects where KWVW15’s observed and photospheric values are very discrepant, our model values provide a more accurate estimate of the stellar luminosities.

6.2.2. Ages of the dusty disks and shells

A comparison of the ages of the disk and shells can be potentially useful for constraining details of the physical mechanism responsible for the transition of RGB stars directly (i.e., without ascending the AGB) towards the PN phase, which has been argued to be CEE. For example, in the Boomerang Nebula, the age of the central disk structure is estimated to be 1925 yr, less than the age of the shell of $\gtrsim 3840$ yr, which implies that the disk was formed after the (inferred) companion entered the CE, resulting in the ejection of the primary red giant star’s envelope and the subsequent merging of the companion with the primary’s core. In general, we find that the disk age is generally lower

than the shell age for the objects in our study with the exception of the post-RGB object, J045555.15-712112.3 and the post-AGB object, J052519.48-705410.0. Our estimate for the age depends on (i) the assumed expansion velocities for the disk and the shell respectively (V_{exp}) and (ii) on the thickness of the shell/disk (Y).

Our derived Y value is likely a lower limit to the estimated shell thickness. We illustrate this point with the post-RGB objects, J045755.05-681649.2 ($Y = 30$) and J051920.18-722522.1 ($Y = 20$). In Figs. 4.2 and 7.4, we plot the correctly illuminated two-component models for the objects with the thickness of the outer shell increased by a factor of 10, i.e. $Y = 300$ and 200 respectively. No noticeable change is observed in the fits. The derived model parameters corresponding to these fits are given in 2. In the absence of data beyond $24 \mu\text{m}$, it is quite plausible that the shell is even more extended (i.e. the actual value of Y is much larger than in our model) For example, in the post-AGB object, IRAS 22036+5306, where the modeled SED included data up to $\sim 200 \mu\text{m}$ the outer radius of the shell is a factor ~ 40 larger than the inner radius (Sahai et al. 2006). A thicker outer shell in J045555.15-712112.3 would translate into a larger value for the shell age.

The post-AGB star, J052519.48-705410.0 has been classified as a Cepheid (Soszyński et al. 2008) and a RV Tauri variable (van Aarle et al. 2011). The variable nature of this object is also evidenced by the difference between the IRAC and WISE (ALLWISE) fluxes (§ 5.8). The disk being older than the shell is consistent with the RV Tauri classification of the object (Waters et al. 1993). In RV Tauri systems, the hot dust is believed to be related to the presence of a companion and may be the remnant of a phase of high mass loss in the past or rapid mass transfer during Roche lobe overflow. The outer shell is usually related to more recent mass-loss history (Van Winckel et al. 1999; Waters et al. 1993).

6.2.3. RV Tauri post-AGB stars

The post-AGB disk stars, J051418.09-691234.9, J052519.48-705410.0, J055122.52-695351.4 are known RV Tauri variables (van Aarle et al. 2011). Galactic RV Tauri variables with infrared excess are almost always associated with circumstellar disks, e.g. (Lloyd Evans 1995; Van Winckel et al. 1999; Gielen et al. 2007) The RV Tauri stars in the LMC may also be expected to show similar morphology (Manick et al. 2018). However, our model SEDs show that although J052519.48-705410.0 and J055122.52-695351.4 harbour a warm inner disk in addition to the outer shell, the observed SED of the RV Tauri star, J055122.52-695351.4 did not require a circumstellar disk, as it could be fitted by a single shell model (Fig. 16.1).

6.3. Systematic discrepancies in SED Modeling

In this section, we discuss some systematic discrepancies between the model and observed SEDs and their implications. Some of these may be due to the presence of dust emission features – JWST/MRS spectroscopy will be needed to test this hypothesis. Other discrepancies may be related to systematic uncertainties in the photometry.

6.3.1. PAH emission

We find systematic discrepancies between the model and observed SEDs in the $5.8\text{--}8 \mu\text{m}$ region for some of our post-RGB sources – J043919.30-685733.4, J045555.15-712112, J045755.05-681649.2 and J050257.89-665306.3. These discrepancies may be explained by the presence of PAHs in the dust disks/shells of our sources.

We discuss two possibilities that may account for the presence of PAH molecules in oxygen-rich post-RGB stars. Both of these have been discussed by Jura et al. (2006) for the case of HD233517, an evolved oxygen-rich red giant showing PAH features in the circumstellar environment. In the first scenario, since the dusty post-RGB stars in our sample are most likely in close binary systems, the companion of the post-RGB star which may have been more massive than the latter on the MS, may have evolved to become a C-rich AGB star and transferred C-rich material to the post-RGB star progenitor, making it carbon-rich⁵; then, the post-RGB progenitor, when it evolved to become a red giant underwent a CE interaction with the companion (then a WD), ejecting C-rich material that made PAHs. Another possible scenario is that when the more massive star of the binary pair became a red giant, it engulfed the secondary, and the mass transfer and resulting ejection of circumstellar matter via CEE that followed harbored the required physical conditions for the formation of PAHs. For example, Fischer-Tropsch catalysis on the surface of iron grains (Willacy 2004) converted much of the carbon initially contained in CO into hydrocarbons, and subsequently, analogous to the atmospheric chemistry in Jupiter (Wong 2003), these simple hydrocarbons were converted into PAHs.

⁵ this mechanism is believed to be responsible for dwarf carbon stars and CH stars

PAH emission is believed to be the result of excitation of the PAH molecules and/or photodissociation of the CO molecule in dense torii. The latter is believed to account for the presence of PAH emission features in O-rich circumstellar environments of post-AGB stars, PPNe and PNe (Beintema et al. 1996; Waters et al. 1998; Matsuura et al. 2004; Cerrigone et al. 2009; Guzman-Ramirez et al. 2011). It is widely accepted that UV flux is required for both these mechanisms. However, UV flux cannot account for the excitation of PAH molecules in the circumstellar environment of post-RGB stars, because of their low T_{eff} . Li & Draine (2002) argue that UV flux is not imperative for the excitation of PAH molecules – depending on the sizes of the PAH molecules, these may be excited by photons covering a wide range of wavelengths. In particular, it is possible for PAH molecules to be excited by photons longwards of UV wavelengths – in fact, PAH emission may be observed even if the effective temperature of the exciting star is as low as 3000 K.

6.3.2. Silicate emission feature

The $\sim 10 \mu\text{m}$ amorphous silicate emission feature is visible in the model spectra of several of our objects. We illustrate the effects of choice of silicate grains (Sil-Ow, Sil-Oc), dust temperature at the inner boundary of the dust shells (T_d) and maximum grain size on the silicate emission feature, using the post-AGB (shell) source, J050632.10-714229.8 as an example. Changing the grains from “warm” (Sil-Ow) to “cold” (Sil-Oc) silicates doesn’t do much to alter the fit in the mid-IR (Fig. 10.2). The silicate emission feature is also not very sensitive to changing T_d (Fig. 10.7). Incorporating larger Sil-Ow grains in the inner shell has the effect of broadening the wings of the silicate emission feature while reducing its intensity. Fig. 10.8 shows the fits for different values of a_{max} .

6.3.3. R and I band data

For several of our post-RGB and post-AGB sources, the model SEDs do not provide good matches to the R- and I-band data. The R magnitudes, taken from the GSC 2.2 catalog (as in KWVW15), often have large error bars, e.g. the post-RGB sources, J051347.57-704450.5 and J051920.18-722522.1. The modeled SEDs do not agree with the extinction corrected Rmag even after taking into account the large error bars. For the post-RGB source J051347.57-704450.5, in addition to the GSC 2.2 data, we plotted the extinction corrected USNO-B 1.0 R1 and R2 fluxes (Fig. Set 3). We find that the latter are in better agreement with the modeled SED.

KWVW15 compiled I magnitudes from the MCPS Catalog for the LMC (Zaritsky et al. 2004). In Table 5 we compare the I-band magnitudes from Zaritsky et al. (2004) with data from the DENIS catalog (Cioni et al. 2000) and USNO-B 1.0 (Monet et al. 2003). The Zaritsky et al. (2004) data is in good agreement with the DENIS data with the exception of the post-RGB source, J050257.89-665306.3 ($\Delta\text{Imag} \sim 1 \text{ mag}$). The corrected DENIS Imag for this object is in good agreement with our modeled SED, Fig. 8.2. In most cases, the USNO-B 1.0 magnitudes are brighter than the Zaritsky et al. (2004) data and would show better agreement with our modeled SEDs.

6.3.4. WISE and ALLWISE photometry

The WISE magnitudes from the All-Sky Data Release Cutri et al. (2012) and the ALLWISE magnitudes (Cutri et al. 2013) are listed in Table 1. A mismatch between modeled and observed SEDs at WISE band 2 (W2/4.6 μm) was observed for the post-RGB sources, J043919.30-685733.4, J045555.15-712112.3 and J045755.05-681649.2. Hence, we additionally plotted the ALLWISE magnitudes of the sources from Vizier. Because of processing improvements in compiling the photometric data and the addition of a second coverage of the sky in the short wavelength bands, ALLWISE achieves better sensitivity in bands 1 and 2. The latter data shows good agreement with our modeled SEDs for J043919.30-685733.4 (Figs. 2.8, 2.9), J045755.05-681649.2 (Fig. 7.2) and J045555.15-712112.3 (Fig. 6.4). Similarly, we notice a mismatch between modeled and observed SEDs for the post-AGB “disk” sources in the WISE band 1 and 2 fluxes. When the mismatch between WISE and ALLWISE data significantly exceeds the error in the observed photometry, it may be due to source variability. Three of the post-AGB disk sources, J051418.09-691234.9, J052519.48-705410.0, J055122.52-695351.4 are known RV Tauri variables (§ 6.2.3).

7. CONCLUSIONS

We have modeled the SEDs of a select sample of post-RGB and post-AGB objects (8 in each class) in the LMC, drawn from a large list of such sources classified as possessing “disks” or “shells” based on the shape of their SEDs. A circumstellar disk suggests binarity. Close binary systems undergoing CEE can result in the premature evolution of an RGB star into a PNe. We have used the 1-D radiative transfer code, DUSTY, approximating disk structures

as wedge-shaped fractions of a sphere (disk-fractions). We have derived the total dust mass (and using an assumed gas-to-dust ratio, the total mass of gas) in the disks and shells, and set constraints on the dust grain composition and sizes. Our main conclusions are listed below:

1. The masses of ejecta in the disks of post-RGBs (disks/inner shells of post-AGBs) lie in the range $\sim 9 \times 10^{-9} - 3 \times 10^{-5} M_{\odot}$ ($\sim 9 \times 10^{-9} - 7 \times 10^{-4} M_{\odot}$) and in the outer shells from $\sim 4 \times 10^{-5} - 3 \times 10^{-2} M_{\odot}$ ($\sim 1 \times 10^{-4} - 6 \times 10^{-2} M_{\odot}$). On average, the shell masses in post-RGBs are less than those in post-AGBs, with the caveat that a substantial amount of mass in both types of objects may lie in an extended cold shell, that is detectable only at wavelength longwards of the MIPS 24 μm band.
2. The disk fractions are surprisingly large (typically 0.3–0.4), implying that the disks are geometrically thick structures with a substantial opening angle ($\sim 41^{\circ} \pm 6^{\circ}$). The large opening angles appear to be roughly consistent with the latitudinal variation of gas density in the ejected envelope as seen in numerical simulations of CEE, relatively soon after CEE occurs.
3. We find evidence that for some post-RGB sources the ejected matter may be carbon-rich, even though it is expected to be oxygen-rich. For J055102.44-685639.1, the inner disk is composed of amorphous carbon grains and the outer shell has a mix of silicate and silicon carbide grains. In addition, for J043919.30-685733.4, J045555.15-712112, J045755.05-681649.2 and J050257.89-665306.3, PAH emission may account for the discrepancy between model and observed SEDs. The presence of PAHs provides independent support for the hypothesis of binary interaction leading to the formation of post-RGB objects.
4. We find that the published classification of these objects as “shell” or “disk” sources is not robust. Our modeling shows the presence of a disk is (a) required in some “shell” sources (the post-RGB sources: J043919.30-685733.4 and J051920.18-722522.1), and (b) not required in some “disk” sources (the post-AGB sources: J045623.21-692749.0 and J055122.52-695351.4).
5. Comparison of our model dust mass values with the predictions of models of CEE on the RGB that produce dust suggest that CEE occurred near or at the tip of the RGB for the post-RGB sources in our sample.

We thank our anonymous referees for their meticulous reviews of our paper, which have helped us improve it. G.S. would like to acknowledge financial support from the Department of Science and Technology (DST), Government of India, through a grant numbered SR/WOS-A/PM-93/2017. R.S.’s contribution to the research described here was carried out at the Jet Propulsion Laboratory, California Institute of Technology, under a contract with NASA, and funded in part by NASA via ADAP awards, and multiple HST GO awards from the Space Telescope Science Institute.

REFERENCES

- Acke, B., Degroote, P., Lombaert, R., de Vries, B.L. et al. 2013, *A&A*, 551, 76
- Beintema, D. A., van den Ancker, M. E., Molster, F. J. et al. 1996, *A&A*, 315, L369
- Bujarrabal, V., Castro-Carrizo, A., Alcolea, J, Sánchez Contreras, C. 2001, *A&A*, 377, 868
- Cutri, R. M., Wright, E. L., Conrow, T. et al. 2012, Explanatory Supplement to the WISE All-Sky Data Release Products. Tech. rep.
- Cutri, R. M., Wright, E. L., Conrow, T. et al. 2013, Explanatory Supplement to the ALLWISE Data Release Products. Tech. rep. the WISE All-Sky Data Release Products. Tech. rep.
- Cerrigone, L., Hora, J. L., Umana, G. & Trigilio, C. 2009, *ApJ*, 703, 585
- Cioni, M. -R., Loup, C., Habing, H. J. et al. 2000, *A&AS*, 144, 235
- Clayton, M., Podsiadlowski, P., Ivanova, N., Justham, S. 2017, *MNRAS*, 470, 1788
- Demyk, K., Meny, C., Leroux, H. et al. 2017, *A&A*, 606, 50
- Deroo, P., Acke, B., Verhoelst, T., et al. 2007, *A&A*, 474, L45
- Draine, B. T. & Lee, H. M. 1984, *ApJ*, 285, 89
- Ferrarotti, A. S. & Gail, H. 2006, *A&A*, 447, 553
- Gail, H. P., Zhukovska, S. V., Hoppe, P., Trieloff, M. 2009, *ApJ*, 698, 1136

- Gao, Jian, Jiang, B. W., Li, Aigen & Xue, M. Y. 2013, *ApJ*, 776, 7
- Gordon, K. D., Clayton, G. C., Misselt, K. A., Landolt, A. U. & Wolff, M. J. 2003, *ApJ*, 594, 279
- Gruendl, R. A., Chu, You-Hua 2009, *ApJS*, 184, 172
- Guzman-Ramirez, L., Zijlstra, A. A., Níchuimín, R., et al. 2011, *MNRAS*, 414, 1667
- García-Segura, G., Ricker, P. M., & Taam, R. E. 2018, *ApJ*, 860, 19
- Glanz, H., Perets, H.B. 2018, *MNRAS*, 478, L12
- Gielen, C., Van Winckel, H., Waters, L. B. F. M., Min, M., & Dominik, C. 2007, *A&A*, 475, 629
- Hanner, M.S. 1988, *NASA Conf. Pub.* 3004, 22
- Höfner, S., Olofsson, H. 2018, *A&ARv*, 26, 1
- Hrivnak, B. J., Lu, W., Bohlender, D., Morris, S. C., Woodsworth, A. W., Scarfe, C. D. 2011, *ApJ*, 734, 25
- Iaconi, R., Maeda, K., Nozawa, T., De Marco, O., Reichardt, T. 2020, *MNRAS*, 497, 3166
- Ivanova, N., Podsiadlowski, P., Spruit, H. 2002, *MNRAS*, 334, 819
- Ivanova, N., Justham, S., Chen, X., et al. 2013, *The Astronomy and Astrophysics Review*, 21, 59
- Ivezić, Z., Nenkova, M., Heymann, F. & Elitzur, M. 2012, *User Manual for DUSTY (V4)*
- Jura, M., Kahane, C. 1999, *ApJ*, 521, 302
- Jura, M., Bohac, C. J., Sargent, B., Forrest, W. J. et al. 2006, *ApJ*, 637, L45
- Kashi, Amit, Soker, Noam 2011, *MNRAS*, 417, 1466
- Kamath, D., Wood, P. R. & Van Winckel, H. 2014, *MNRAS*, 439, 2211
- Kamath, D., Wood, P. R. & Van Winckel, H. 2015, *MNRAS*, 454, 1468
- Kamath, D., Wood, P. R., Van Winckel, H., & Nie, J.D. 2016, *A&A*, 586, L5
- Kamath, D. & Van Winckel, H. 2019, *MNRAS*, 486, 3524
- Keller, S. C. & Wood, P. R. 2006, *ApJ*, 642, 834
- Lacy, J. H., Baas, F., Allamandola, L. J., Persson, S. E. et al. 1984, *ApJ*, 276, 533
- Li, Aigen and Draine, T. 2002, *ApJ*, 572, 232
- Lloyd Evans, T. 1995, *Ap&SS*, 230, 169
- Lü, G., Zhu, C., Podsiadlowski, P. 2013, *ApJ*, 768, 193
- Manick, R., Van Winckel, H., Kamath, D., Sekaran, S. & Kolenberg, K 2018, *A&A*, 618, 21
- Mathis, J. S., Rumpl, W. & Nordsieck, K. H. 1977, *ApJ*, 217, 425
- Matsuura, M., Zijlstra, A. A., Molster, F. J. et al. 2004 *ApJ*, 604, 791
- Meixner, M., Gordon, K. D., Indebetouw, R., Hora, J. L. et al. 2006, *AJ*, 132, 2268
- Monet, D. G., Levine, S. E., Canzian, B. 2003, *AJ*, 125, 984
- Nanni, A., Groenewegen, M. A. T., Aringer, B. et al. 2019, *MNRAS* 487, 502
- Nyman, L. -Å., Booth, R. S., Carlström, U. et al. 1992, *A&AS*, 93, 121
- Olofsson, H. 1993, in Schwarz H.E., ed., *Second ESO/CTIO workshop, Mass loss on the AGB and beyond. ESO Conference and Workshop Proceedings No. 46*, Garching, p.330
- Ossenkopf, V., Henning, Th. & Mathis, J. S. 1992, *A&A*, 261, 567
- Paczynski, B. 1976, in *IAU Symposium, Vol. 73*, p. 75, *Structure and Evolution of Close Binary Systems*, eds. Eggleton, P., Mitton, S., Whelan, J.
- Pégourié, B. 1988, *A&A*, 194, 335
- Pei, Y.C. 1992, *ApJ*, 395, 130
- Podsiadlowski, P., Ivanova, N., Justham, S., Rappaport, S. 2010, *MNRAS*, 406, 840
- Roman-Duval, J., Gordon, K. D., Meixner, M. et al., 2014 *ApJ*, 797, 86
- Sahai, R. & Nyman, Lars-Ake, 1997 *ApJ*, 487, L155
- Sahai, R., Zijlstra, A., Sánchez Contreras, C., & Morris, M., 2003 *ApJ*, 586, L81
- Sahai, R., Young, K., Patel, N. A., Sánchez Contreras, C. and Morris, M. 2006 *ApJ*, 653, 1241
- Sahai, R., Morris, M., Sánchez Contreras, C. and Claussen, M. 2007, *ApJ*, 134, 2200
- Sahai, R. 2009, *Astro2010: The Astronomy and Astrophysics Decadal Survey, Science White Papers, no. 256*
- Sahai, R., Claussen, M. J., Schnee, S. et al. 2011, *ApJ*, 739, L3
- Sahai, R., Vlemmings, W.H.T. & Nyman, L.A. 2017, *ApJ*, 841, 110
- Sahai, R. 2018, *Galaxies*, 6, 102
- Sánchez Contreras, C & Sahai, R. 2012, *ApJS*, 203, 16
- Sarkar, G. & Sahai, R. 2006, *ApJ*, 644, 1171
- Szczerba ,R. & Marten H. 1993, in Schwarz H.E., ed., *Second ESO/CTIO workshop, Mass loss on the AGB and beyond. ESO Conference and Workshop Proceedings No. 46*, Garching, p.90
- Soszyński et al. 2008, *Acta Astronomica*, 58, 293
- Ueta, T., Margaret, M., Matthew, B. 2000, *ApJ*, 528, 861
- van Aarle, E., Van Winckel, H., Lloyd Evans, T. et al. 2011, *A&A*, 530, A90
- van Aarle, E., Van Winckel, H., D. Smedt, K, Kamath, D., Wood, P.R. 2013, *A&A*, 554, 106
- van Loon, J.T., Groenewegen M. A. T., de Koter A., Trams N. R., Waters L. B. F. M., Zijlstra, A. A., Whitelock, P. A 1999, *A&A*, 351, 559

- Van Winckel, H., Waelkens, C., Fernie, J. D., Waters, L. B. F. M. 1999, A&A, 343, 202
- Van Winckel, H. 2003, ARA&A, 41, 391
- Waters, L. B. F. M., Waelkens, C., Mayor, M., Trams, N. R. 1993, A&A, 269
- Waters, L.B.F.M., Cami, J., de Jong, T., et al. 1998, Nature, 391, 868
- Willacy, K. 2004, ApJ, 600, L87
- Wong, A.-S., Yung, Y. L., & Friedson, A. J. 2003, Geophys. Res. Lett., 30, 30
- Zacharias, N., Monet, D. G., Levine, S. E., Urban, S. E., Gaume, R., Wycoff, G. L. 2004, AAS, 205, 4815
- Zaritsky, D., Harris, J., Thompson, I. B., Grebel, E. K. 2004, AJ, 128, 1606

Table 1. Photometric Data

Object	Type	U	B	V	R	I	J	H	K	[3.6]	[4.5]	[5.8]	[8.0]	[24] ^a	[24] ^b	W1	W2	W3	W4	W1'	W2'	W3'	W4'
post-RGB stars																							
J043919.30-685733.4	Shell	20.093	19.475	18.805	18.100	17.900	17.206	16.597	16.333	16.068	15.741	...	13.856	9.263	9.307	16.416	16.259	13.07 [†]	9.380 [†]	16.194	15.894	12.938	8.988 [†]
J051347.57-704450.5	Shell	19.909	18.510	17.077	16.740	15.683	14.661	13.933	13.719	13.661	13.728	13.625	13.563	9.257	9.310
...	15.76
...	16.29
J051920.18-722522.1	Shell	19.408	18.650	17.426	17.020	16.152	15.154	14.540	14.396	13.977	13.785	13.159	12.057	8.050	8.053	14.084	13.807	10.882	8.462	14.069	13.789	10.752	8.297
J053930.60-702248.5	Shell	...	19.934	18.243	18.600	16.915	15.810	14.981	14.756	14.611	14.686	14.405	14.160	9.568	9.345	14.907	15.130	11.350	9.302	14.804	15.206	11.274	9.015
J045555.15-712112.3	disk	18.216	18.455	18.165	17.610	...	16.790	16.350	16.011	14.232	14.190	11.518	9.974	7.323	7.197	14.034	13.774	8.696	6.833	14.035	13.814	8.762	6.896
J045755.05-681649.2	disk	20.118	19.563	18.321	...	17.205	16.369	15.651	15.470	15.059	14.922	14.557	12.480	9.626	9.732	15.233	15.460	11.489	9.825 [†]	15.144	15.094	11.253	9.190 [†]
J050257.89-665306.3	disk	19.988	19.788	18.518	17.610	17.563	15.979	15.242	14.666	14.387	13.830	13.829	11.652	8.531	8.601	14.174	14.134	10.747	8.472	14.169	4.138	11.201	8.773
J055102.44-685639.1	disk	20.108	19.951	18.861	18.210	17.821	16.346	15.598	14.734	13.890	13.383	12.727	10.138	5.954	5.968	14.223	13.409	9.120	6.076	14.247	13.410	9.042	6.022
post-AGB stars																							
J050632.10-714229.8	Shell	14.801	14.717	14.298	13.950	13.780	13.408	13.254	13.168	12.989	12.827	11.441	9.192	5.107	5.129	13.077	12.960	7.979	5.160	13.072	12.959	7.957	5.147
J051848.84-700247.0	Shell	18.692	17.142	15.429	14.800	13.852	13.152	12.713	12.568	12.372	11.992	10.889	8.558	4.197	4.232
J051906.86-694153.9	Shell	...	16.800	15.470	...	14.473	13.652	13.048	12.900	12.765	12.827	12.761	12.786	8.347	8.234	12.529	12.656	10.844	7.499	12.515	12.747	13.366 [†]	9.628 [†]
J053250.69-713925.8	Shell	17.985	16.533	15.069	14.240	13.803	13.124	12.842	12.709	12.488	12.280	11.255	8.898	4.751	4.715	12.537	12.360	7.348	4.873	12.555	12.370	7.327	4.846
J045623.21-692749.0	disk	17.707	16.211	14.628	14.070	13.123	12.416	11.740	11.430	10.533	10.420	10.068	9.486	7.149	7.231	10.695	10.460	8.752	7.260	10.709	10.504	8.851	7.743
J051418.09-691234.9	disk	15.837	14.924	14.552	13.780	13.853	13.089	12.635	12.093	10.144	9.394	8.669	7.835	5.970	6.045	10.669	9.584	7.290	6.025	10.554	9.500	7.297	6.111
J055122.52-695351.4	disk	15.870	15.589	15.160	14.460	14.009	13.717	13.317	13.099	11.669	10.678	9.676	8.408	5.979	5.724	12.248	11.009	7.606	5.969	12.029	10.763	7.578	5.889
J052519.48-705410.0	disk	16.310	15.450	14.973	14.800	14.276	14.221	13.829	13.459	10.897	10.119	9.502	8.647	6.618	6.564	11.954	10.791	8.312	6.989	11.668	10.566	8.272	6.856

NOTE—

1) [3.6], [4.5], [5.8], [8.0] photometric values correspond to *Spitzer* IRAC band 1–4 observations.2) [24]^a, [24]^b: *Spitzer* MIPS band 1 observations corresponding to epoch 1 and 2 respectively (Meixner et al. 2006), retrieved from<https://isa.ipac.caltech.edu>.3) WISE magnitudes: W1 (3.4 μ m), W2 (4.6 μ m), W3 (12 μ m), W4 (22 μ m)4) ALLWISE magnitudes: W1' (3.4 μ m), W2' (4.6 μ m), W3' (12 μ m), W4' (22 μ m)5) [†]: Magnitudes are upper limits

Table 2. Models of post-RGB objects

$T_d(\text{in})^a$	$T_d(\text{out})^b$	Y^c	R_{in}^d	τ^e	a_{min}	a_{max}	F_{bol}	L	M_{gd}^f	Age ^g	dM/dt^h	χ^2
(K)	(K)		(10^{14} cm)		(μm)	(μm)	(W m^{-2})	(L_{\odot})	(M_{\odot})	(yr)	($M_{\odot} \text{ yr}^{-1}$)	
J043919.30-685733.4 (shell source)												
Single shell (one-component) models with Sil-Ow grains												
550	161	8	1.82	1.5	0.005	0.25	1.8×10^{-15}	140.0	1.45×10^{-5}	8.09	1.79×10^{-6}	87.6
550	65.6	100	1.79	1.5	0.005	0.25	1.8×10^{-15}	140.0	1.74×10^{-4}	112	1.55×10^{-6}	61.4
550	38.4	500	1.79	1.5	0.005	0.25	1.8×10^{-15}	140.0	8.72×10^{-4}	565	1.54×10^{-6}	68.6
145	27.2	100	26.3	0.8	0.005	0.25	1.5×10^{-15}	116.0	2.01×10^{-2}	1650	1.22×10^{-5}	48.3
175	32	100	16	0.8	0.005	0.25	1.5×10^{-15}	116.0	7.51×10^{-3}	1010	7.45×10^{-6}	47.8
500	66.7	100	1.79	0.8	0.005	0.25	1.5×10^{-15}	116.0	9.32×10^{-5}	112	8.30×10^{-7}	43.6
Two-component model, # 1: cold outer shell: Sil-Ow and warm inner disk: Sil-Ow (disk fraction = 0.35)												18.8
130 “shell”	41.3	20	29.1	0.95	0.005	0.25	9.81×10^{-16}	76.0	5.87×10^{-3}	351	1.67×10^{-5}	
1000 “disk”	764	1.4	0.29	0.5	0.005	0.25	5.19×10^{-16}	40.0	2.19×10^{-8}	1.86	1.18×10^{-8}	
model # 1: varying the thickness of the warm inner disk												
1000	383	5.0	0.27	0.5	0.005	0.25	5.19×10^{-16}	40.0	6.67×10^{-8}	17.2	3.89×10^{-9}	34.4
1000	271	10	0.27	0.5	0.005	0.25	5.19×10^{-16}	40.0	1.31×10^{-7}	38.3	3.42×10^{-9}	39.4
Two-component model, # 2: cold outer shell: Sil-Ow and warm inner disk: Sil-Ow (disk fraction = 0.35)												25.8
130 “shell”	41.3	20	29.1	0.95	0.005	0.25	9.81×10^{-16}	76.0	5.87×10^{-3}	351	1.67×10^{-5}	
800 “disk”	644	1.4	0.14	0.25	1.0	25.0	5.19×10^{-16}	40.0	5.34×10^{-7}	0.89	5.99×10^{-7}	
model # 2: varying the thickness of the warm inner disk												
800	338	5.0	0.13	0.25	1.0	25.0	5.19×10^{-16}	40.0	1.66×10^{-6}	8.30	2.00×10^{-7}	40.9
800	240	10.0	0.13	0.25	1.0	25.0	5.19×10^{-16}	40.0	3.25×10^{-6}	18.5	1.76×10^{-7}	45.8
model # 2: varying the minimum and maximum grain sizes in the warm inner disk												
800	650	1.4	0.20	0.25	0.1	25.0	5.19×10^{-16}	40.0	2.45×10^{-7}	1.28	1.92×10^{-7}	37.9
800	647	1.4	0.15	0.25	1.0	5.0	5.19×10^{-16}	40.0	3.32×10^{-8}	0.95	3.49×10^{-8}	24.2
800	644	1.4	0.14	0.25	1.0	50.0	5.19×10^{-16}	40.0	7.12×10^{-7}	0.88	8.07×10^{-7}	26.0
† Correctly illuminated model # 1,c: two-component model assuming the shell to be divided into two parts												18.1
† 130 “shell(low-lat)”	42.8	20	27.7	0.65	0.005	0.25	9.81×10^{-16}	76.0	3.64×10^{-3}	334	1.09×10^{-5}	
† 130 “shell(high-lat)”	43.1	20	18.2	0.65	0.005	0.25	5.19×10^{-16}	40.0	1.56×10^{-3}	219	7.14×10^{-6}	
† 1000 “disk”	764	1.4	0.29	0.5	0.005	0.25	5.19×10^{-16}	40.0	2.19×10^{-8}	1.86	1.18×10^{-8}	
Correctly illuminated model # 2,c: two-component model assuming the shell to be divided into two parts												30.4
130 “shell(low-lat)”	43.1	20	27.3	0.60	0.005	0.25	9.81×10^{-16}	76.0	3.25×10^{-3}	329	9.90×10^{-6}	
130 “shell(high-lat)”	43.1	20	19.8	0.60	0.005	0.25	5.19×10^{-16}	40.0	1.71×10^{-3}	238	7.18×10^{-6}	
800 “disk”	644	1.4	0.14	0.25	1.0	25.0	5.19×10^{-16}	40.0	5.34×10^{-7}	0.89	5.99×10^{-7}	
J051347.57-704450.5 (shell source)												
Single shell (one-component) models with Sil-Ow grains												
250	155	3.0	14.1	0.35	0.1	0.25	1×10^{-14}	776.0	4.00×10^{-5}	17.8	2.24×10^{-6}	71.7
Varying the dust temperature at the shell’s inner radius												
200	127	3.0	23.8	0.35	0.1	0.25	1×10^{-14}	776.0	1.15×10^{-4}	30.2	3.79×10^{-6}	74.7
300	180	3.0	9.5	0.35	0.1	0.25	1×10^{-14}	776.0	1.82×10^{-5}	12	1.51×10^{-6}	74.2
Varying the shell’s optical depth												
250	155	3.0	14.0	0.30	0.1	0.25	1×10^{-14}	776.0	3.37×10^{-5}	17.7	1.91×10^{-6}	75.6
† 250	154	3.0	14.2	0.40	0.1	0.25	1×10^{-14}	776.0	4.66×10^{-5}	18	2.59×10^{-6}	69.2
Varying the shell’s grain sizes												
250	155	3.0	13.1	0.35	0.05	0.25	$1 \text{e-}14$	776.0	4.48×10^{-5}	16.6	2.7×10^{-6}	69.5
250	155	3.0	14.4	0.35	0.1	0.35	$1 \text{e-}14$	776.0	4.84×10^{-5}	18.2	2.66×10^{-6}	69.3
Varying the shell’s thickness												
250	181	2.0	14.3	0.35	0.1	0.25	1×10^{-14}	776.0	2.75×10^{-5}	9.06	3.04×10^{-6}	72.2

Table 2 continued on next page

Table 2 (continued)

$T_d(\text{in})^a$	$T_d(\text{out})^b$	Y^c	R_{in}^d	τ^e	a_{min}	a_{max}	F_{bol}	L	M_{gd}^f	Age g	dM/dt^h	χ^2
(K)	(K)		(10^{14}cm)		(μm)	(μm)	(W m^{-2})	(L_{\odot})	(M_{\odot})	(yr)	($M_{\odot} \text{ yr}^{-1}$)	
250	99.9	10.0	13.9	0.35	0.1	0.25	1×10^{-14}	776.0	1.3×10^{-4}	79.2	1.64×10^{-6}	71.7
J051920.18-722522.1 (shell source)												
Single shell (one-component) model with Sil-Ow grains, # 1,s												
200	63.5	20	18.4	0.75	0.005	0.25	7.5×10^{-15}	582.0	1.85×10^{-3}	221	8.34×10^{-6}	89.1
Varying the dust temperature at the shell's inner radius												
150	49.7	20	38.4	0.75	0.005	0.25	7.5×10^{-15}	582.0	8.04×10^{-3}	462	1.74×10^{-5}	103.2
250	75.8	20	10.9	0.75	0.005	0.25	7.5×10^{-15}	582.0	6.47×10^{-4}	131	4.94×10^{-6}	88.1
Varying the shell's optical depth												
200	64.0	20	18.2	0.65	0.005	0.25	7.5×10^{-15}	582.0	1.56×10^{-3}	219	7.14×10^{-6}	93.5
200	63.0	20	18.6	0.85	0.005	0.25	7.5×10^{-15}	582.0	2.14×10^{-3}	224	9.55×10^{-6}	90.6
Varying the shell's grain sizes												
200	63.6	20	20.4	0.75	0.05	0.25	7.5×10^{-15}	582.0	1.55×10^{-3}	246	6.3×10^{-6}	94.6
200	63.4	20	19.8	0.75	0.005	0.5	7.5×10^{-15}	582.0	2.29×10^{-3}	238	9.6×10^{-6}	91.9
Varying the shell's thickness												
200	102	5	18.6	0.75	0.005	0.25	7.5×10^{-15}	582.0	4.75×10^{-4}	47.3	1.00×10^{-5}	88.2
200	50.4	40	18.3	0.75	0.005	0.25	7.5×10^{-15}	582.0	3.67×10^{-3}	453	8.10×10^{-6}	89.5
Two-component model, # 2: cold outer shell: Sil-Ow and warm inner disk: Sil-Ow (disk fraction = 0.4)												
110 "shell"	36.8	20	70.6	1.00	0.005	0.25	4.5×10^{-15}	349.0	3.63×10^{-2}	851	4.27×10^{-5}	17.3
500	326	2.0	1.00	0.40	0.5	20.0	3×10^{-15}	233.0	3.01×10^{-5}	15.9	1.89×10^{-6}	
Varying the minimum and maximum grain sizes in the warm inner disk												
500	329	2.0	1.15	0.40	0.1	20.0	3×10^{-15}	233.0	1.39×10^{-5}	18.2	7.62×10^{-7}	53.2
500	326	2.0	1.11	0.40	0.5	5.0	3×10^{-15}	233.0	2.71×10^{-6}	17.6	1.54×10^{-7}	21.1
† Correctly illuminated model # 2,c: two-component model assuming the shell to be divided into two parts												
†110 "shell(low-lat)"	37.9	20	65.8	0.65	0.005	0.25	4.5×10^{-15}	349.0	2.05×10^{-2}	792	2.58×10^{-5}	
†110 "shell(high-lat)"	37.9	20	53.6	0.65	0.005	0.25	3×10^{-15}	233.0	1.36×10^{-2}	645	2.11×10^{-5}	
†500 "disk"	326	2.0	1.00	0.40	0.5	20.0	3×10^{-15}	233.0	3.01×10^{-5}	15.9	1.89×10^{-6}	
Shell thickness increased by a factor of 10 in model # 2,c												
110 "shell(high-lat)"	17.6	200	65.6	0.65	0.005	0.25	4.5×10^{-15}	349.0	0.204	8270	2.46×10^{-5}	16.9
110 "shell(high-lat)"	17.6	200	53.4	0.65	0.005	0.25	3×10^{-15}	233.0	0.135	6740	2.01×10^{-5}	
500 "disk"	326	2.0	1.00	0.40	0.5	20.0	3×10^{-15}	233.0	3.01×10^{-5}	15.9	1.89×10^{-6}	
J053930.60-702248.5 (shell source)												
† Single shell (one-component) model with Sil-Ow grains												
†300	112	10	4.77	0.70	0.005	0.25	3.8×10^{-15}	295	5.81×10^{-5}	27.2	2.13×10^{-6}	30.4
Varying the dust temperature at the shell's inner radius												
250	97.5	10	7.08	0.70	0.005	0.25	3.8×10^{-15}	295	1.28×10^{-4}	40.4	3.16×10^{-6}	30.8
350	125	10	3.52	0.70	0.005	0.25	3.8×10^{-15}	295	3.16×10^{-5}	20.1	1.57×10^{-6}	32.0
Varying the shell's optical depth												
300	113	10	4.72	0.60	0.005	0.25	3.8×10^{-15}	295	4.88×10^{-5}	27.0	1.81×10^{-6}	32.7
300	111	10	4.83	0.80	0.005	0.25	3.8×10^{-15}	295	6.79×10^{-5}	27.5	2.47×10^{-6}	29.2
Varying the shell's grain sizes												
300	112	10	5.27	0.7	0.05	0.25	3.8×10^{-15}	295	4.83×10^{-5}	30.1	1.60×10^{-6}	32.9
300	112	10	5.26	0.7	0.005	0.50	3.8×10^{-15}	295	7.53×10^{-5}	30.0	2.51×10^{-6}	27.8
Varying the shell's thickness												
300	145	5	4.83	0.70	0.005	0.25	3.8×10^{-15}	295	2.97×10^{-5}	12.2	2.43×10^{-6}	30.7
300	87.8	20	4.76	0.70	0.005	0.25	3.8×10^{-15}	295	1.15×10^{-4}	57.3	2.01×10^{-6}	30.4

Table 2 continued on next page

Table 2 (continued)

$T_d(\text{in})^a$	$T_d(\text{out})^b$	Y^c	R_{in}^d	τ^e	a_{min}	a_{max}	F_{bol}	L	M_{gd}^f	Age g	dM/dt^h	χ^2
(K)	(K)		(10^{14} cm)		(μm)	(μm)	(W m^{-2})	(L_\odot)	(M_\odot)	(yr)	($M_\odot \text{ yr}^{-1}$)	
J045555.15-712112.3 (disk source)												
Single shell (one-component) model with Sil-Ow grains, # 1,s:												
550	101	20	4.49	2.3	0.005	1.0	8×10^{-15}	621.0	4.49×10^{-4}	54.0	8.32×10^{-6}	619.8
Varying the dust temperature at the shell's inner radius												
500	95.3	20	5.33	2.3	0.005	1.0	8×10^{-15}	621.0	6.35×10^{-4}	64.2	9.89×10^{-6}	423.8
600	108	20	3.79	2.3	0.005	1.0	8×10^{-15}	621.0	3.20×10^{-4}	45.6	7.02×10^{-6}	1033.9
Varying the shell's optical depth												
550	105	20	4.41	2.0	0.005	1.0	8×10^{-15}	621.0	3.78×10^{-4}	53.1	7.11×10^{-6}	463.8
550	99.6	20	4.51	2.5	0.005	1.0	8×10^{-15}	621.0	4.94×10^{-4}	54.3	9.09×10^{-6}	727.4
Varying the shell's grain sizes												
550	93.3	20	5.83	2.3	0.005	0.25	8×10^{-15}	621.0	5.70×10^{-4}	70.2	8.11×10^{-6}	341.0
550	105	20	3.64	2.3	0.005	2.0	8×10^{-15}	621.0	3.93×10^{-4}	43.8	8.97×10^{-6}	1132.3
550	105	20	4.36	2.3	0.05	1.0	8×10^{-15}	621.0	3.67×10^{-4}	52.5	6.98×10^{-6}	554.4
Varying the shell's thickness												
550	168	5	4.56	2.3	0.005	1.0	8×10^{-15}	621.0	1.16×10^{-4}	11.6	1.00×10^{-5}	802.8
550	130	10	4.51	2.3	0.005	1.0	8×10^{-15}	621.0	2.27×10^{-4}	25.7	8.83×10^{-6}	676.7
550	88.1	30	4.46	2.3	0.005	1.0	8×10^{-15}	621.0	6.67×10^{-4}	82.0	8.13×10^{-6}	600.8
Two-component model, # 2: cold outer shell: Sil-Ow and warm inner disk: Sil-Ow (disk fraction = 0.1)												1139.4
550 "shell"	101	20	4.26	2.3	0.005	1.0	7.2×10^{-15}	559.0	4.04×10^{-4}	51.3	7.89×10^{-6}	
1200 "disk"	241	10	0.363	0.5	0.005	0.1	8×10^{-16}	62.0	7.19×10^{-7}	51.8	1.39×10^{-8}	
Correctly illuminated model # 2,c: two-component model assuming the shell to be divided into two parts												1125.5
550 "shell(low-lat)"	104	20	4.11	2.10	0.005	1.0	7.2×10^{-15}	559.0	3.45×10^{-4}	49.6	6.96×10^{-6}	
550 "shell(high-lat)"	113	20	1.06	2.10	0.005	1.0	8×10^{-16}	62.0	2.30×10^{-5}	12.8	1.80×10^{-6}	
1200 "disk"	241	10	0.363	0.5	0.005	0.1	8×10^{-16}	62.0	7.19×10^{-7}	51.8	1.39×10^{-8}	
Two-component model, # 3: cold outer shell: Sil-Ow/0.8 + grf-DL/0.2 and warm inner disk: grf-DL (disk fraction = 0.1)												1276.7
500 "shell"	216	2	7.64	1.8	0.005	0.25	7.2×10^{-15}	559	9.6×10^{-5}	4.84	1.98×10^{-5}	
800 "disk"	356	5	1.06	0.7	0.005	0.25	8×10^{-16}	62	2.67×10^{-6}	66.9	3.99×10^{-8}	
Correctly illuminated model # 3,c: two-component model assuming the shell to be divided into two parts												1318.3
500 "shell(low-lat)"	224	2	7.42	1.60	0.005	0.25	7.2×10^{-15}	559.0	8.06×10^{-5}	4.71	1.71×10^{-5}	
500 "shell(high-lat)"	236	2	2.14	1.60	0.005	0.25	8×10^{-16}	62.0	6.71×10^{-6}	1.36	4.94×10^{-6}	
800 "disk"	356	5	1.06	0.7	0.005	0.25	8×10^{-16}	62	2.67×10^{-6}	66.9	3.99×10^{-8}	
† Two-component model, # 4: cold outer shell: Sil-Ow and warm inner disk: Sil-Ow (disk fraction = 0.4)												116.6
†300 "shell"	138	2	12.5	2.5	0.005	0.25	3.6×10^{-15}	279.0	2.84×10^{-4}	7.92	3.59×10^{-5}	
†1000 "disk"	226	10	0.919	1.0	0.005	0.25	2.4×10^{-15}	186.0	3.08×10^{-6}	131	2.35×10^{-8}	
J045755.05-681649.2 (disk source)												
Single shell (one-component) model with Sil-Ow grains, # 1,s:												
500	118	20	1.94	1.0	0.005	0.25	2.8×10^{-15}	217.0	2.75×10^{-5}	23.4	1.18×10^{-6}	25.2
Varying the dust temperature at the shell's inner radius												
450	110	20	2.34	1.0	0.005	0.25	2.8×10^{-15}	217.0	4.00×10^{-5}	28.2	1.42×10^{-6}	31.1
550	125	20	1.65	1.0	0.005	0.25	2.8×10^{-15}	217.0	1.98×10^{-5}	19.9	9.98×10^{-7}	20.70
Varying the shell's optical depth												
500	119	20	1.93	0.9	0.005	0.25	2.8×10^{-15}	217.0	2.44×10^{-5}	23.2	1.05×10^{-6}	25.1
500	117	20	1.97	1.1	0.005	0.25	2.8×10^{-15}	217.0	3.12×10^{-5}	23.8	1.31×10^{-6}	26.9
Varying the shell's thickness												
500	200	5	1.99	1.0	0.005	0.25	2.8×10^{-15}	217.0	7.20×10^{-6}	5.04	1.43×10^{-6}	26.7
500	85.5	50	1.94	1.0	0.005	0.25	2.8×10^{-15}	217.0	6.89×10^{-5}	60.4	1.14×10^{-6}	25.1

Table 2 continued on next page

Table 2 (continued)

$T_d(\text{in})^a$	$T_d(\text{out})^b$	Y^c	R_{in}^d	τ^e	a_{min}	a_{max}	F_{bol}	L	M_{gd}^f	Age ^g	dM/dt^h	χ^2
(K)	(K)		(10^{14} cm)		(μm)	(μm)	(W m^{-2})	(L_{\odot})	(M_{\odot})	(yr)	($M_{\odot} \text{ yr}^{-1}$)	
Two-component model, # 2: cold outer shell: Sil-Ow and warm inner disk: Sil-Ow (disk fraction = 0.4)												18.1
400 “shell”	91.0	30	2.31	0.9	0.1	1.0	1.68×10^{-15}	130.0	5.84×10^{-5}	42.6	1.37×10^{-6}	
1300 “disk”	921	2	0.12	0.5	0.005	2.0	1.12×10^{-15}	87.0	9.64×10^{-9}	1.94	4.98×10^{-9}	
† Correctly illuminated model # 2,c: two-component model assuming the shell to be divided into two parts												24.7
†400 “shell(low-lat)”	93.3	30	2.20	0.6	0.1	1.0	1.68×10^{-15}	130.0	3.52×10^{-5}	40.5	8.7×10^{-7}	
†400 “shell(high-lat)”	93.5	30	1.74	0.6	0.1	1.0	1.12×10^{-15}	87.0	2.21×10^{-5}	32.1	6.9×10^{-7}	
†1300 “disk”	921	2	0.12	0.5	0.005	2.0	1.12×10^{-15}	87.0	9.64×10^{-9}	1.94	4.98×10^{-9}	
Shell thickness increased by a factor of 10 in model # 2,c												23.9
400 “shell(low-lat)”	43.0	300	2.19	0.6	0.1	1.0	1.68×10^{-15}	130.0	3.48×10^{-4}	415	8.40×10^{-7}	
400 “shell(high-lat)”	43.1	300	1.74	0.6	0.1	1.0	1.12×10^{-15}	87.0	2.21×10^{-4}	331	6.69×10^{-7}	
1300 “disk”	921	2	0.12	0.5	0.005	2.0	1.12×10^{-15}	87.0	9.64×10^{-9}	1.94	4.98×10^{-9}	
J050257.89-665306.3												
(disk source)												
Single shell (one-component) model with Sil-Ow grains, # 1,s:												
250	64.9	30	8.14	1.1	0.005	0.25	4.2×10^{-15}	326.0	7.97×10^{-4}	150	5.32×10^{-6}	114.3
Two-component model, # 2: cold outer shell: Sil-Ow and warm inner disk: Sil-Ow (disk fraction = 0.4)												46.4
240 “shell”	90.2	10	7.23	1.20	0.005	1.0	2.34×10^{-15}	182.0	3.05×10^{-4}	41.3	7.38×10^{-6}	
1200 “disk”	677	3.0	0.136	0.5	0.3	5.0	1.56×10^{-15}	121.0	5.77×10^{-8}	4.32	1.34×10^{-8}	
† Correctly illuminated model # 2,c: two-component model assuming the shell to be divided into two parts												48.4
†240 “shell(low-lat)”	94.5	10	6.57	0.65	0.005	1.0	2.34×10^{-15}	182.0	1.36×10^{-4}	37.5	3.63×10^{-6}	
†240 “shell(high-lat)”	94.6	10	5.28	0.65	0.005	1.0	1.56×10^{-15}	121.0	8.8×10^{-5}	30.1	2.92×10^{-6}	
†1200 “disk”	677	3.0	0.136	0.5	0.3	5.0	1.56×10^{-15}	121.0	5.77×10^{-8}	4.32	1.34×10^{-8}	
Two-component model, # 3: cold outer shell: Sil-Ow and warm inner disk: amC-Hn (disk fraction = 0.3)												39.3
250 “shell”	90.8	10	6.76	1.70	0.005	0.25	2.59×10^{-15}	201.0	2.83×10^{-4}	38.6	7.34×10^{-6}	
1000 “disk”	726	2.0	0.242	0.6	0.005	0.50	1.11×10^{-15}	86.0	2.21×10^{-8}	3.84	5.75×10^{-9}	
Correctly illuminated model # 3,c: two-component model assuming the shell to be divided into two parts												43.9
250 “shell(low-lat)”	93.2	10	6.35	1.3	0.005	0.25	2.59×10^{-15}	201.0	1.91×10^{-4}	36.2	5.27×10^{-6}	
250 “shell(high-lat)”	93.9	10	3.86	1.3	0.005	0.25	1.11×10^{-15}	86.0	7.05×10^{-5}	22.0	3.2×10^{-6}	
1000 “disk”	726	2.0	0.242	0.6	0.005	0.50	1.11×10^{-15}	86.0	2.21×10^{-8}	3.84	5.75×10^{-9}	
J055102.44-685639.1 (disk source)												
Single shell (one-component) model with Sil-Ow grains, # 1,s:												
190	44.0	20	37.5	4.0	0.005	0.25	7×10^{-15}	543	4.1×10^{-2}	452	9.08×10^{-5}	600.2
Two-component model, # 2a: cold outer shell: Sil-Ow and warm inner disk: Sil-Ow (disk fraction = 0.4)												1800.0
350 “shell”	1.28	3	7.06	8.0	0.005	0.07	5.4×10^{-15}	419	2.12×10^{-3}	8.95	2.37×10^{-4}	
1400 “disk”	872	2.0	0.361	0.5	0.005	0.12	3.6×10^{-15}	279.0	1.05×10^{-7}	5.72	1.84×10^{-8}	
Two-component model, # 2b: cold outer shell: Sil-Ow and warm inner disk: Sil-Ow (disk fraction = 0.3)												639.7
350 “shell”	128	3	7.20	8.00	0.005	0.07	5.6×10^{-15}	435.0	2.2×10^{-3}	9.12	2.41×10^{-4}	
1400 “disk”	748	2.0	0.278	1.00	0.005	0.08	2.4×10^{-15}	186.0	2.34×10^{-7}	4.41	5.3×10^{-8}	
† Two-component model, # 3: cold outer shell: Sil-Ow/0.4 + SiC-Pg/0.6 and warm inner disk: amC-Hn (disk fraction = 0.3)												147.3
†350 “shell”	118	3	9.89	12.0	0.005	0.07	5.6×10^{-15}	435.0	3.05×10^{-3}	12.5	2.43×10^{-4}	
†2000 “disk”	813	7.0	0.09	1.0	0.005	0.05	2.4×10^{-15}	186.0	1.99×10^{-8}	8.79	2.27×10^{-9}	
model # 3: varying the dust temperature at the inner radius of the cold outer shell												
250	87.8	3	20.0	12.0	0.005	0.07	5.6×10^{-15}	435	1.25×10^{-2}	25.3	4.92×10^{-4}	458.2
450	143	3	6.11	12.0	0.005	0.07	5.6×10^{-15}	435	1.17×10^{-3}	7.75	1.5×10^{-4}	476.4
model # 3: varying the thickness of the cold outer shell												
350	138	2	10.0	12.0	0.005	0.07	5.6×10^{-15}	435.0	2.09×10^{-3}	6.35	3.29×10^{-4}	151.9
350	75.6	10	9.72	12.0	0.005	0.07	5.6×10^{-15}	435.0	9.83×10^{-3}	55.5	1.77×10^{-4}	154.5

Table 2 continued on next page

Table 2 (continued)

$T_d(\text{in})^a$	$T_d(\text{out})^b$	Y^c	R_{in}^d	τ^e	a_{min}	a_{max}	F_{bol}	L	M_{gd}^f	Age ^g	dM/dt^h	χ^2
(K)	(K)		(10^{14} cm)		(μm)	(μm)	(W m^{-2})	(L_{\odot})	(M_{\odot})	(yr)	($M_{\odot} \text{ yr}^{-1}$)	
model # 3: varying the optical depth of the cold outer shell												
350	122	3	9.74	9.00	0.005	0.07	5.6×10^{-15}	435.0	2.22×10^{-3}	12.4	1.8×10^{-4}	357.9
350	114	3	9.8	18.0	0.005	0.07	5.6×10^{-15}	435.0	4.5×10^{-3}	12.4	3.62×10^{-4}	189.7
model # 3: varying the maximum grain size in the cold outer shell												
350	118	3	9.05	12.0	0.005	0.05	5.6×10^{-15}	435.0	3.97×10^{-3}	11.5	3.46×10^{-4}	152.5
350	119	3	10.8	12.0	0.005	0.09	5.6×10^{-15}	435.0	2.14×10^{-3}	13.7	1.56×10^{-4}	622.3
model # 3: varying the dust temperature at the disk's inner radius												
1800	726	7.0	0.12	1.0	0.005	0.05	2.4×10^{-15}	186.0	3.47×10^{-8}	11.6	2.99×10^{-9}	180.1
2200	899	7.0	0.07	1.0	0.005	0.05	2.4×10^{-15}	186.0	1.21×10^{-8}	6.85	1.77×10^{-9}	159.2
model # 3: varying the disks' thickness												
2000	1120	3.0	0.09	1.00	0.005	0.05	2.4×10^{-15}	186.0	8.8×10^{-9}	2.97	2.96×10^{-9}	159.8
2000	542	20.0	0.09	1.00	0.005	0.05	2.4×10^{-15}	186.0	5.63×10^{-8}	27.7	2.03×10^{-9}	148.1
model # 3: varying the disks' optical depth												
2000	837	7.0	0.09	0.8	0.005	0.05	2.4×10^{-15}	186	1.55×10^{-8}	8.68	1.79×10^{-9}	202.5
2000	791	7.0	0.09	1.2	0.005	0.05	2.4×10^{-15}	186	2.44×10^{-8}	8.88	2.75×10^{-9}	151.3
model # 3: varying the disks' maximum grain size												
2000	832	7.0	0.09	1.0	0.005	0.10	2.4×10^{-15}	186	1.62×10^{-8}	8.83	1.83×10^{-9}	169.6
2000	838	7.0	0.07	1.0	0.005	0.50	2.4×10^{-15}	186	1.17×10^{-8}	6.93	1.68×10^{-9}	263.9

NOTE—

The inner disk is approximated as an axially symmetric wedge-shaped fraction of a sphere. This fraction is referred to as “**disk fraction**” The acronyms for the dust grain compositions refer to ‘warm’ and ‘cold’ silicates (Sil-Ow and Sil-Oc) from Ossenkopf et al. (1992), graphite grains (grf-DL) from Draine & Lee (1984), amorphous carbon (amC-Hn) from Hanner (1988) and silicon carbide (SiC-Pg) from Pégourié (1988).

shell: Parameters for the outer shell in two-component models

disk: Parameters for the inner disk in two-component models

shell(low-lat): Correctly illuminated models, part of shell in the solid angle not covered by the disk

shell(high-lat): Correctly illuminated models, part of shell in the solid angle covered by the disk

suffix ‘s’: Single shell model

suffix ‘c’: Correctly illuminated two-component model

[†]: Adopted (best-fit) model

^aThe (input) dust temperature at shell inner radius

^bThe (output) dust temperature at shell outer radius

^cThe (input) ratio of the dust shell’s outer to inner radius

^dThe (inferred) inner radius of the dust shell

^eThe (input) dust shell’s optical depth at $0.55 \mu\text{m}$

^fThe (inferred) circumstellar (gas+dust) mass using $\delta = 200$

^gThe (inferred) dust shell’s age

^hThe (inferred) mass-loss rate characterizing the dust shell

Table 3. Models of post-AGB objects

$T_d(\text{in})^a$	$T_d(\text{out})^b$	Y^c	R_{in}^d	τ^e	a_{min}	a_{max}	F_{bol}	L	M_{gd}^f	Age^g	dM/dt^h	χ^2
(K)	(K)		(10^{14}cm)		(μm)	(μm)	(W m^{-2})	(L_{\odot})	(M_{\odot})	(yr)	($M_{\odot} \text{ yr}^{-1}$)	
J050632.10-714229.8 (shell source)												
Single shell (one-component) model with Sil-Ow grains, # 1,s												
200	62.4	20	81.1	0.60	0.005	0.25	7×10^{-14}	5434	2.87×10^{-2}	3260	8.83×10^{-6}	231.1
Varying the dust temperature at the shell's inner radius												
180	57.1	20	106.0	0.60	0.005	0.25	7×10^{-14}	5434	4.93×10^{-2}	4260	1.16×10^{-5}	248.7
220	67.4	20	64.7	0.60	0.005	0.25	7×10^{-14}	5434	1.83×10^{-2}	2600	7.05×10^{-6}	253.9
Nested Shell Models: The warm inner shell												
grain type # 1: Sil-Ow; varying the temperature at the inner radius of the warm shell												
450	286	2	15.4	0.4	0.005	0.25	7×10^{-14}	5434	6.92×10^{-5}	9.77	7.08×10^{-6}	1690.1
400	260	2	18.9	0.4	0.005	0.25	7×10^{-14}	5434	1.05×10^{-4}	12.0	8.71×10^{-6}	1528.2
350	233	2	24.3	0.4	0.005	0.25	7×10^{-14}	5434	1.72×10^{-4}	15.4	1.12×10^{-5}	1382.4
grain type # 1: Sil-Ow; varying the maximum grain size in the inner shell for $T_d(\text{in}) = 400 \text{ K}$												
400	263	2	16.9	0.4	0.005	1.0	7×10^{-14}	5434	1.11×10^{-4}	10.7	1.03×10^{-5}	1528.2
400	265	2	11.6	0.4	0.005	5.0	7×10^{-14}	5434	1.12×10^{-4}	7.34	1.53×10^{-5}	1545.0
grain type: Sil-Oc												
400	261	2	16.4	0.4	0.005	0.25	7×10^{-14}	5434	6.72×10^{-5}	10.4	6.45×10^{-6}	1579.5
grain type # 2: amC-Hn:0.1, Sil-Ow:0.9												
350	239	2	26.5	0.4	0.1	0.5	7×10^{-14}	5434	1.59×10^{-4}	16.8	9.48×10^{-6}	1412.0
grain type: amC-Hn:0.2, Sil-Ow:0.8												
350	241	2	27.3	0.4	0.1	0.5	7×10^{-14}	5434	1.73×10^{-4}	17.3	1.00×10^{-5}	1445.6
grain type # 3: grf-DL:0.3, Sil-Ow:0.7												
$\dagger 350$	163	5	23.7	0.4	0.1	1.0	7×10^{-14}	5434	7.5×10^{-4}	60.0	1.25×10^{-5}	988.4
Nested shells # 1: correctly illuminated Sil-Ow outer shell with Sil-Ow (grain type # 1) inner shell, $T_d(\text{in}) = 400 \text{ K}$												
100	73.9	2	484	0.45	0.005	0.25	7×10^{-14}	5434	7.69×10^{-2}	1020	7.51×10^{-5}	181.6
Nested shells # 2: correctly illuminated Sil-Ow outer shell with amC-Hn/0.1 + Sil-Ow/0.9 (grain type # 2) inner shell, $T_d(\text{in}) = 350 \text{ K}$												
100	74.3	2	488	0.40	0.005	0.25	7×10^{-14}	5434	6.94×10^{-2}	1030	6.73×10^{-5}	164.2
\dagger Nested shells # 3: correctly illuminated Sil-Ow outer shell with grf-DL/0.3 + Sil-Ow/0.7 (grain type # 3) inner shell, $T_d(\text{in}) = 350 \text{ K}$												
$\dagger 100$	74.8	2	481	0.35	0.005	0.25	7×10^{-14}	5434	5.91×10^{-2}	1020	5.81×10^{-5}	154.7
J051848.84-700247.0 (shell source)												
\dagger Single shell (one-component) model with Sil-Ow grains												
$\dagger 350$	77.4	20	27.5	3.2	0.005	0.25	8×10^{-14}	6210.0	1.76×10^{-2}	1100	1.6×10^{-5}	50.4
Varying the dust temperature at the shell's inner radius												
300	69.6	20	37.4	3.2	0.005	0.25	8×10^{-14}	6210.0	3.25×10^{-2}	1500	2.17×10^{-5}	235.7
400	84.4	20	21.5	3.2	0.005	0.25	8×10^{-14}	6210.0	1.08×10^{-2}	864	1.25×10^{-5}	297.4
Varying the shell's optical depth												
350	80.9	20	26.7	2.5	0.005	0.25	8×10^{-14}	6210.0	1.3×10^{-2}	1070	1.21×10^{-5}	470.8
350	74.6	20	28.3	4.0	0.005	0.25	8×10^{-14}	6210.0	2.33×10^{-2}	1140	2.05×10^{-5}	103.0
Varying the shell's thickness												
350	126	5	28.1	3.2	0.005	0.25	8×10^{-14}	6210.0	4.59×10^{-3}	237	1.93×10^{-5}	98.4
J051906.86-694153.9 (shell source)												
Nested Shell Models: The warm inner shell: amC-Hn grain-type												
$\dagger 2000$	1480	2	0.231	0.35	0.005	0.25	2.6×10^{-14}	2018.0	9.58×10^{-9}	0.146	6.54×10^{-8}	179.3
Varying the dust temperature at the warm shell's inner radius												
1700	1260	2	0.355	0.35	0.005	0.25	2.6×10^{-14}	2018.0	2.27×10^{-8}	0.225	1.01×10^{-7}	225.1

Table 3 continued on next page

Table 3 (continued)

$T_d(\text{in})^a$	$T_d(\text{out})^b$	Y^c	R_{in}^d	τ^e	a_{min}	a_{max}	F_{bol}	L	M_{gd}^f	Age^g	dM/dt^h	χ^2
(K)	(K)		(10^{14} cm)		(μm)	(μm)	(W m^{-2})	(L_{\odot})	(M_{\odot})	(yr)	($M_{\odot} \text{ yr}^{-1}$)	
2300	1700	2	0.160	0.35	0.005	0.25	2.6×10^{-14}	2018.0	4.62×10^{-9}	0.102	4.54×10^{-8}	189.0
Varying the optical depth of the warm inner shell												
2000	1510	2	0.224	0.20	0.005	0.25	2.6×10^{-14}	2018.0	5.16×10^{-9}	0.142	3.63×10^{-8}	216.4
2000	1460	2	0.237	0.50	0.005	0.25	2.6×10^{-14}	2018.0	1.44×10^{-8}	0.150	9.58×10^{-8}	203.5
Varying the thickness of the warm inner shell												
2000	945	7	0.225	0.35	0.005	0.25	2.6×10^{-14}	2018.0	3.18×10^{-8}	0.856	3.72×10^{-8}	219.2
†Nested shells: correctly illuminated SiC-Pg outer shell with amC-Hn warm inner shell												
†160	125	2	24.3	0.07	2.3	3.0	2.6×10^{-14}	2018.0	1.78×10^{-4}	51.4	3.46×10^{-6}	21.3
Nested shells: varying temperature at the inner boundary of the cold outer shell												
130	104	2.0	43.9	0.07	2.3	3.0	2.6×10^{-14}	2018.0	5.8×10^{-4}	92.8	6.25×10^{-6}	55.4
200	152	2.0	13.8	0.07	2.3	3.0	2.6×10^{-14}	2018.0	5.72×10^{-5}	29.1	1.96×10^{-6}	30.5
Nested shells: varying optical depth of the cold outer shell												
160	125	2.0	24.0	0.05	2.3	3.0	2.6×10^{-14}	2018.0	1.24×10^{-4}	50.8	2.44×10^{-6}	26.5
160	125	2.0	24.8	0.1	2.3	3.0	2.6×10^{-14}	2018.0	2.63×10^{-4}	52.3	5.03×10^{-6}	80.6
Nested shells: varying the minimum and maximum grain sizes in the cold outer shell												
160	127	2.0	35.7	0.07	1.0	3.0	2.6×10^{-14}	2018.0	2.23×10^{-4}	75.4	2.96×10^{-6}	86.0
160	122	2.0	21.5	0.07	2.3	5.0	2.6×10^{-14}	2018.0	2.30×10^{-4}	45.5	5.07×10^{-6}	118.5
Nested shells: varying the thickness of the cold outer shell												
160	78.7	10.0	23.9	0.07	2.3	3.0	2.6×10^{-14}	2018.0	8.62×10^{-4}	455	1.89×10^{-6}	35.5
J053250.69-713925.8 (shell source)												
Single shell (one-component) model with Sil-Ow/0.2 and grf-DL/0.8 grains												
†260	160	2	68.1	0.90	0.005	0.50	6×10^{-14}	4657.0	6.45×10^{-3}	144	4.48×10^{-5}	214.4
Varying the dust temperature at the shell's inner radius												
250	154	2	73.7	0.90	0.005	0.50	6×10^{-14}	4657.0	7.55×10^{-3}	156	4.85×10^{-5}	777.0
270	166	2	62.9	0.90	0.005	0.50	6×10^{-14}	4657.0	5.50×10^{-3}	133	4.14×10^{-5}	460.2
Varying the shell's optical depth												
260	163	2	67.5	0.80	0.005	0.50	6×10^{-14}	4657.0	5.63×10^{-3}	143	3.94×10^{-5}	2220.7
260	158	2	68.9	1.00	0.005	0.50	6×10^{-14}	4657.0	7.34×10^{-3}	146	5.04×10^{-5}	2547.2
Varying the maximum grain sizes in the shell												
260	158	2	76.4	0.90	0.005	0.25	6×10^{-14}	4657.0	6.76×10^{-3}	162	4.18×10^{-5}	241.4
260	163	2	56.8	0.90	0.005	1.0	6×10^{-14}	4657.0	6.04×10^{-3}	120	5.03×10^{-5}	253.7
Varying the shell thickness												
260	107	5	66.1	0.90	0.005	0.50	6×10^{-14}	4657.0	1.52×10^{-2}	558	2.71×10^{-5}	426.7
J045623.21-692749.0 (disk source)												
Single shell (one-component) model with Sil-Ow grains												
1100	163	50	1.29	0.6	0.005	5.0	8.5×10^{-14}	6598	5.23×10^{-5}	1340	3.91×10^{-7}	254.2
Nested Shell Models: The warm inner shell (model # 1) : Sil-Ow grain type												
†1100	619	3	1.34	0.6	0.005	5.0	8.5×10^{-14}	6598.0	3.38×10^{-6}	1.7	1.99×10^{-6}	191.3
†Nested shells model # 1: correctly illuminated Sil-Ow cold outer shell and Sil-Ow warm inner shell												
†150	115	2	106	0.1	0.005	0.25	8.5×10^{-14}	6598.0	8.25×10^{-4}	225	3.67×10^{-6}	100.2
Two-component model, # 2: Sil-Ow cold outer shell and amC-Hn warm inner disk (disk fraction = 0.5)												
400 "shell"	123	15	9.36	0.22	0.40	1.0	4.25×10^{-14}	3300.0	2.7×10^{-4}	83.1	3.25×10^{-6}	
1100 "disk"	775	2	0.94	0.5	0.005	2.0	4.25×10^{-14}	3300.0	5.63×10^{-7}	14.9	3.77×10^{-8}	
Correctly illuminated model # 2,c: two-component model assuming the shell to be divided into two parts												
400 "shell(low-lat)"	125	15	8.85	0.12	0.40	1.0	4.25×10^{-14}	3300.0	1.32×10^{-4}	78.5	1.68×10^{-6}	
400 "shell(high-lat)"	125	15	8.67	0.12	0.40	1.0	4.25×10^{-14}	3300.0	1.27×10^{-4}	77.0	1.64×10^{-6}	
1100 "disk"	775	2	0.94	0.5	0.005	2.0	4.25×10^{-14}	3300.0	5.63×10^{-7}	14.9	3.77×10^{-8}	

Table 3 continued on next page

Table 3 (continued)

$T_d(\text{in})^a$	$T_d(\text{out})^b$	Y^c	R_{in}^d	τ^e	a_{min}	a_{max}	F_{bol}	L	M_{gd}^f	Age ^g	dM/dt^h	χ^2
(K)	(K)		(10^{14} cm)		(μm)	(μm)	(W m^{-2})	(L_{\odot})	(M_{\odot})	(yr)	($M_{\odot} \text{ yr}^{-1}$)	
J051418.09-691234.9 (disk source)												
†Two-component model, # 1: cold outer shell: Sil-Ow/0.4 + grf-DL/0.6 and amC-Hn: warm inner disk (disk fraction = 0.25)												98.0
†600 “shell”	114	30.0	13.0	0.4	0.005	0.25	7.5×10^{-14}	5822.0	1.21×10^{-3}	800	1.51×10^{-6}	
†1100 “disk”	249	15.0	0.99	5.0	0.005	2.0	2.5×10^{-14}	1941.0	4.67×10^{-5}	220	2.12×10^{-7}	
model # 1: varying the dust temperature at the inner radius of the cold outer shell												
450	88.1	30.0	24.1	0.40	0.005	0.25	7.5×10^{-14}	5822.0	4.13×10^{-3}	1480	2.80×10^{-6}	325.3
750	143	30.0	7.71	0.40	0.005	0.25	7.5×10^{-14}	5822.0	4.22×10^{-4}	472	8.94×10^{-7}	332.1
model # 1: varying the optical depth of the cold outer shell												
600	115	30.0	12.9	0.30	0.005	0.25	7.5×10^{-14}	5822.0	8.86×10^{-4}	790	1.12×10^{-6}	208.8
600	112	30.0	13.2	0.50	0.005	0.25	7.5×10^{-14}	5822.0	1.55×10^{-3}	809	1.91×10^{-6}	144.6
model # 1: varying the thickness of the cold outer shell												
600	184	10.0	13.1	0.40	0.005	0.25	7.5×10^{-14}	5822.0	4.08×10^{-4}	250	1.63×10^{-6}	155.4
model # 1: varying the dust temperature at the disk’s inner radius												
1000	228	15.0	1.23	5.00	0.005	2.0	2.5×10^{-14}	1941.0	7.19×10^{-5}	273	2.63×10^{-7}	126.8
1200	270	15.0	0.82	5.00	0.005	2.0	2.5×10^{-14}	1941.0	3.19×10^{-5}	182	1.76×10^{-7}	104.7
model # 1: varying the disk’s optical depth												
1100	258	15.0	0.96	4.0	0.005	2.0	2.5×10^{-14}	1941.0	3.48×10^{-5}	212	1.64×10^{-7}	104.4
1100	243	15.0	1.02	6.0	0.005	2.0	2.5×10^{-14}	1941.0	5.97×10^{-5}	227	2.63×10^{-7}	122.8
model # 1: varying the disk’s maximum grain size												
1100	268	15.0	1.04	5.0	0.005	1.0	2.5×10^{-14}	1941.0	3.45×10^{-5}	232	1.49×10^{-7}	144.6
1100	241	15.0	0.98	5.0	0.005	3.0	2.5×10^{-14}	1941.0	6.44×10^{-5}	217	2.97×10^{-7}	106.2
model # 1: varying the disk’s thickness												
1100	385	5.0	1.02	5.0	0.005	2.0	2.5×10^{-14}	1941.0	1.64×10^{-5}	64.5	2.54×10^{-7}	125.8
J055122.52-695351.4 (disk source)												
†Single shell (one-component) model with Sil-Ow grains												
†450	185	6	23.0	0.78	0.05	0.3	5.3×10^{-14}	4116.0	1.18×10^{-3}	243	4.86×10^{-6}	41.8
Varying the dust temperature at the shell’s inner radius												
400	161	6	31.0	0.78	0.05	0.3	5.3×10^{-14}	4116.0	2.15×10^{-3}	327	6.56×10^{-6}	284.3
500	210	6	17.5	0.78	0.05	0.3	5.3×10^{-14}	4116.0	6.81×10^{-4}	184	3.69×10^{-6}	128.5
Varying the shell’s optical depth												
450	187	6	22.8	0.70	0.05	0.3	5.3×10^{-14}	4116.0	1.05×10^{-3}	241	4.33×10^{-6}	56.5
450	183	6	23.1	0.85	0.05	0.3	5.3×10^{-14}	4116.0	1.30×10^{-3}	244	5.32×10^{-6}	63.7
Varying the minimum and maximum grain sizes in the shell												
450	178	6	23.7	0.78	0.005	0.3	5.3×10^{-14}	4116.0	1.53×10^{-3}	251	6.09×10^{-6}	132.8
450	191	6	18.7	0.78	0.05	0.5	5.3×10^{-14}	4116.0	9.97×10^{-4}	197	5.05×10^{-6}	48.2
Varying the shell thickness												
450	253	3	23.3	0.78	0.05	0.3	5.3×10^{-14}	4116.0	6.06×10^{-4}	98.4	6.16×10^{-6}	77.3
450	106	20	22.8	0.78	0.05	0.3	5.3×10^{-14}	4116.0	3.89×10^{-3}	917	4.24×10^{-6}	98.6
J052519.48-705410.0 (disk source)												
Single shell (one component) model, # 1 with Sil-Ow grains												
800	198	10.0	5.18	1.0	0.005	0.25	4.6×10^{-14}	3571.0	9.78×10^{-5}	98.5	9.92×10^{-7}	444.5
Single shell (one component) model, # 2 with grf-DL grains												
700	478	2.0	5.61	0.55	0.005	1.5	4.6×10^{-14}	3571.0	5.15×10^{-5}	11.9	4.34×10^{-6}	318.3
† Two-component model, # 3: cold grf-DL outer shell and warm Sil-Ow inner disk (disk fraction = 0.35)												35.9
600 “shell”	393	2.0	9.65	0.8	0.005	0.5	3.185×10^{-14}	2473.0	1.25×10^{-4}	20.4	6.12×10^{-6}	
800 “disk”	198	10.0	3.16	1.0	0.005	0.25	1.715×10^{-14}	1331.0	3.64×10^{-5}	451	8.08×10^{-8}	

Table 3 continued on next page

Table 3 (continued)

$T_d(\text{in})^a$	$T_d(\text{out})^b$	Y^c	R_{in}^d	τ^e	a_{min}	a_{max}	F_{bol}	L	M_{gd}^f	Age g	dM/dt^h	χ^2
(K)	(K)		(10^{14} cm)		(μm)	(μm)	(W m^{-2})	(L_\odot)	(M_\odot)	(yr)	($M_\odot \text{ yr}^{-1}$)	
model # 3: varying the dust temperature at the inner radius of the cold outer shell												
550	356	2.0	12.1	0.8	0.005	0.5	3.185×10^{-14}	2473.0	1.98×10^{-4}	25.6	7.70×10^{-6}	148.5
650	430	2.0	7.81	0.8	0.005	0.5	3.185×10^{-14}	2473.0	8.18×10^{-5}	16.5	4.96×10^{-6}	96.7
model # 3: varying the optical depth of the cold outer shell												
600	401	2.0	9.55	0.7	0.005	0.5	3.185×10^{-14}	2473.0	1.07×10^{-4}	20.2	5.31×10^{-6}	72.3
600	386	2.0	9.70	0.9	0.005	0.5	3.185×10^{-14}	2473.0	1.42×10^{-4}	20.5	6.93×10^{-6}	62.6
model # 3: varying the maximum grain sizes in the cold outer shell												
600	381	2.0	12.9	0.8	0.005	0.25	3.185×10^{-14}	2473.0	1.82×10^{-4}	27.2	6.69×10^{-6}	139.3
600	391	2.0	7.66	0.8	0.005	1.0	3.185×10^{-14}	2473.0	1.07×10^{-4}	16.2	6.62×10^{-6}	80.0
model # 3: varying the thickness of the cold outer shell												
600	261	5.0	6.2	0.8	0.005	0.5	3.185×10^{-14}	2473.0	1.29×10^{-4}	52.4	2.46×10^{-6}	227.3
model # 3: varying the dust temperature at the disk's inner radius												
650	170	10.0	4.71	1.0	0.005	0.25	1.715×10^{-14}	1331.0	8.07×10^{-5}	671	1.20×10^{-7}	63.4
950	230	10.0	2.20	1.0	0.005	0.25	1.715×10^{-14}	1331.0	1.76×10^{-5}	314	5.62×10^{-8}	52.6
model # 3: varying the disk's optical depth												
800	216	10.0	2.94	0.5	0.005	0.25	1.715×10^{-14}	1331.0	1.58×10^{-5}	420	3.76×10^{-8}	112.1
800	185	10.0	3.32	1.5	0.005	0.25	1.715×10^{-14}	1331.0	6.01×10^{-5}	473	1.27×10^{-7}	71.6
model # 3: varying the disk's thickness												
800	418	2.0	3.37	1.0	0.005	0.25	1.715×10^{-14}	1331.0	8.26×10^{-6}	53.4	1.55×10^{-7}	57.7
800	108	50.0	3.13	1.0	0.005	0.25	1.715×10^{-14}	1331.0	1.79×10^{-4}	2430	7.35×10^{-8}	41.5

NOTE—

The inner disk is approximated as an axially symmetric wedge-shaped fraction of a sphere. This fraction is referred to as “disk fraction”. The acronyms for the dust grain compositions refer to ‘warm’ and ‘cold’ silicates (Sil-Ow and Sil-Oc) from Ossenkopf et al. (1992), graphite grains (grf-DL) from Draine & Lee (1984), amorphous carbon (amC-Hn) from Hanner (1988) and silicon carbide (SiC-Pg) from Pégourié (1988).

shell: Parameters for the outer shell in two-component models

disk: Parameters for the inner disk in two-component models

shell(low-lat): Correctly illuminated models, part of shell in the solid angle not covered by the disk

shell(high-lat): Correctly illuminated models, part of shell in the solid angle covered by the disk

suffix ‘s’: Single shell model

suffix ‘c’: Correctly illuminated two-component model

†: Adopted (best-fit) model

^a The (input) dust temperature at shell inner radius

^b The (output) dust temperature at shell outer radius

^c The (input) ratio of the dust shell’s outer to inner radius

^d The (inferred) inner radius of the dust shell

^e The (input) dust shell’s optical depth at $0.55\mu\text{m}$

^f The (inferred) circumstellar (gas+dust) mass using $\delta = 200$

^g The (inferred) dust shell’s age

^h The (inferred) mass-loss rate characterizing the dust shell

Table 4. Important parameters derived from the best-fit models

Object	Disk-Fraction	Inner disk/shell					Outer shell					$\frac{M_{\text{gd}}(dust)}{M_{\text{gd}}(shell)}$	χ^2/h					
		Dust Composition	T_d (in)	a	τb	$a_{\text{min}} c$	$a_{\text{max}} d$	γe	$M_{\text{gd}} f$	Dust Composition	T_d (in)			a	τb	$a_{\text{min}} c$	$a_{\text{max}} d$	γe
			(K)	(K)	(μm)	(μm)	(M_{\odot})	(M_{\odot})	(M_{\odot})	(M_{\odot})	(K)	(K)	(μm)	(μm)	(M_{\odot})	(M_{\odot})	(L_{\odot})	
post-RGB stars																		
shell sources																		
J043919.30-685733.4	0.35	SiL-Ow/1.0	1000	0.5	0.005	0.25	1.4	2.19×10^{-8}	SiL-Ow/1.0	130	0.65	0.005	0.25	20	5.2×10^{-3}	116	4.21×10^{-6}	18.1
J051347.57-704450.5	SiL-Ow/1.0	250	0.40	0.1	0.25	3.0	4.66×10^{-5}	776	...	69.2
J051920.18-722522.1	0.4	SiL-Ow/1.0	500	0.4	0.5	20	2.0	3.01×10^{-5}	SiL-Ow/1.0	110	0.65	0.005	0.25	20	3.41×10^{-2}	582	8.83×10^{-4}	17.5
J053930.60-702248.5	SiL-Ow/1.0	300	0.70	0.005	0.25	10	5.81×10^{-5}	295	...	30.4
disk sources																		
J045555.15-712112.3	0.4	SiL-Ow/1.0	1000	1.0	0.005	0.25	10.0	3.08×10^{-6}	SiL-Ow/1.0	300	2.5	0.005	0.25	2.0	2.84×10^{-4}	465	1.08×10^{-2}	116.6
J045755.05-681649.2	0.4	SiL-Ow/1.0	1300	0.5	0.005	2.0	2.0	9.64×10^{-9}	SiL-Ow/1.0	400	0.6	0.1	1.0	30.0	5.73×10^{-5}	217	1.68×10^{-4}	24.7
J050257.89-665306.3	0.4	SiL-Ow/1.0	1200	0.5	0.3	5.0	3.0	5.77×10^{-8}	SiL-Ow/1.0	250	0.65	0.005	1.0	10.0	2.24×10^{-4}	303	2.56×10^{-4}	48.4
J055102.44-685639.1	0.3	amC-Hn/1.0	2000	1.0	0.005	0.05	7.0	1.99×10^{-8}	SiL-Ow/0.4+SiC-Pg/0.6	350	12.0	0.005	0.07	3.0	3.05×10^{-3}	621	6.52×10^{-6}	147.3
post-AGB stars																		
shell sources																		
J050632.10-714229.8	...	grf-DL / 0.3+SiL-Ow/0.7	350	0.4	0.1	1.0	5.0	7.5×10^{-4}	SiL-Ow/1.0	100	0.35	0.005	0.25	2.0	5.92×10^{-2}	5434	1.27×10^{-2}	154.7
J051848.84-700247.0	SiL-Ow/1.0	350	3.2	0.005	0.25	20.0	1.76×10^{-2}	6210	...	50.4
J051906.86-694153.9	...	amC-Hn/1.0	2000	0.35	0.005	0.25	2.0	9.58×10^{-9}	SiC-Pg/1.0	160	0.07	2.3	3.0	2.0	1.78×10^{-4}	2018	5.38×10^{-5}	21.3
J053250.69-713925.8	SiL-Ow/0.2+grf-DL/0.8	260	0.9	0.005	0.50	2.0	6.45×10^{-3}	4657	...	214.4
disk sources																		
J045623.21-692749.0	...	SiL-Ow/1.0	1100	0.6	0.005	5.0	3.0	3.38×10^{-6}	SiL-Ow/1.0	150	0.1	0.005	0.25	2.0	8.25×10^{-4}	6598	4.1×10^{-3}	100.2
J051418.09-691234.9	0.25	amC-Hn/1.0	1100	5.0	0.005	2.0	15.0	4.67×10^{-5}	SiL-Ow/0.4+grf-DL/0.6	600	0.4	0.005	0.25	30.0	1.21×10^{-3}	7763	3.86×10^{-2}	98.0
J055122.52-695351.4	SiL-Ow/1.0	450	0.78	0.05	0.3	6.0	1.18×10^{-3}	4116	...	41.8
J052519.48-705410.0	0.35	SiL-Ow/1.0	800	1.0	0.005	0.25	20.0	3.64×10^{-5}	grf-DL/1.0	600	0.8	0.005	0.5	2.0	1.25×10^{-4}	3804	0.29	35.9

NOTE—

The acronyms for the dust grain compositions refer to ‘warm’ silicates (SiL-Ow) from Ossenkopf et al. (1992), graphite grains (grf-DL) from Draine & Lee (1984), amorphous carbon (amC-Hn) from Hanner (1988) and silicon carbide (SiC-Pg) from Pégourié (1988).

^a The (input) dust temperature at shell (disk) inner radius

^b The dust shell’s (disk’s) optical depth at 0.55 μm

^c The minimum dust grain size

^d The maximum dust grain size

^e The thickness of the disk/shell

^f The (inferred) circumstellar (gas+dust) mass using $\delta = 200$

^g The (inferred) luminosity

^h The reduced chi-square value

Table 5. I-band photometry

Object	Zaritsky (Imag)	DENIS (Imag)	USNO-B 1.0 (Imag)
post-RGB stars			
J043919.30-685733.4	17.900	17.658	...
J051347.57-704450.5	15.683	15.699	...
J051920.18-722522.1	16.152	16.169	15.87
J053930.60-702248.5	16.915	16.917	...
J045555.15-712112.3
J045755.05-681649.2	17.205	17.352	17.73
J050257.89-665306.3	17.563	16.536	16.34
J055102.44-685639.1	17.821	17.866	17.16
post-AGB			
J050632.10-714229.8	13.780	13.886	13.53
J051848.84-700247.0	13.852	13.845	...
J051906.86-694153.9	14.473
J053250.69-713925.8	13.803	13.877	13.60
J045623.21-692749.0	13.123	13.154	12.85
J051418.09-691234.9	13.853	13.856	13.38
J055122.52-695351.4	14.009	14.077	13.64
J052519.48-705410.0	14.276	14.575	14.50

Table 6. Luminosities of the sources

Object	Best-fit Model		KWVW15	
			Observed	Photospheric
	L_{\odot}		L_{\odot}	L_{\odot}
post-RGB stars				
J043919.30-685733.4	116		106	159
J051347.57-704450.5	776		712	840
J051920.18-722522.1	582		496	507
J053930.60-702248.5	295		248	294
J045555.15-712112.3	465		454	191
J045755.05-681649.2	217		190	215
J050257.89-665306.3	303		267	177
J055102.44-685639.1	621		452	815
post-AGB stars				
J050632.10-714229.8	5434		4910	7606
J051848.84-700247.0	6210		4477	14112
J051906.86-694153.9	2018		2052	4246
J053250.69-713925.8	4657		4223	11056
J045623.21-692749.0	6598		6864	7131
J051418.09-691234.9	7763		6667	4703
J055122.52-695351.4	4116		3780	3657
J052519.48-705410.0	3804		3219	4943

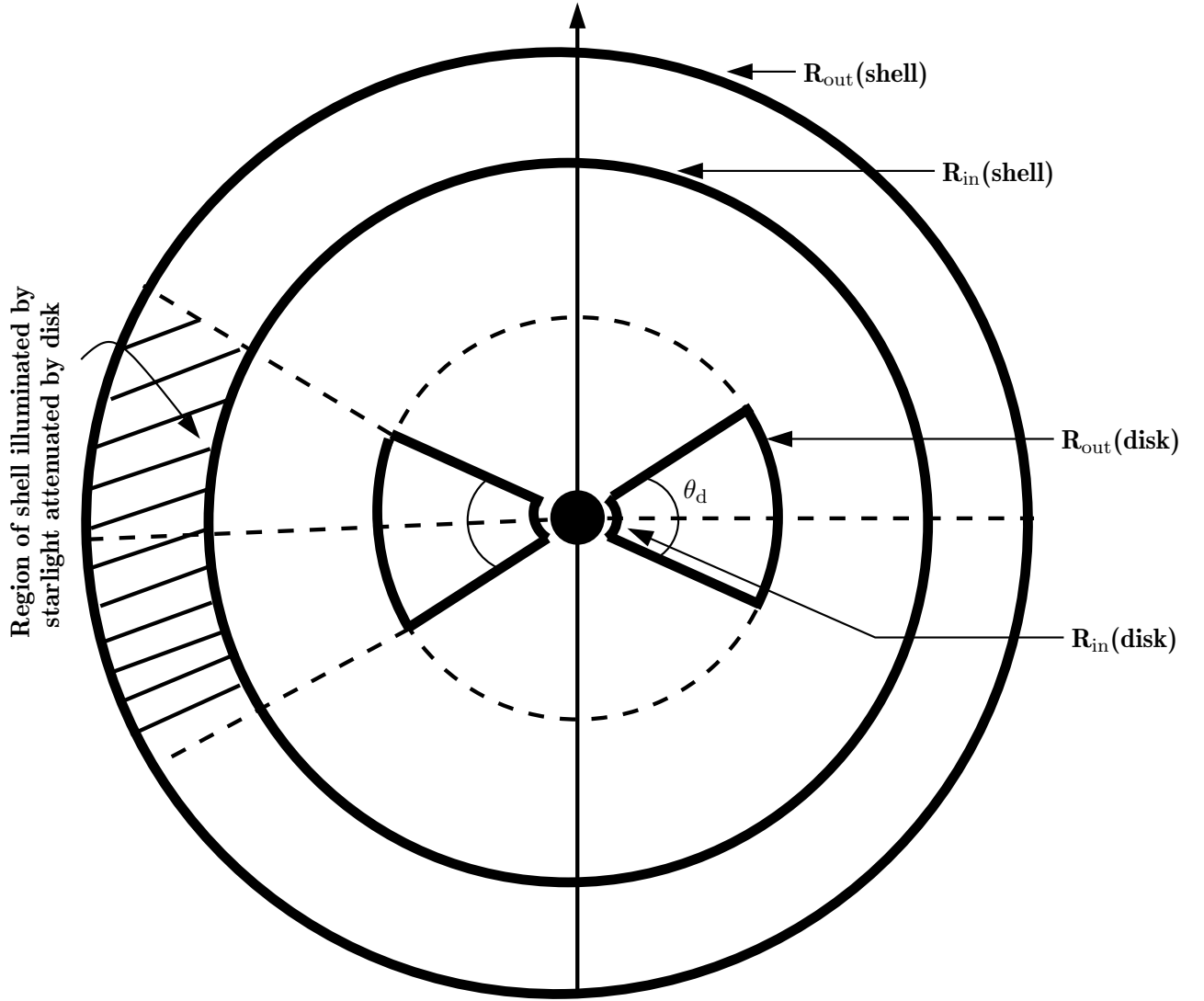


Figure 1. Illustration showing post-RGB dust geometry with an inner disk and an outer shell. R_{in} and R_{out} are the inner and outer radius of the disk (shell). A disk with an opening angle θ_d intercepts $\text{Sin}(\theta_d/2)$ (referred to as disk-fraction in this paper) of starlight.

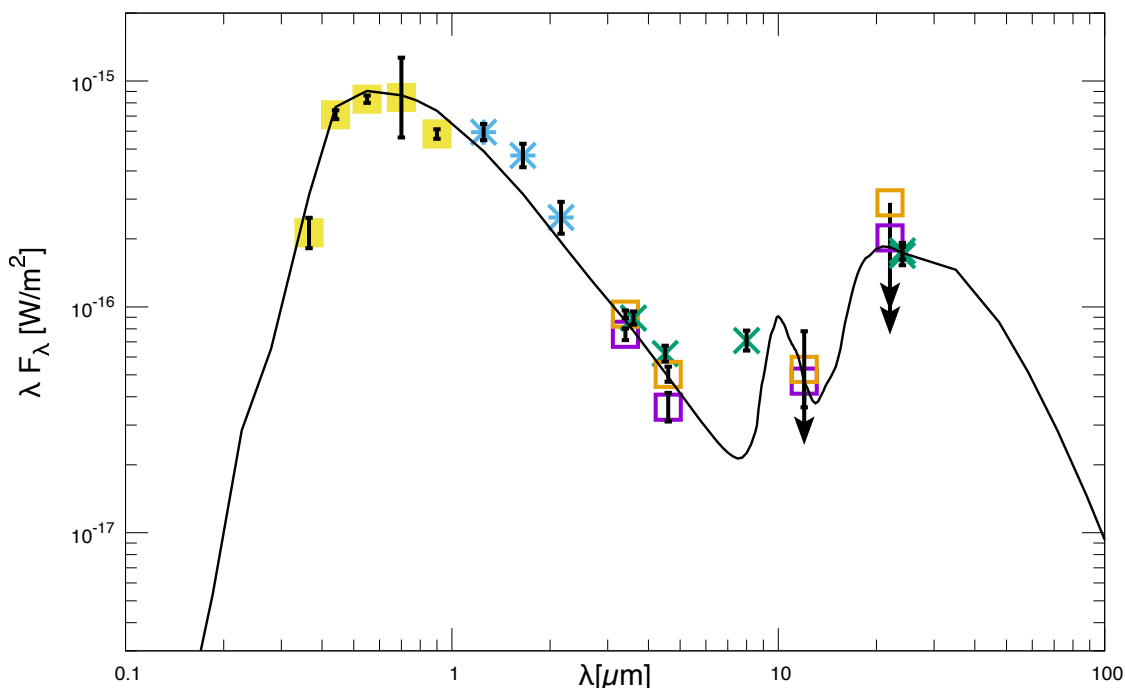


Figure 2. The figure shows the adopted two-component best-fit, model # 1,c ($\chi^2 = 18.1$) for the post-RGB (shell) source, J043919.30-685733.4. The observed fluxes are de-reddened for Galactic and LMC reddening. U,B,V,R,I (yellow), 2MASS J,H,K (cyan) data are plotted along with WISE (purple) and ALLWISE (orange) photometry and data from the SAGE-LMC Survey (green) which covers the IRAC and MIPS bands. The error bars and upper limits (arrows) are indicated in black. All model fits obtained for the source including the adopted best-fit are available in the corresponding Figure Set.

- Fig. Set 2. J043919.30-685733.4 (post-RGB shell source)
- Fig. Set 3. J051347.57-704450.5 (post-RGB shell source)
- Fig. Set 4. J051920.18-722522.1 (post-RGB shell source)
- Fig. Set 5. J053930.60-702248.5 (post-RGB shell source)
- Fig. Set 6. J045555.15-712112.3 (post-RGB disk source)
- Fig. Set 7. J045755.05-681649.2 (post-RGB disk source)
- Fig. Set 8. J050257.89-665306.3 (post-RGB disk source)
- Fig. Set 9. J055102.44-685639.1 (post-RGB disk source)
- Fig. Set 10. J050632.10-714229.8 (post-AGB shell source)
- Fig. Set 11. J051848.84-700247.0 (post-AGB shell source)
- Fig. Set 12. J051906.86-694153.9 (post-AGB shell source)
- Fig. Set 13. J053250.69-713925.8 (post-AGB shell source)
- Fig. Set 14. J045623.21-692749.0 (post-AGB disk source)
- Fig. Set 15. J051418.09-691234.9 (post-AGB disk source)
- Fig. Set 16. J055122.52-695351.4 (post-AGB disk source)
- Fig. Set 17. J052519.48-705410.0 (post-AGB disk source)

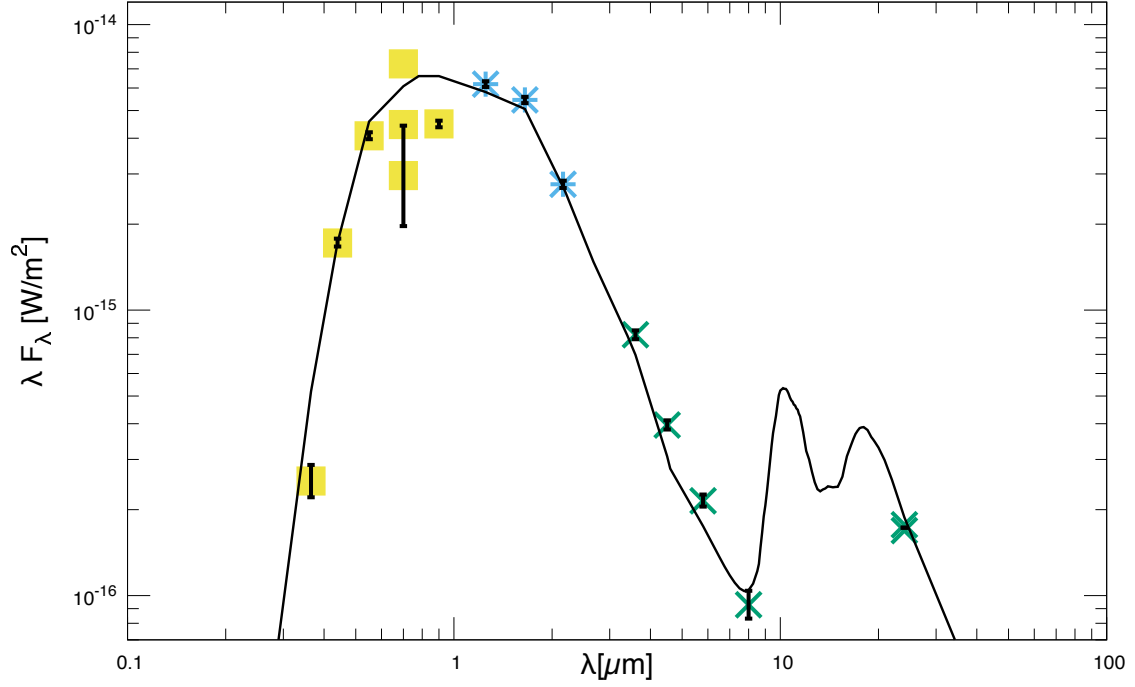


Figure 3. The figure shows the adopted one-component best-fit model ($\chi^2 = 69.2$) for the post-RGB (shell) source, J051347.57-704450.5. The observed fluxes are de-reddened for Galactic and LMC reddening. U,B,V,R,I (yellow), 2MASS J,H,K (cyan) data are plotted along with data from the SAGE-LMC Survey (green) which covers the IRAC and MIPS bands. The error bars are indicated in black. All model fits obtained for the source including the adopted best-fit are available in the corresponding Figure Set.

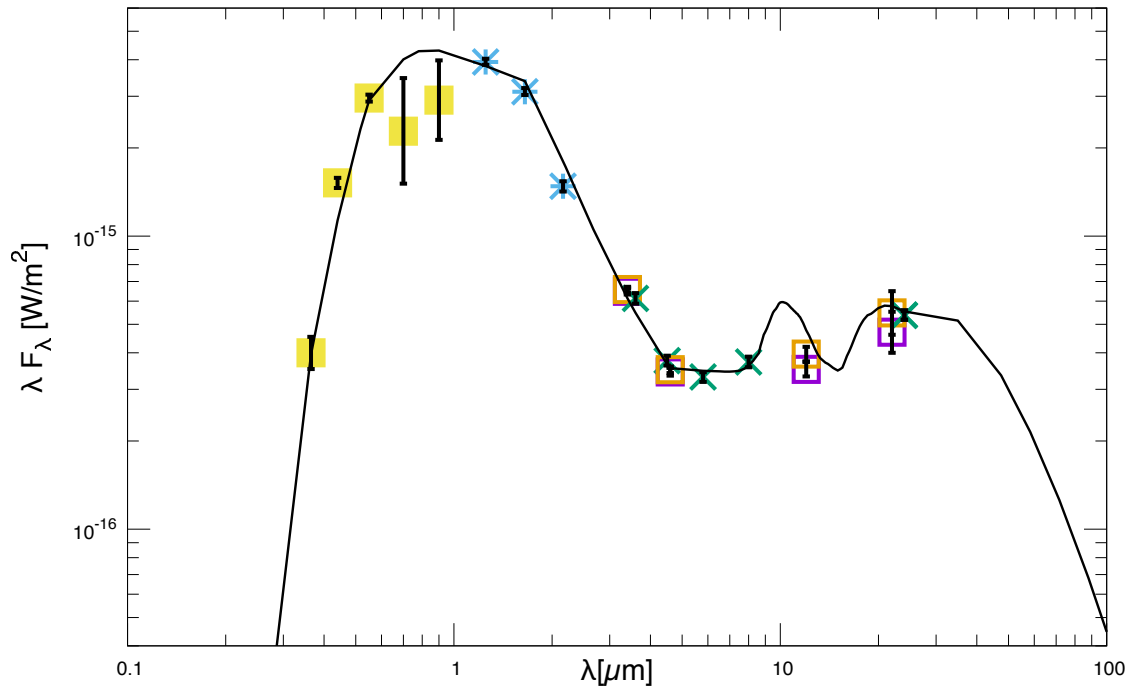


Figure 4. The figure shows the adopted two-component best-fit model (disk fraction = 0.4; $\chi^2 = 17.5$) for the post-RGB (shell) source, J051920.18-722522.1. The fit (model # 2,c) corresponds to the correctly illuminated model # 2. The observed fluxes are de-reddened for Galactic and LMC reddening. U,B,V,R,I (yellow), 2MASS J,H,K (cyan) data are plotted along with WISE (purple) and ALLWISE photometry (orange) and data from the SAGE-LMC Survey (green) which covers the IRAC and MIPS bands. The error bars are indicated in black. All model fits obtained for the source including the adopted best-fit are available in the corresponding Figure Set.

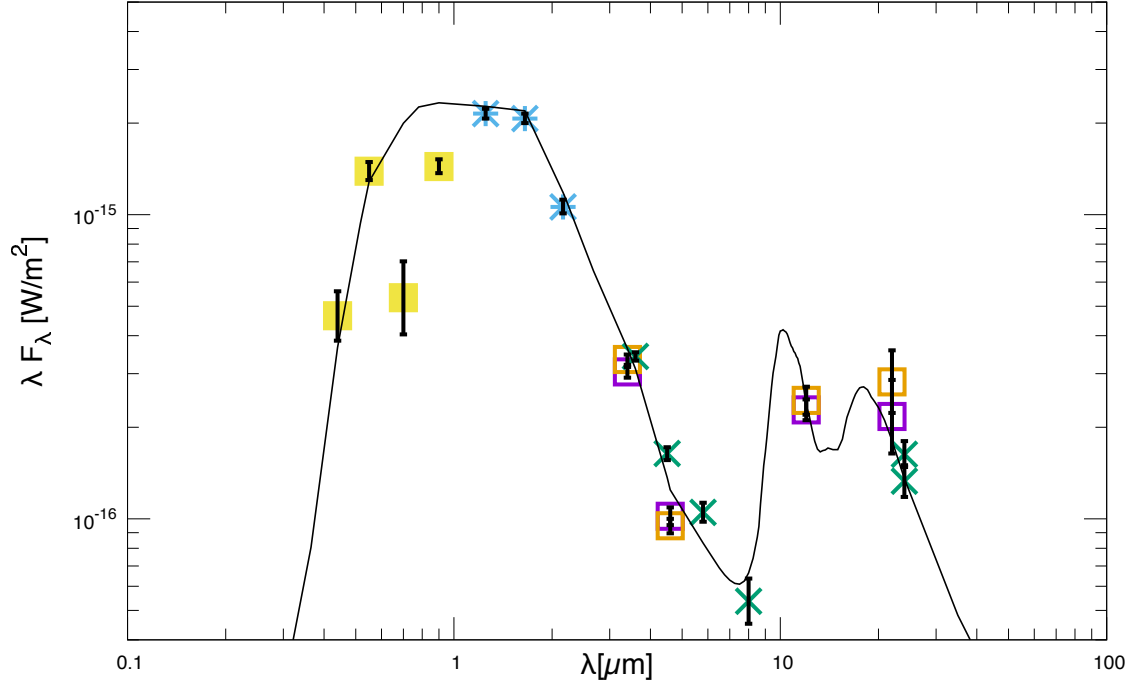


Figure 5. The figure shows the adopted one-component model fit ($\chi^2 = 30.4$) to the observed SED of the post-RGB (shell) source, J053930.60-702248.5. The observed fluxes are de-reddened for Galactic and LMC reddening. B,V,R,I (yellow), 2MASS J,H,K (cyan) data are plotted along with WISE (purple) and ALLWISE (orange) photometry and data from the SAGE-LMC Survey (green) which covers the IRAC and MIPS bands. The error bars are indicated in black. All model fits obtained for the source including the adopted best-fit are available in the corresponding Figure Set.

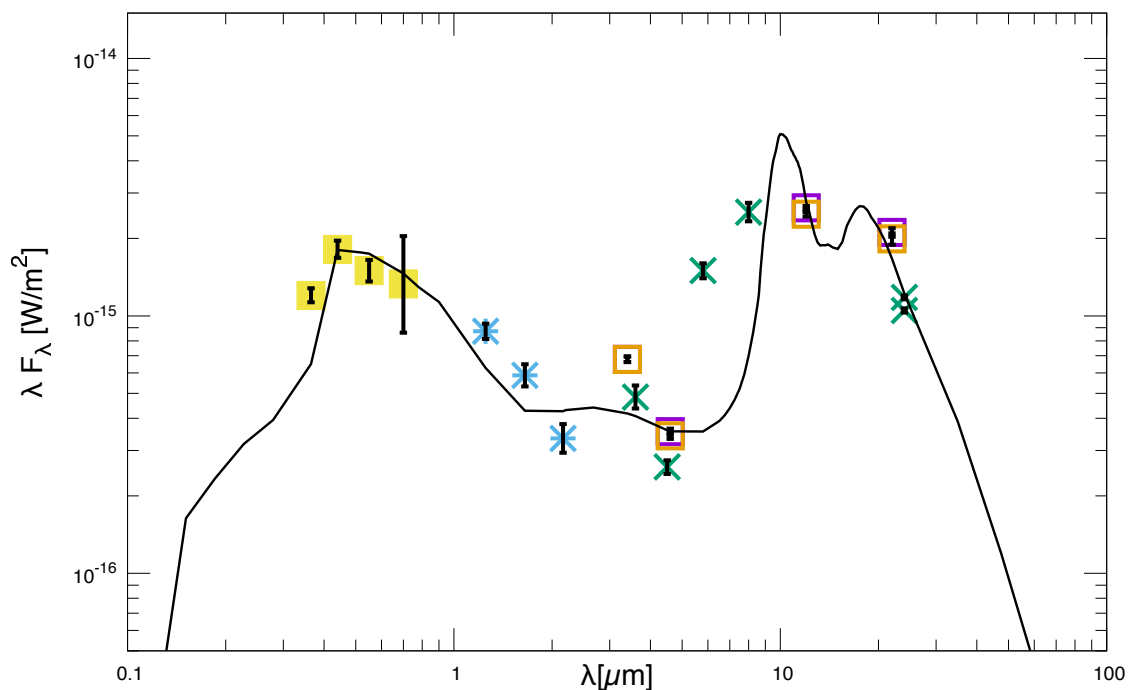


Figure 6. The figure shows the adopted two-component model fit (model # 4, disk fraction = 0.4, $\chi^2 = 116.6$) to the observed SED of the post-RGB (disk) source, J045555.15-712112.3. The observed fluxes are de-reddened for Galactic and LMC reddening. U,B,V,R (yellow), 2MASS J,H,K (cyan) data are plotted along with WISE (purple) and ALLWISE (orange) photometry and data from the SAGE-LMC Survey (green) which covers the IRAC and MIPS bands. The error bars are indicated in black. All model fits obtained for the source including the adopted best-fit are available in the corresponding Figure Set.

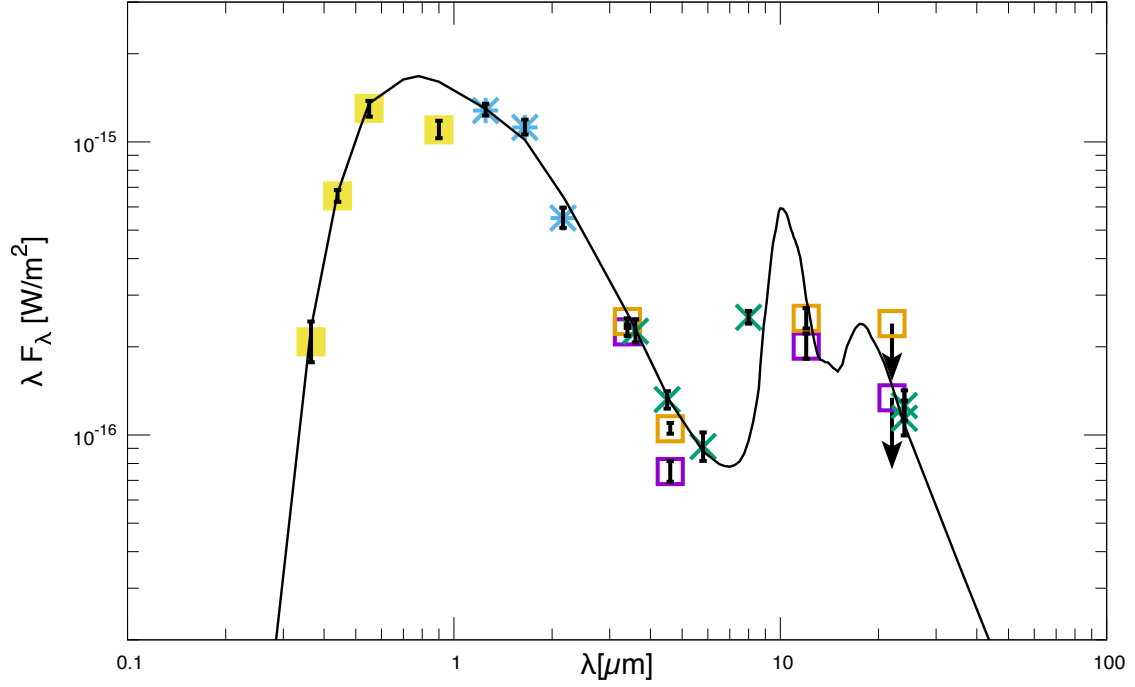


Figure 7. The figure shows the adopted two-component model fit (model # 2,c, disk fraction = 0.4, $\chi^2 = 24.7$) to the observed SED of the post-RGB (disk) source, J045755.05-681649.2. The observed fluxes are de-reddened for Galactic and LMC reddening. U,B,V,I (yellow), 2MASS J,H,K (cyan) data are plotted along with WISE (purple) and ALLWISE (orange) photometry and data from the SAGE-LMC Survey (green) which covers the IRAC and MIPS bands. The error bars are indicated in black. All model fits obtained for the source including the adopted best-fit are available in the corresponding Figure Set.

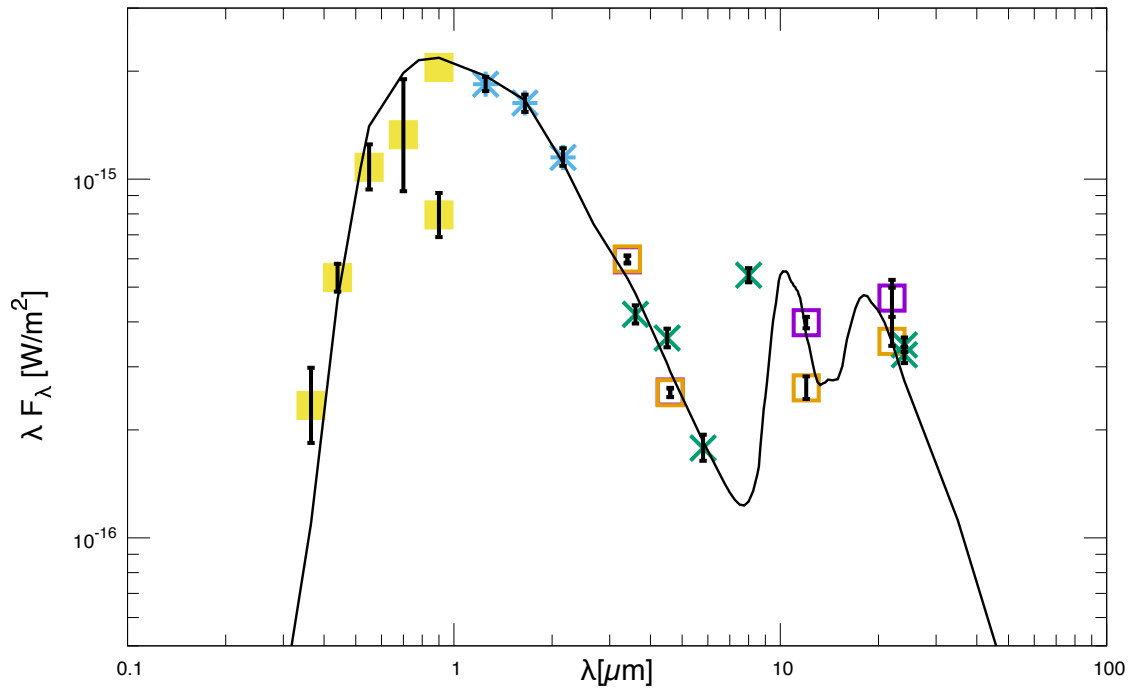


Figure 8. The figure shows the adopted two-component model fit (model # 2,c, disk fraction = 0.4, $\chi^2 = 48.4$) to the observed SED of the post-RGB (disk) source, J050257.89-665306.3. The observed fluxes are de-reddened for Galactic and LMC reddening. U,B,V,R,I (yellow), 2MASS J,H,K (cyan) data are plotted along with WISE (purple) and ALLWISE (orange) photometry and data from the SAGE-LMC Survey (green) which covers the IRAC and MIPS bands. The error bars are indicated in black. All model fits obtained for the source including the adopted best-fit are available in the corresponding Figure Set.

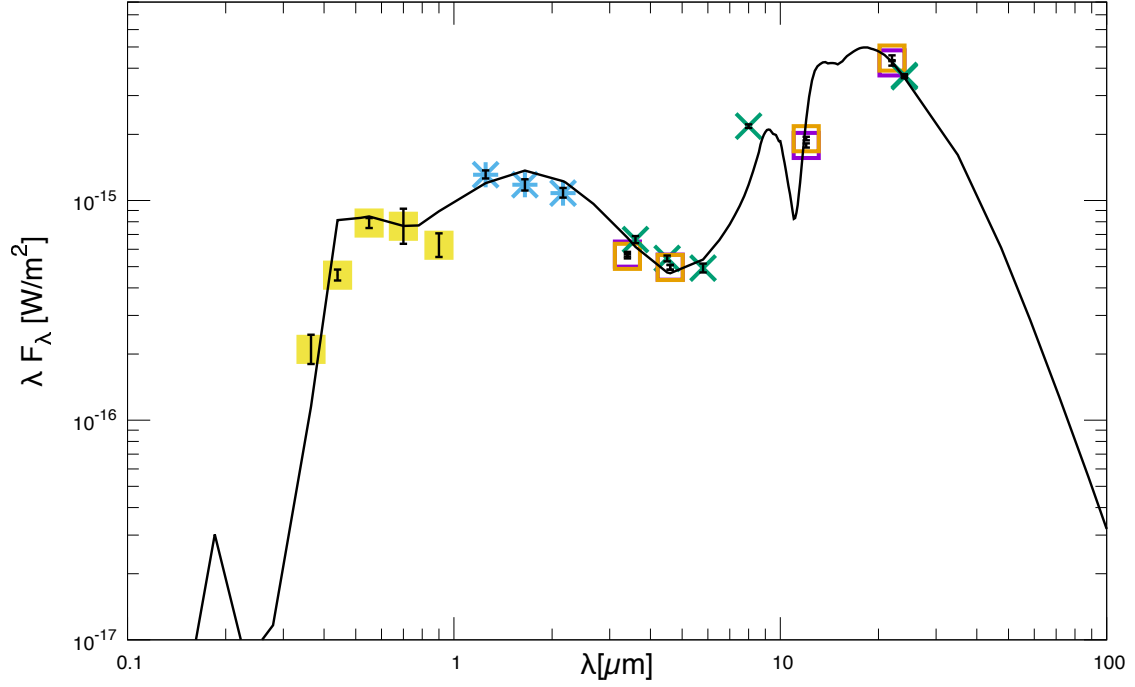


Figure 9. The figure shows the adopted two-component model fit (model # 3, disk fraction = 0.3; $\chi^2 = 147.3$) to the observed SED of the post-RGB (disk) source, J055102.44-685639.1. The observed fluxes are de-reddened for Galactic and LMC reddening. U,B,V,R,I (yellow), 2MASS J,H,K (cyan) data are plotted along with WISE (purple) and ALLWISE (orange) photometry and data from the SAGE-LMC Survey (green) which covers the IRAC and MIPS bands. The error bars are indicated in black. All model fits obtained for the source including the adopted best-fit are available in the corresponding Figure Set.

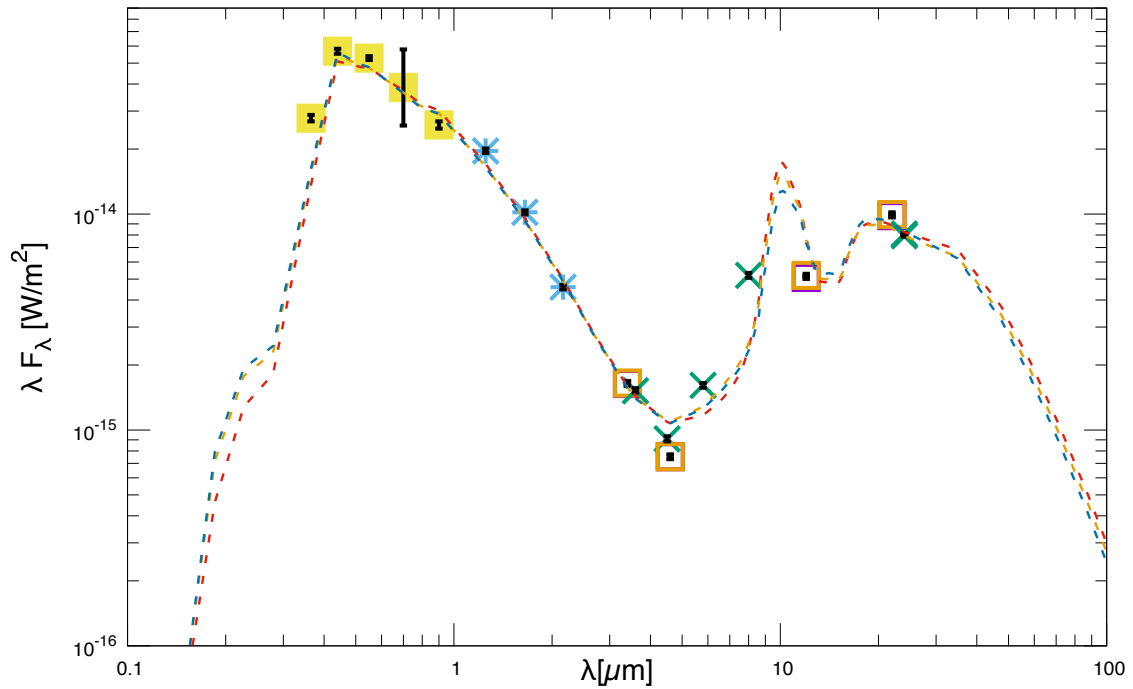


Figure 10. The figure shows the nested shells models for the post-AGB (shell) source, J050632.10-714229.8. The fits correspond to the correctly illuminated outer shell, Table 3. The observed fluxes are de-reddened for Galactic and LMC reddening. U,B,V,R,I (yellow), 2MASS J,H,K (cyan) data are plotted along with WISE (purple) and ALLWISE (orange) photometry and data from the SAGE-LMC Survey (green) which covers the IRAC and MIPS bands. The error bars are indicated in black. All model fits obtained for the source including the nested shells models are available in the corresponding Figure Set.

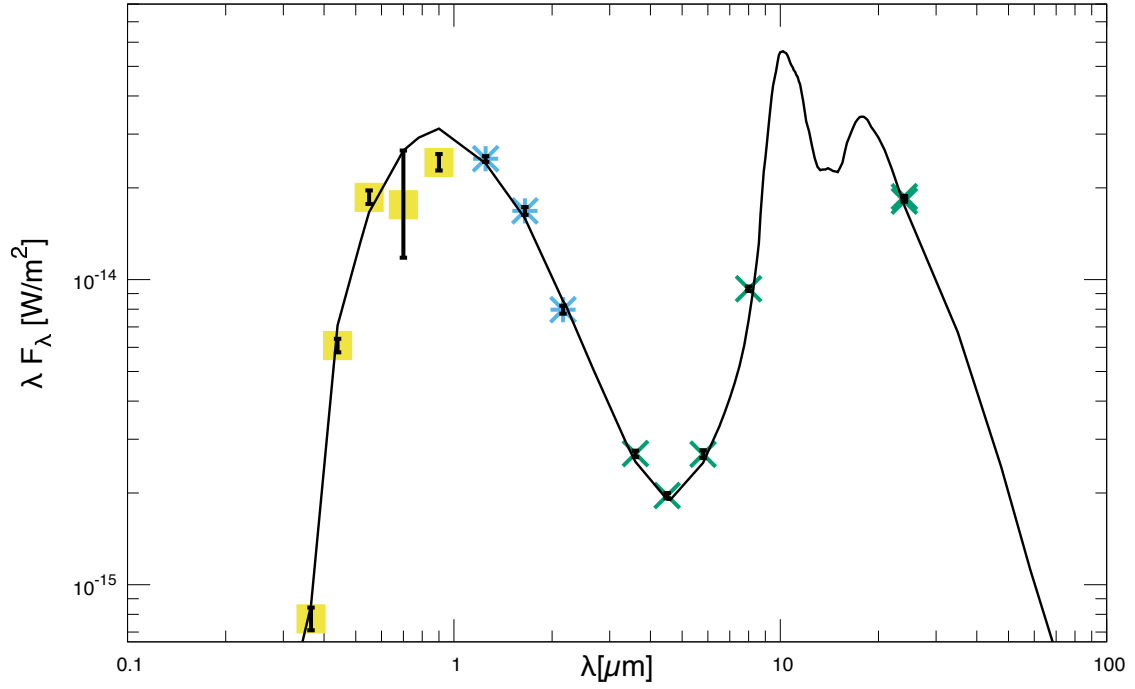


Figure 11. The adopted one-component model fit ($\chi^2 = 50.4$) to the observed SED of the post-AGB (shell) source, J051848.84-700247.0. The observed fluxes are de-reddened for Galactic and LMC reddening. U,B,V,R,I (yellow), 2MASS J,H,K (cyan) data are plotted along with data from the SAGE-LMC Survey (green) which covers the IRAC and MIPS bands. The error bars are indicated in black. All model fits obtained for the source including the adopted best-fit are available in the corresponding Figure Set.

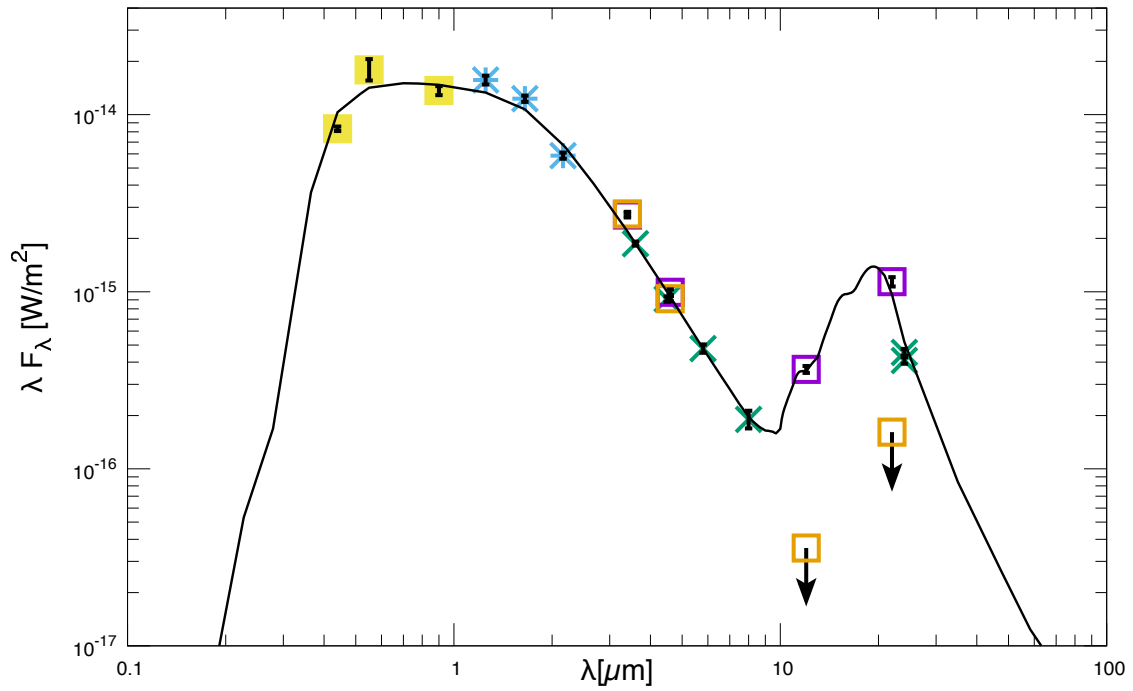


Figure 12. The figure shows the adopted nested shells model ($\chi^2 = 21.3$) for the post-AGB (shell) source, J051906.86-694153.9. The observed fluxes are de-reddened for Galactic and LMC reddening. B,V,I (yellow), 2MASS J,H,K (cyan) data are plotted along with WISE (purple) and ALLWISE (orange) photometry and data from the SAGE-LMC Survey (green) which covers the IRAC and MIPS bands. The error bars are indicated in black. All model fits obtained for the source including the adopted best-fit are available in the corresponding Figure Set.

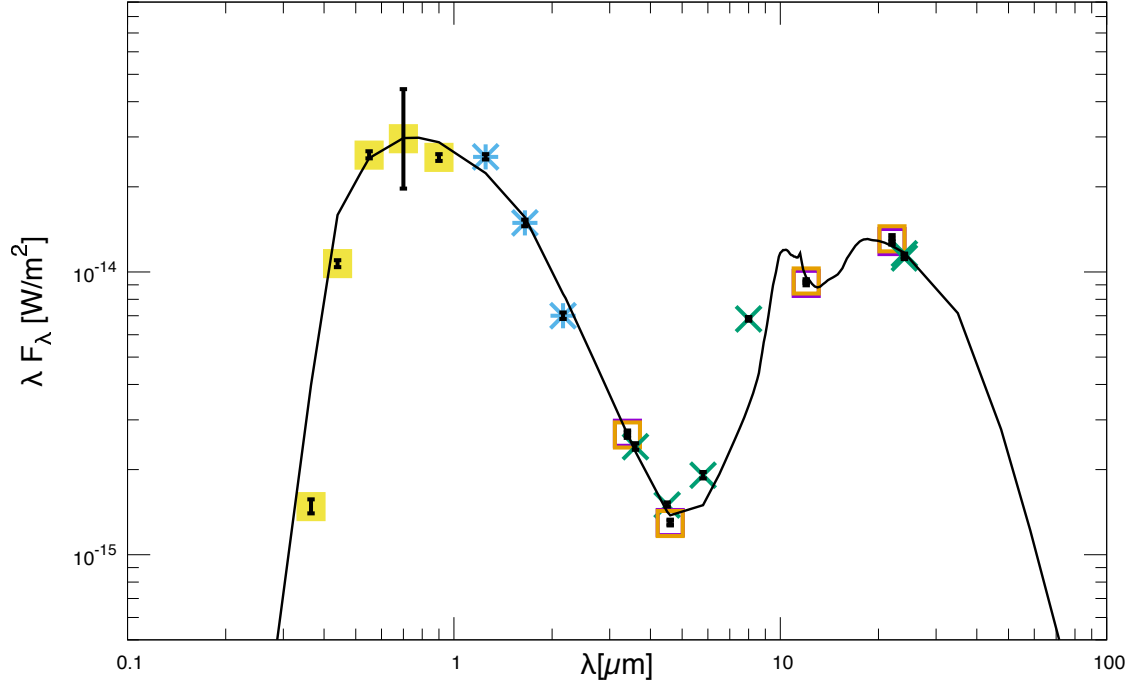


Figure 13. The adopted one-component model fit ($\chi^2 = 214.4$) to the observed SED of the post-AGB (shell) source, J053250.69-713925.8. The observed fluxes are de-reddened for Galactic and LMC reddening. U,B,V,R,I (yellow), 2MASS J,H,K (cyan) data are plotted along with WISE (purple) and ALLWISE (orange) photometry and data from the SAGE-LMC Survey (green) which covers the IRAC and MIPS bands. The error bars are indicated in black. All model fits obtained for the source including the adopted best-fit are available in the corresponding Figure Set.

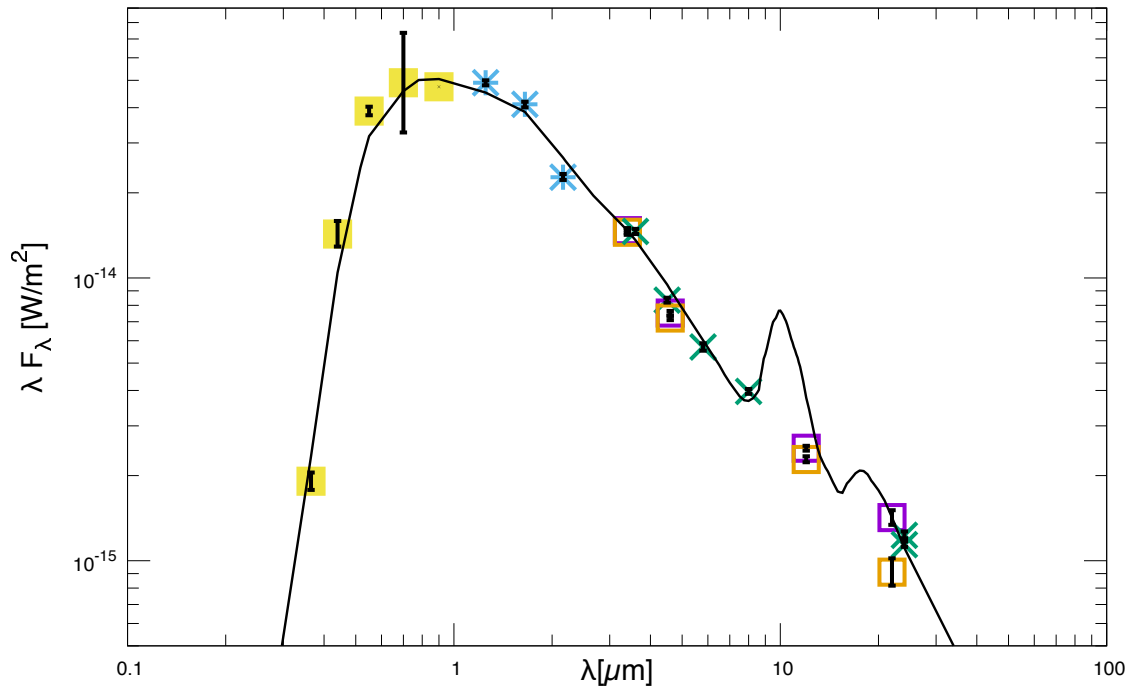


Figure 14. The adopted nested shells model (model # 1, $\chi^2 = 100.2$) for the post-AGB (disk) source, J045623.21-692749.0. The observed fluxes are de-reddened for Galactic and LMC reddening. U,B,V,R,I (yellow), 2MASS J,H,K (cyan) data are plotted along with WISE (purple) and ALLWISE (orange) photometry and data from the SAGE-LMC Survey (green) which covers the IRAC and MIPS bands. The error bars are indicated in black. All model fits obtained for the source including the adopted best-fit are available in the corresponding Figure Set.

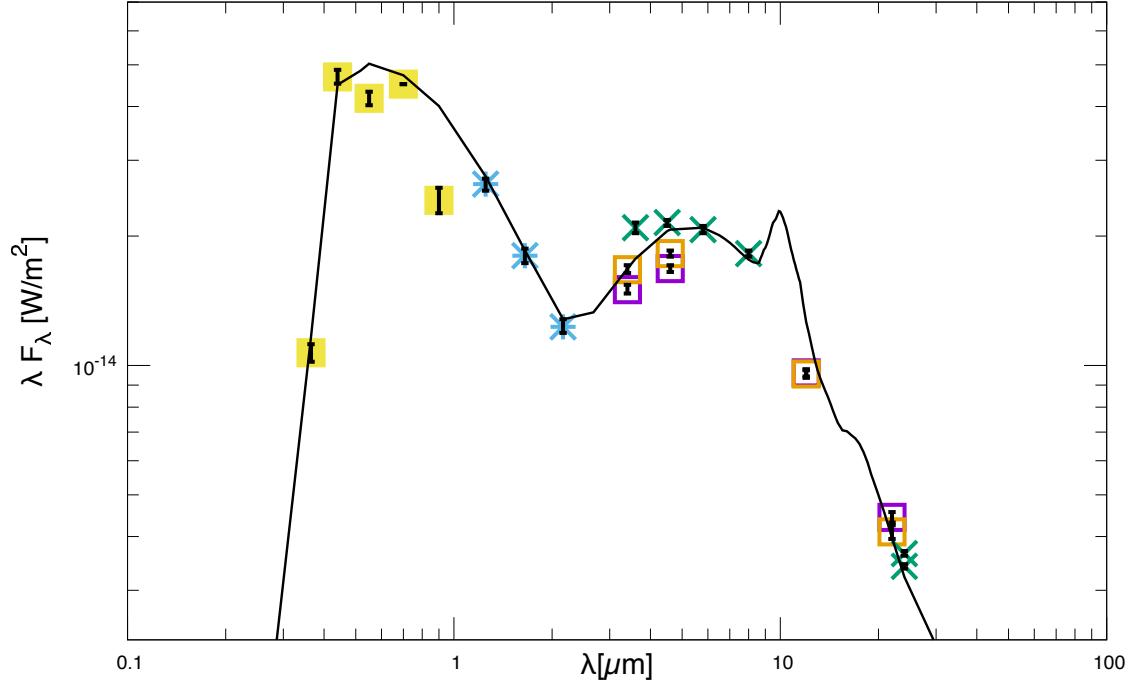


Figure 15. The adopted two-component model fit (disk fraction = 0.25, $\chi^2 = 98.0$) to the observed SED of the post-AGB (disk) source, J051418.09-691234.9. The observed fluxes are de-reddened for Galactic and LMC reddening. U,B,V,R,I (yellow), 2MASS J,H,K (cyan) data are plotted along with WISE (purple) and ALLWISE (orange) photometry and data from the SAGE-LMC Survey (green) which covers the IRAC and MIPS bands. The error bars are indicated in black. All model fits obtained for the source including the adopted best-fit are available in the corresponding Figure Set.

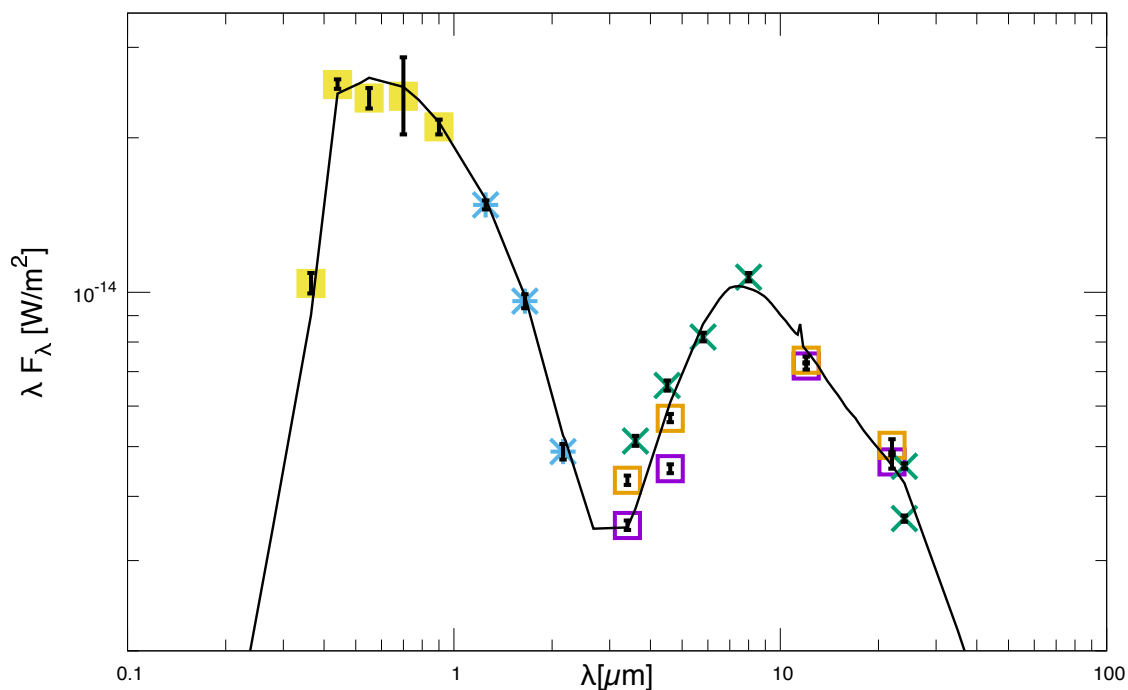


Figure 16. The adopted one-component model fit ($\chi^2 = 41.8$) to the observed SED of the post-AGB (disk) source, J055122.52-695351.4. The observed fluxes are de-reddened for Galactic and LMC reddening. U,B,V,R,I (yellow), 2MASS J,H,K (cyan) data are plotted along with WISE (purple) and ALLWISE (orange) photometry and data from the SAGE-LMC Survey (green) which covers the IRAC and MIPS bands. The error bars are indicated in black. All model fits obtained for the source including the adopted best-fit are available in the corresponding Figure Set.

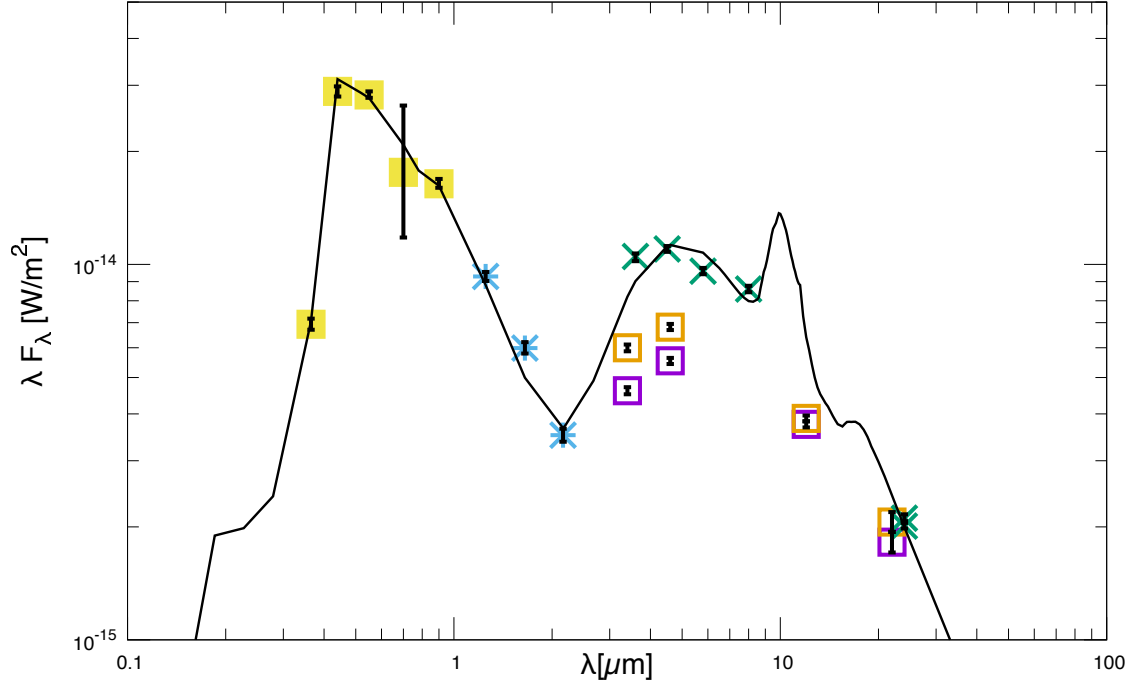


Figure 17. The adopted two-component model fit (disk fraction = 0.35, $\chi^2 = 35.9$) to the observed SED of the post-AGB (disk) source, J052519.48-705410.0. The observed fluxes are de-reddened for Galactic and LMC reddening. U,B,V,R,I (yellow), 2MASS J,H,K (cyan) data are plotted along with WISE (purple) and ALLWISE (orange) photometry and data from the SAGE-LMC Survey (green) which covers the IRAC and MIPS bands. The error bars are indicated in black. All model fits obtained for the source including the adopted best-fit are available in the corresponding Figure Set

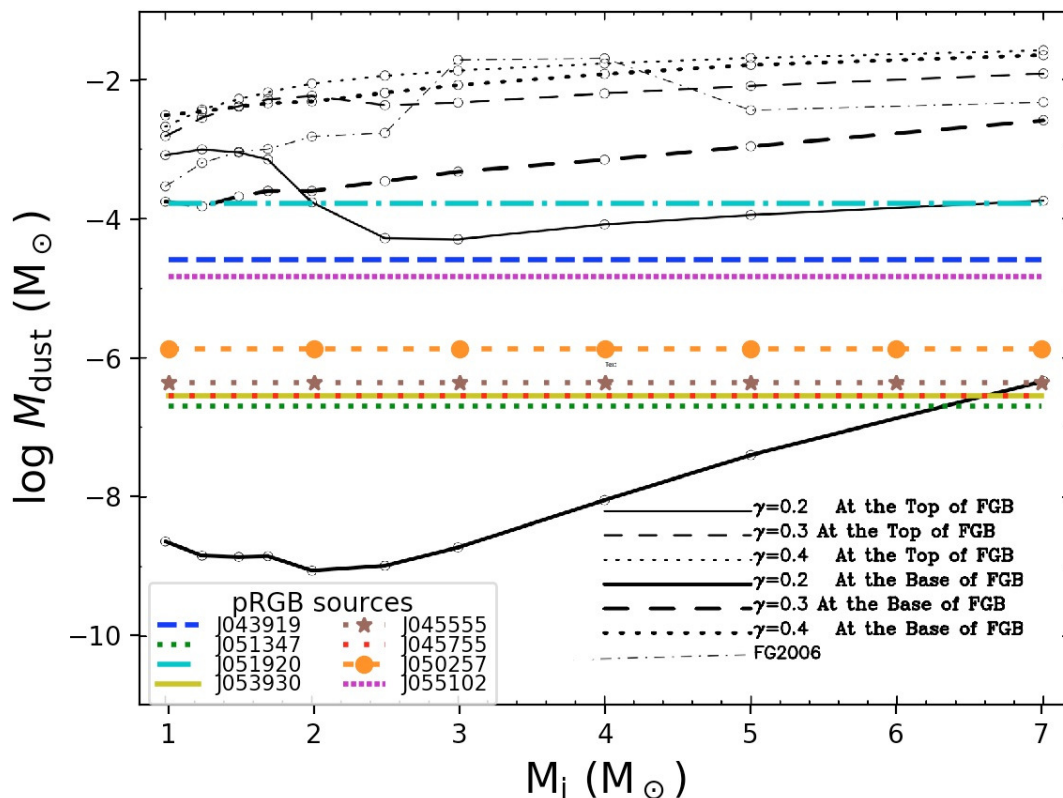


Figure 18. The circumstellar dust mass (M_d) of our post-RGB objects are shown (colored horizontal lines) on a plot of theoretically estimated dust masses in the ejecta of common envelope systems versus initial stellar mass, taken from Fig. 2 of Lü et al. (2013). FGB refers to the first red giant branch. FG2006 refers to results by Ferrarotti & Gail (2006), showing the dust masses produced in the dust-driven outflows of AGB stars. M_d scales in proportion to the thickness of the circumstellar component. Determination of the latter is constrained by the long wavelength limit of our data ($24 \mu\text{m}$). Our estimated M_d values may be treated as lower limits to the actual dust mass in the shells.